2009

MICROSTRUCTURAL EVOLUTION AND PHYSICAL BEHAVIOR OF PALLADIUM AND OSMIUM-RUTHENIUM NOBLE METAL FILMS

Wen-Chung Li
University of Kentucky, micro_scientist@yahoo.com.tw

Recommended Citation
Li, Wen-Chung, "MICROSTRUCTURAL EVOLUTION AND PHYSICAL BEHAVIOR OF PALLADIUM AND OSMIUM-RUTHENIUM NOBLE METAL FILMS" (2009). *University of Kentucky Doctoral Dissertations.* Paper 802.
http://uknowledge.uky.edu/gradschool_diss/802

ABSTRACT OF DISSERTATION

Wen-Chung Li

The Graduate School

University of Kentucky

2009

MICROSTRUCTURAL EVOLUTION AND PHYSICAL BEHAVIOR OF PALLADIUM AND OSMIUM-RUTHENIUM NOBLE METAL FILMS

ABSTRACT OF DISSERTATION

A dissertation submitted in partial fulfillment of the
requirements for the degree of Doctor of Philosophy in the
College of Engineering
at the University of Kentucky

By
Wen-Chung Li

Lexington, Kentucky

Director: Dr. T. John Balk, Professor of Chemical and Materials Engineering

Lexington, Kentucky

2009

ABSTRACT OF DISSERTATION

MICROSTRUCTURAL EVOLUTION AND PHYSICAL BEHAVIOR OF PALLADIUM AND OSMIUM-RUTHENIUM NOBLE METAL FILMS

Nanostructured noble metals exhibit novel physical, mechanical and chemical behavior, and hold promise for applications such as gas sensing and electron emission. A strong emphasis was placed on the processing and characterization of these materials, in the form of nanoporous or nanocrystalline thin films. Palladium-based and osmium-ruthenium alloys were investigated in this dissertation research and will be presented as follows:

(1) Preparation and Characterization of Nanoporous Metal Thin Films
(2) Characterization of Osmium-Ruthenium Coatings

Nanoporous palladium (np-Pd) thin films were prepared by dealloying co-sputtered palladium-nickel precursor alloys. Nanoporous structures were created with 3-D interconnected ligaments and open pores. Size of ligaments and pores was ~5 nm, achieved with a novel processing method developed in this study. Hydrogen cycling tests performed with np-Pd films demonstrated a significant improvement in sensitivity to hydrogen and response time for sensing. Effects of alloying element (Ni), film thickness, local stress and pore/ligament size on hydrogen cycling behavior were investigated in detail. Additionally, nanoporous gold and gold-palladium thin films were studied to clarify the evolution of microstructure during dealloying, including the formation of nanoporous structure and effects of substrate curvature on dealloying behavior. The results from this project have yielded a new understanding of dealloying as well as an ideal coating material for hydrogen sensing.

Nanocrystalline osmium-ruthenium (Os-Ru) thin films were deposited on porous tungsten substrates with varied sputtering parameters. These parameters were mapped to microstructure, film texture and film composition in samples that were comparable to commercial devices. Using this map, Os-Ru films can be produced with higher stability during annealing and/or high-temperature operation. These results should lead to Os-Ru top coatings that increase the lifetime and emission performance of dispenser cathodes.

KEYWORDS: nanoporous, palladium, dealloying, osmium, ruthenium

Wen-Chung Li
Student’s Signature

December 21, 2009
Date

MICROSTRUCTURAL EVOLUTION AND PHYSICAL BEHAVIOR OF PALLADIUM AND OSMIUM-RUTHENIUM NOBLE METAL FILMS

By

Wen-Chung Li

T. John Balk, Ph. D.
Director of Dissertation

Stephen E. Rankin, Ph. D.
Director of Graduate Studies

December 21, 2009

RULES FOR THE USE OF DISSERTATIONS

Unpublished dissertations submitted for the Doctor's degree and deposited in the University of Kentucky Library are as a rule open for inspection, but are to be used only with due regard to the rights of the authors.

Bibliographical references may be noted, but quotations or summaries of parts may be published only with the permission of the author, and with the usual scholarly acknowledgments.

Extensive copying or publication of the dissertation in whole or in part also requires the consent of the Dean of the Graduate School of the University of Kentucky.

A library that borrows this dissertation for use by its patrons is expected to secure the signature of each user.

Name Date

DISSERTATION

Wen-Chung Li

The Graduate School

University of Kentucky

2009

MICROSTRUCTURAL EVOLUTION AND PHYSICAL BEHAVIOR OF PALLADIUM AND OSMIUM-RUTHENIUM NOBLE METAL FILMS

DISSERTATION

A dissertation submitted in partial fulfillment of the
requirements for the degree of Doctor of Philosophy in the
College of Engineering
at the University of Kentucky

By
Wen-Chung Li

Lexington, Kentucky

Director: Dr. T. John Balk, Professor of Chemical and Materials Engineering

Lexington, Kentucky

2009

ProQuest LLC.
789 East Eisenhower Parkway
P.O. Box 1346
Ann Arbor, MI 48106 - 1346

ACKNOWLEDGMENTS

I had a dream that I want to be a great scientist when I was a child, and I think I am a lucky guy who is still possible to fulfill his childhood dream when he has grown up. Completing the PhD study is a critical step for making the dream to come true. There are many people whom I want to thank because they help and support me a lot for the important step because my PhD study could not be done without their help.

Dr. T. John Balk, a young gentleman, is the most important person who supports me as not only an academic advisor but also a good friend every moment in my life at the University of Kentucky. Dr. Balk knows how to give me a hand very well when I lost my way in the materials world although he is a young professor. His talent, knowledge, patience and positive attitude have guided me to be a great scientist. I also want to thank Dr. Balk's family, especially to his parents (Thomas and Michele) and his wife (Ilka), because they always take care of me as their family member. It is not easy that a foreign student wants to adapt his new life in a different environment. However, Dr. Balk and his family let me feel that I am not alone when I faced challenges.

I also deeply appreciate all members of my committee: Dr. Kimberly W. Anderson, Dr. Alan T. Male, Dr. Bruce Hinds, Dr. Fu-Qian Yang and Dr. J. Todd Hastings for their helpful suggestions. I thank them for agreeing with being my committee members and their time spending on my study. Especially, I thank Dr. Yang for his encouragement and concern about helping me in adapting my study life at the UK.

I want to thank Dr. Ye Sun who was my colleague during the first three years in Dr. Balk's group and is my best friend forever. He is always the person whom I can discuss experiments with and share my feeling with. I also thank my other colleagues for their help in my study: Simone C. Schendel, Thomas König, Elizabeth Fadde and Phillip D. Swartzentruber. In addition, I would like to send my thankfulness to my classmates who accompanied me when I needed someone's help: Ashley Brinegar, Bin-Hui Wang, Xue-Bei Shi, Bing Hu, and all people who have ever helped me out.

I thank Dr. Shun-Tian Lin who is the advisor of my M.S. study and pushed me toward my dream. I also deeply appreciate Mr. Pat Chiao and Dr. Herng-Der Chiou for their kind support and long-term encouragement.

I want to send my best gratitude to my family, especially to my parents. Without their support, I could not come to the US and take four and half years for fulfilling my childhood dream. There is no doubt that my wife, Shu-Ping (Aikey) Lin, is the person whom I want to send my greatest gratitude. To her, this is not only acknowledgement but also the firmest love and promise of all my life. Finally, I thank the God for giving me the best gift – Ashley L. Li, my dear princess, in the year of my graduation. She has been the most important force driving me to a more successful future.

Thank all the people who have ever helped me out and supported me!!

TABLE OF CONTENTS

LIST OF TABLES

LIST OF FIGURES

LIST OF FILES

WenChungLiDissertation.pdf	8.4 MB

Chapter 1

Introduction

This dissertation focused on two material systems: *nanoporous Pd-based alloy* and *osmium-ruthenium (Os-Ru)* thin films. Pd, Au, Os and Ru are noble metals and have unique properties. For example, Pd has high reactivity with H_2 and can be used as a sensing material in H_2 sensing devices. Os-Ru is capable to be the coating material in thermionic dispenser cathodes for decreasing the work function of a tungsten (W) diode. In order to improve performance of the devices, i.e. H_2 sensors and dispenser cathodes, these two material systems were systematically investigated in the study.

1.1 Introduction of Np-Pd Films

At atmospheric pressure and room temperature, Pd can absorb 900 times its own volume of H_2 in its lattices with no transformation of the lattice structure [1]. The absorbed H atoms can be desorbed when the Pd is heated at elevated temperatures or in an atmosphere with low H_2 partial pressures. During the absorption of H_2 in Pd, H_2 molecules firstly need physisorption on the Pd surface, and the physisorbed H_2 can sequentially dissociate into two H atoms and chemisorb with the surface Pd atoms. The H atoms occupy octahedral sites in the face-centered cubic (FCC) structure of Pd. In addition, the H atoms can reside in locations of structural defects in Pd, such as grain boundaries, dislocation cores and vacancies [2].

Due to its high reactivity with H_2, Pd is considered as a good candidate material for applications of H_2 storage, purification and sensing [3]. For the applications, surface area (or reaction front) plays a critical role to the interaction between Pd and H_2. For improving the H/Pd interaction, high surface-to-volume ratio is a key factor. In order to increase the surface-to-volume ratio, many investigators have paid attention on structuring Pd in several forms: nanoparticles-decorated nanowires/nanotubes [4-6], nanocrystals [7-9], thin films [10-12] and thin films coated on a nanoporous template (e.g. anodic alumina) [13-15]. However, Pd nanoparticles have high surface-to-volume ratio, but limited intrinsic mechanical stability. Conversely, nanocrystalline Pd and Pd thin films coated on either a flat substrate or a porous template offer improved mechanical stability, but low surface-to-volume ratio. In this dissertation, Pd was prepared as nanoporous thin films, which can have good mechanical stability and high surface area.

Dealloying (or selective dissolution) is a reliable process for making porous materials. It is a process to leach out one (or more) elements from an alloy using a proper etchant solution. Under an appropriate dealloying condition, the porous material can be produced with ligaments and pores from several to tens of nm [16]. Due to its high reliability and simplicity, dealloying has been applied to produce a variety of nanoporous metals in bulk form, thin films, or even nanowires, with nanoporous gold (np-Au) [17-21], palladium (np-Pd) [22, 23], copper (np-Cu) [24] and nickel (np-Ni) [25] as examples. In the study, dealloying is the method applied to prepare np-Pd thin films from Pd-based precursor alloys.

Many factors can affect the final nanoporous structure produced by dealloying, such as alloying elements and composition of the precursor alloy, temperature and concentration of the etchant solution, and dealloying time. In addition, microstructure of the np-Pd can directly and significantly influence sensitivity and capability of H_2 absorption and desorption. Effects of the dealloying parameters on the produced nanoporous structure, mechanisms of dealloying, and mechanisms of H_2 absorption and desorption will be discussed in more detail in Chapter 2. Also, relevant results and discussion of the effects and mechanisms will be presented in this dissertation to clarify some scientific issues of dealloying and H_2 absorption and desorption in the nanostructured Pd. Furthermore, in order to achieve finer nanoporous structure of the np-Pd, novel processing methods are proposed and discussed in this dissertation.

1.2 Introduction of Nanocrystalline Os-Ru Films

A typical thermionic dispenser cathode used by Semicon Associates, the industrial cooperator for the Os-Ru project, mainly contains the heating elements at the bottom and an emitting unit at the top of the cathode (see schematic in Figure 1.1). The emitting unit is a barium (Ba) calcium aluminate impregnated porous W pellet [26-28] inserted in a molybdenum cup. The W pellet is coated with an Os-Ru layer. During operation, the heating elements can heat up the emitting unit to temperatures high enough to overcome the work function of the emitting surface for electron emission. The Os-Ru coating can effectively decrease the work function of the impregnated W from 2.1 eV to 1.85 eV [29, 30]. The decrease in work function can desirably lower operation temperatures of the cathode, and lead the cathode to obtain longer lifetime.

Two factors can shorten cathode lifetime: depletion of the Ba impregnant and degradation of the Os-Ru coating. As Semicon Associates' experience in operating the cathodes, there is almost no cathode failed due to depletion of the Ba impregnant. Instead, degradation of the Os-Ru coating is the primary killing issue to failure of the cathodes. The coating degradation is because of excessive interdiffusion between the W substrate and the Os-Ru coating during high temperature operation which eventually causes loss of emission capability [31-33].

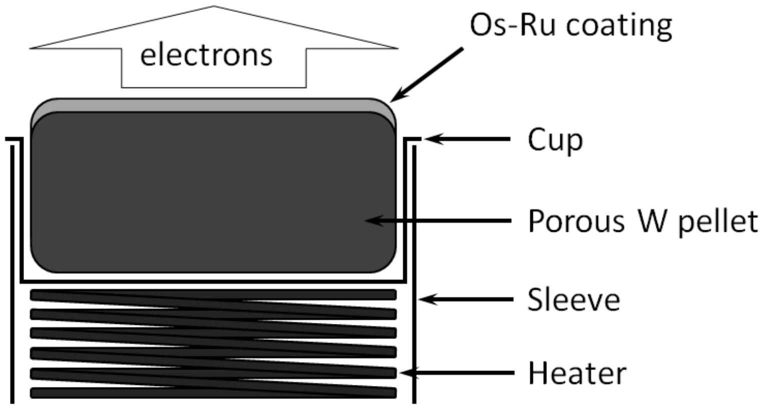

Figure 1.1 Schematic of the typical design of a thermionic dispenser cathode used by Semicon Associates. An Os-Ru thin film was coated on the porous W pellet on the heating element.

There are two types of diffusion paths for the W diffusion through the Os-Ru coating layer: volume diffusion by penetrating lattices of the Os-Ru structure and short circuit diffusion along grain boundaries in the Os-Ru layer. In the case of W diffusion, the diffusion coefficient is closely related to microstructure of the Os-Ru film, such as grain structure and film texture. However, only a little attention has been paid to the microstructure of the Os-Ru coating and its evolution at high temperatures. Some studies characterized the film composition [34-38], and some studies observed film morphology [34, 39, 40]. The proposed results were not sufficient to clarify and even limit the W interdiffusion in the Os-Ru coatings.

Because the cathodes are mostly used in military and space-based applications, where do not allow replacing the cathodes if they failed, reliability and lifetime are of the foremost importance for the cathodes. For inhibiting the interdiffusion of W in the Os-Ru coating, deposition parameters were tuned for obtaining the Os-Ru coating with the highest stability of microstructure, film texture and composition during annealing. The results were discussed based on the point of view of materials engineering in this dissertation.

1.3 Hypotheses

In the study, two primary hypotheses were proposed as below. The hypotheses were investigated by systematical experiments and will be discussed in this dissertation.

- *Nanoporous Pd-based alloy thin films can provide a high surface-to-volume ratio. It is hypothesized that the high amount of surface area might enhance physisorption, dissociation and chemisorption of* H_2 *to surfaces of the Pd-based alloy. The enhanced reactivity of nanoporous Pd-based alloy thin films to* H_2 *might be able to improve rates of H absorption and desorption because rates of phase transformation between* α*-*PdH_x *and* β*-*PdH_x *might be accelerated due to increasing of surface area. However, as the phase diagram of the Pd-H system, capability of H in a nanostructured Pd-based alloy may be sacrificed due to decreasing of the Pd crystal size. Sensitivity and capability of H absorption and desorption in nanoporous Pd-based alloy films will be presented in the study.*

- *Texture and microstructure of Os-Ru thin films might be changed with substrate biasing applied all the time during film deposition. Primary mechanisms of W diffusion in Os-Ru thin films are grain boundary diffusion and bulk diffusion. It is hypothesized that alterations in film texture and microstructure (e.g. grain structure) can change rates of W diffusion and an optimized biasing power might be able to inhibit W diffusion from the W substrate into the Os-Ru film.*

Chapter 2

Background

Both nanoporous Pd-based alloys and Os-Ru are nanocrystalline thin films. The nanocrystalline structure can present physical and chemical properties different from the material in a bulk form, such as reactivity to H_2 and electron emission. The studies described in Chapter 1 involve two material systems: *nanoporous Pd-based alloy* (np-Pd, np-AuPd and np-PdNi) and *Os-Ru thin films*. For the study of nanoporous Pd-based alloy thin films, np-AuPd thin films were used to investigate effects of dealloying parameters on the final nanoporous structure. The np-Pd and np-PdNi thin films were selected to study H_2 absorption and desorption behavior. Additionally, Os-Ru thin films were utilized to clarify effects of sputtering parameters of the film deposition on the film texture, microstructure and stability of the film during annealing.

This chapter will review literatures relevant to the issues presented in the dissertation. Sections 2.1-3 describe applications of Pd-based alloy thin films, mechanisms of dealloying, and hydridation/dehydridation behavior of the np-Pd and np-PdNi thin films. Sections 2.4 and 2.5 present applications of Os-Ru thin films and W interdiffusion in the Os-Ru films, respectively. Note that the np-Pd and np-PdNi are new materials, and no literatures reported the materials before this dissertation (only one study presents np-Pd in a bulk form [1]). So, some literatures mentioned in this chapter are for clarifying theories, processing principles and even new ideas although the literatures present different material systems from np-Pd and np-PdNi thin films.

2.1 Applications of Pd-based Alloy Thin Films

2.1.1 Electrode Material of Fuel Cells

Pd can be a good material for H_2 storage, purification and sensing due to its high reactivity to H_2 at room and low temperatures. Pd [2] and Pd-based alloys (e.g. PdPt [3, 4] and PdPtRu [4]) are also considered to be used in proton exchange membrane fuel cells (PEMFCs) as an H-catalyzed material for the electrodes. In a typical PEMFC, the layered structure contains anode gas diffuser, anode electrode, anode catalyst, PEM layer, cathode catalyst, cathode electrode and cathode gas diffuser [5] from the anode side to the cathode side. The assembled unit in a PEMFC is the energy generation unit. Gas channel structures are attached to the anode and cathode for guiding H_2 to the anode and O_2 to the cathode. H and O ions combine at the cathode catalyst layer to form water as waste byproducts.

For enhancing utilization efficiency of H_2 input from the anode gas channels, materials of the anode require to rapidly adsorb and dissociate H_2 molecules. Carbon-supported Pd [2] and PdPt [4] nanoparticles were used as the anode materials because the nanocrystalline Pd and PdPt have high reactivity with H_2 due to the high amount of surface area (particle size: 4.6-12.2 nm [4]). The material(s) is widely used as anode sets in most current PEMFCs.

Erdler et al. [6] proposed a novel idea that Pd was used as the H storing material in an integrated fuel cell chip. The H-loaded Pd reservoir was setup as the anode directly attached to the PEM, which is a different design from the current PEMFCs. As electrical performance tests for the fuel cell chip, the result shows that the single fuel cell chip operated with a voltage higher than 0.4 V for ~160 hrs (most PEMFCs with voltage output of 0.5-1.0 V [5]). The chip fuel cell shows a strong potential for using the chips as the power source of micro-actuators or the stacked chips for high-power devices although current density of the single chip was several orders lower than regular PEMFC modules.

For the application of PEMFCs, np-Pd and/or np-PdNi thin films might be able for using as the anode materials because the thin films have high reactivity to H_2, high surface area and high intrinsic mechanical stability than the carbon-supported nanoparticles. Furthermore, interconnected ligaments in the np-Pd and np-PdNi films should be able to provide channels for proton transportation to the PEM. So, it is suggested that np-Pd and/or np-PdNi thin films might be a good candidate material for building the anode structure although no literatures have pointed out this novel idea so far.

2.1.2 H_2 Sensors

Comparing with traditional H_2 sensors using a flat Pd thin film as the sensing material, Pd mesowires [7, 8], nanofibers [9, 10] and Pd-decorated carbon nanotubes [11] have been proposed to improve performance of H_2 sensors, especially shortening their response time. The improvement is attributed to increase in Pd surface area. Current H_2 sensors mostly measure changes in either electrical resistance or optical transmittance of the Pd crystals during H_2 absorption and desorption to read H_2 content in the atmosphere. Baselt et al. [12] designed a Pd-coated micro-cantilever H_2 sensor, and the cantilever can be bent downward when the Pd film absorbed H_2. The H_2 content can be detected by reading changes in capacitance between the cantilever and the base-plate. However, all types of Pd-based sensing unit mentioned above are coated by Pd thin films, which can limit sensitivity to H_2 due to the restricted surface area of Pd.

For increasing the sensing performance (e.g. response time and accurate quantification of H_2 content), the Pd structure with high surface area is desired. Ding et al. [13-15] deposited Pd thin films on a nanoporous anodic alumina substrate as the sensing material. Similarly, Luongo et al. [16] deposited Pd thin films on a porous silicon substrate to increase surface area of Pd. As their results, performance of the H_2 sensors using a Pd-coated porous substrate was improved significantly.

All current H_2 sensors utilize the measurements of changes in electrical resistance, optical transmittance and even volume of the Pd structure to detect H_2 content. As principles of the measurements, the np-Pd and np-PdNi thin films might be used in H_2 sensors because the films have interconnected Pd (or PdNi) ligaments and uniform film thickness, which can provide the measurements with great accuracy. In addition, surface area of the np-Pd and np-PdNi thin films is much higher than the sensing materials mentioned above. So, using np-Pd and/or np-PdNi thin films as the sensing material in H_2 sensors may improve performance of the H_2 sensors.

2.2 Dealloying

2.2.1 Selection of Precursor Alloys and Etchant Solutions

Selecting an appropriate precursor alloy is the first and important class for producing nanoporous metals by dealloying. Two conditions are generally desired (in cases of binary alloys):

(1) Two alloyed elements are miscible with no extra phases, e.g. intermetallics.

(2) Two alloyed elements have the same lattice structure.

Np-Au is a typical example presenting the nanoporous structure produced by dealloying. For most cases of preparing np-Au, AuAg is used as the precursor alloy for dealloying [17-29] because Au and Ag are miscible with any compositions and have the same FCC lattice structure. Kabius et al. [1] used PdCu (20 at.% Pd) as the precursor alloy for preparing np-Pd by dealloying. Sun et al. [30] prepared np-Ni by dealloying the NiCu precursor alloy.

Once the precursor alloy is decided, an appropriate etchant solution needed to be selected by high dissolution selectivity for the alloyed elements. Dealloying methods can be with or without applied voltage. Dealloying with applied voltage is an electrochemical process. Also, the precursor alloy can be dealloyed as free corrosion in the etchant solution with no voltage applied. Free corrosion and electrochemical dealloying are able to be combined for obtaining the nanoporous metal with a lower amount of the sacrificial element. For all the approaches of dealloying, the etchant solution should be able to leach out the less noble element, but does not attack the more noble element. For the requirement of high dissolution selectivity, HNO_3 is the ideal etchant solution for dealloying of AuAg to prepare np-Au [17-29]. Kabius et al. [1] electrochemically dealloyed the PdCu precursor alloy in a Na_2SO_4+H_2SO_4 solution (1 N, pH 2). Using an appropriate precursor alloy and etchant solution, the porosity can be as fine as several nm, and content of the sacrificial element can be lower than 10 at.%.

The np-Pd and np-PdNi thin films presented in this dissertation were prepared by free corrosion of Pd-based alloys. Selections of the final precursor alloy and etchant solution will be discussed in the next chapter.

2.2.2 Mechanisms of Dealloying

A selected precursor alloy contains the more noble (MN) element and the less nobel (LN) element. During dealloying, the LN element is leached out the precursor alloy and the MN element can agglomerate to form clusters. Erlebacher [31] proposed a kinetic Monte Carlo model to clarify dealloying evolution via an atomistic view. In his simulated model, when the topmost atomic layer of the precursor alloy was attacked by the etchant solution, dissolution of the LN atoms and diffusion of the MN atoms occurred at the alloy/solution interface, where was with a non-equilibrium state. The LN atoms at the etching front dissolved in the solution and remained vacancies in the topmost atomic layer. The MN atoms preferred to agglomerate into clusters for satisfying the stable atomic coordination. By the time, the next atomic layer was exposed to the solution. The dissolution/diffusion behavior can proceed repeatedly until forming a nanoporous structure with a low amount of the LN element. However, dealloying can stop when the etching front was completely passivated by the MN atoms, which led all atoms beneath the topmost atomic layer to be protected from the solution attacking. The passivation phenomenon of dealloying can be verified by changing compositions of the precursor alloy [27].

In Erlebacher's model [31], diffusion distance of the MN atoms along the surface (or the etching front) should be shorter than the length scale between neighboring ligaments/clusters (λ). In other words, both ligaments and pores are formed in localized regions. Using applied potential during dealloying, rates of the dissolution ($k_{dissolution}$) and the surface diffusion ($k_{diffusion}$) were summarized as equations 2.1 and 2.2.

$$k_{dissolution} = \nu_E \exp\left[-\left(nE_b - \phi\right) / k_B T\right] \tag{2.1}$$

$$k_{diffusion} = \nu_D \exp\left(-nE_b / k_B T\right) \tag{2.2}$$

Here, ν_E is a given frequency of 10^4 s^{-1}. ν_D is an attempt frequency of order of the Debye frequency (10^{13} s^{-1}, for most metals). E_b is the bond energy between the LN and MN atoms, which is 0.15 eV for Ag and Au atoms in AuAg alloys. “n” is the amount of neighboring atoms for the given LN or MN atom at the etching front. The n value is in a range of 3-9, depending on locations of the given atom (e.g. steps or kinks). k_b is the Boltzmann Constant and T is the temperature (K).

As equations 2.1 and 2.2, both dissolution of the LN atoms and surface diffusion of the MN atoms require overcoming an activation barrier of (nE_b). Applying a high potential can enhance dissolution of the LN atoms but cannot affect diffusion rate of the MN atoms. However, these two equations are not able to estimate rates of dissolution and surface diffusion in the case of free corrosion (no applied voltage).

For estimating surface diffusion rates of Au atoms on the Au surface (same as the case of free corrosion of AuAg alloys), Andreasen et al. [32] quantified surface diffusion rate of Au atoms on Au particle surface in H_2SO_4 (0.5 M) of 1.5×10^{14} cm^2/s by equation 2.3.

$$D_s = \frac{d(t)^4 k_b T}{32\gamma t a^4} \tag{2.3}$$

where d is the particle size, t is particle coarsening time, T is the temperature (K), γ is surface energy of the particles, and a is the lattice parameter of Au. Using the D_s value , Qian and Chen [33] estimated ligament coarsening rates of np-Au during dealloying of the AuAg alloy by equation 2.4.

$$d(t)^n = k_0 t \exp\left(\frac{-E}{RT}\right) = KtD_s \tag{2.4}$$

where d is the pore diameter, t is dealloying time, and T is temperature (K). K, k_0 and R are constants (K: proportional constant, $k_0 = KD_0$, R: gas constant). Qian and Chen obtained the n value is 3.4-3.7, which is close to the value of 4 calculated by Dona and Gonzalez-Velasco [34].

Erlerbacher and Sieradzki [35] also proposed a description for pattern formation of the nanoporous metal during dealloying. In their study, formation of ligament/cluster was described in a 3-D space. The MN atoms agglomerate into the neighboring clusters by traveling a distance shorter than λ. With subsequent dissolution, the MN atoms need to travel a longer distance for agglomeration due to undercutting of the clusters. When the traveling distance is longer than λ, the MN atoms at the newly formed etching front prefer to nucleate. Subsequently, the new nucleus can grow as new clusters by collecting the neighboring MN atoms. With formation of more new clusters, curved pores are created in the porous structure.

For pattern formation of the nanoporous structure, Sieradzki et al. [36, 37] presented a percolating model for dealloying a binary alloy. As their model, the MN and LN atoms were not uniformly dispersed in the precursor alloy, which means clusters of the MN and LN atoms were pre-existed before dealloying. Dissolution of the pre-existed LN clusters causes subsequent dissolution along penetration paths into the precursor alloy. By the time, the MN atoms can agglomerate into pre-existed MN clusters, with no demand of nucleation of the MN clusters.

2.2.3 Effects on Nanoporous Structures

As mentioned in Section 2.2.2, an over amount of the MN atoms can terminate dealloying due to a completely passivated etching front. However, the final nanoporous structure can crack when the amount of the MN atoms is too low [29]. Lu et al. [27] used a thin film specimen with a compositional gradient in the precursor AuAg alloy (Au: 22-45 at.%, 1.6 μm thick) to study effects of the alloy composition on the dealloyed porous structure (np-Au). An open nanoporous structure of the np-Au with a low amount of remnant Ag content (4 at.%) was obtained after dealloying when Au content in the precursor alloy were 22-26 at.%. However, only the grain boundaries can be dealloyed when the Au content was higher than 36 at.%, leading the dealloyed np-Au structure to retain the AuAg alloy clusters. Cracks were observed in the np-Au thin film when the original Au content was (and lower than) 24 at.%. It is suggested that 25-35 at.% Au was the optimal composition of the AuAg alloy.

During dealloying, volume of the precursor alloy can contract due to loss of the LN atoms. Parida et al. [22] used AuAg leaf samples to measure the volume change by a contraction of 30 % during dealloying. Sun and Balk [29] presented the AuAg thin films contracted by ~15 % in the film thickness and 9 % in biaxial orientations during dealloying. However, volume contractions during dealloying can be avoided by tuning dealloying rates. Sun and Balk [38] proposed a multi-step dealloying method for dealloying the AuAg alloy (in bulk) with no volume change. The proposed method involves two steps: dealloyed in 1:2 diluted HNO_3 for 70 hrs then in concentrated HNO_3 (70 %, stock solution) for 10 hrs. Using the multi-step dealloying, most Ag atoms were removed at a moderate dissolution rate firstly, allowing the structure to maintain the original dimensions and shape with formation of some nanoporosity. Subsequently, the remnant Ag atoms were leached out more rapidly with no change in the structural dimension.

Qian and Chen [33] changed dealloying temperatures to study the effects on the np-Au produced from the AuAg alloy. After dealloying in concentrated HNO_3 (70 %, stock solution) for 4 hrs, diameter of pores was 6, 15 and 27 nm when dealloying temperature was -20°C, 0°C and 25°C, respectively. With the increase in pore diameter, ligaments also coarsened significantly (ligament widths: 7-12 nm).

The final nanoporous structure is closely related to the balancing between dissolution rate of the LN element and surface diffusion rate of the MN element. Both studies by Sun and Balk [38] and Qian and Chen [33] tuned dealloying rates by changing either concentration of the etchant solution or dealloying temperatures. The final nanoporous structure can be affected significantly. In addition to the reported dealloying parameters that can affect the nanoporous structure, effects of the substrate curvature on the np-AuPd ultrathin films were investigated in this dissertation. Also, surfactants were added to the etchant solution for achieving a finer nanoporosity. The issues were not reported by any groups before, and the results will be presented in Chapters 5 and 6. Furthermore, this dissertation will present morphological observation for the bottommost layer of ligaments to clarify formation of a nanoporous structure in Chapter 7.

2.3 Hydridation and Dehydridation of Pd

2.3.1 H in Bulk Pd

Physisorption of H_2 molecules on the Pd surface is closely dependent on both pressure and temperature. When the physisorption occurs, H_2 molecules adhere to the Pd surface by van der Waals forces and/or electrostatic attraction with a binding energy of 1-5 kJ/mol [39]. Coverage ratio of the adsorbed H_2 molecules is a function of H_2 pressure, binding energy, temperature and a rate constant. The rate constant can be seen as sticking coefficient, presenting a ratio of non-activated (stuck) H_2 molecules to activated H_2 molecules. The higher coverage ratio is desired for followed dissociation of H_2 molecules.

Mitsui et al. [40] used scanning tunneling microscopy (STM) to investigate H_2 adsorption and dissociation behavior on a Pd (111) surface. The STM result shows that a success of H_2 adsorption and dissociation on the Pd surface requires aggregates of three of more vacancies. In other words, there should be a limit value for the coverage ratio of H_2 on the Pd surface. Based on density functional theory, Lopez et al. [41] proposed a similar result that formation of an "active site" for H_2 adsorption and dissociation requires aggregation of at least three H-free tetrahedral sites on the Pd (111) surface.

Once H_2 molecules successfully physisorbed and dissociated into H atoms at tetrahedral sites on the Pd surface, the H atoms can be chemisorbed with a strong binding energy (>50 kJ/mol [42]). Subsequently, the chemisorbed H atoms penetrate the topmost layer of Pd atoms to reside at octahedral sites in Pd lattices as interstitial absorbates. With the increasing of H content in the Pd, interaction between neighboring H atoms increases because the H-contained Pd lattices expand, causing a high interfacial energy between the expanded lattice and the neighboring un-expanded lattice. For decreasing the interfacial energy, H atoms prefer to reside in the Pd lattice next to an expanded Pd lattice. So, the second phase of PdH_x is formed by H aggregation in Pd.

Figure 2.1 schematically shows pressure-composition isothermal diagram of Pd-H system. There is a miscibility gap between α- and β-PdH_x, and critical temperature (T_C) is 570K [43, 44]. H content of α- and β-PdH_x is $x = 0.015$ (Point A in Figure 2.1) and 0.58 (Point B), respectively. Both phases have the same FCC crystal structure but present different lattice parameters, varying from 0.389 nm to 0.403 nm with increasing of H content [45, 46]. Lasser and Klatt [47] proposed a theoretical x_{max} value of 0.703 at 1 atm and room temperature. However, no experimental study reported x values higher than 0.6 under the condition of atmospheric pressure and room temperature. Schirber and Morosin [48] presented ultrahigh H-contained β-PdH_x (x near 1.0) with a lattice parameter of 0.408 nm under an extreme condition ($T = 77K$, $P = 5 \times 10^8$ Pa). XRD results show that the ultrahigh H-contained β-PdH_x still maintained the FCC lattice structure and the lattice parameter was linearly increased with increasing of H content.

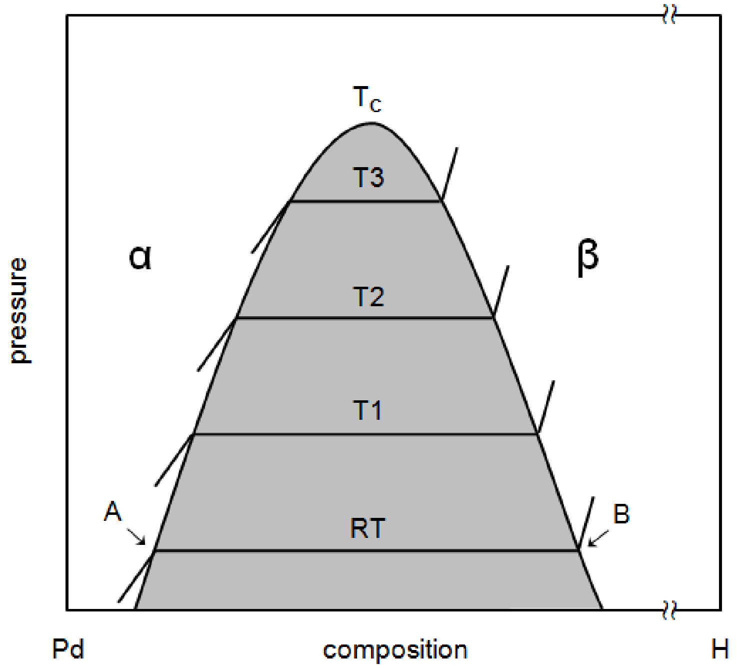

Figure 2.1 Schematic of pressure-composition isothermal diagram of the Pd-H system.

In addition to tetrahedral site on Pd surfaces and octahedral site in Pd lattices, H atoms can reside at/near defects, including dislocation cores and grain boundaries, due to tensile stress and disordered atomic arrangement in the local regions [49]. Nechaev [50] used deformed and annealed bulk Pd specimens to investigate H segregation near dislocations. Due to the nature of H segregation behavior, it is proposed that region near dislocations can form a local hydride-like phase along the dislocations with a diameter up to several nm although the Pd specimens have a low H content. Lemier and Weissmuller [51] used nanocrystalline Pd to study H segregation at grain boundaries. The result indicated that H segregation at grain boundaries was dominant although H content in the Pd was very low (α phase), which agrees with Mutschele and Kirchheim's statement [52].

Oriani [53] compared values of interaction enthalpies of the dissolved H atoms at edge dislocations (-60 to -70 kJ/mol [54, 55]) and grain boundaries (-5.3 kJ/mol [52]) in bulk Pd. It is suggested that the dissolved H atoms might not be able to be desorbed from edge dislocations as easy as grain boundaries when change in interaction entropies of edge dislocations and grain boundaries was negligible because interaction enthalpy of edge dislocations was one order higher than grain boundaries. However, value of the interaction entropies was not presented in their studies. Pundt et al. [49, 56] also proposed that edge dislocations can offer tensile deformed lattices near the dislocation core beneath the dislocation gliding plane for easy occupation of H atoms.

2.3.2 H in Nanostructured Pd

For applications using Pd as an H sensing material, Pd usually requires to be structured in nanoscale for improving its sensitivity. However, H capability of Pd may be sacrificed with the size reduction of Pd crystallites. This concern was firstly proposed by Eastman et al. based on their thermodynamics calculations [57]. Kuji et al. [58] presented pressure-composition isothermal curves of the Pd-H system using annealed Pd sheets with coarse grains and fine Pd particles (particle size: ~200 μm), and a narrower miscibility gap between α- and β-PdH_x was exhibited by fine Pd particles. For the Pd sheets, x value at Points A and B in Figure 2.1 was 0.02 and 0.57, respectively, which agrees with H solubility measured in bulk Pd [45]. However, for the Pd particles, H solubility in α-PdH_x increased (x = 0.05, at Point A) and H content in β-PdH_x decreased (x = 0.52, at Point B). Kuji et al. [59] used nanocrystalline Pd (grain size: ~10 nm) to investigate effects of Pd crystallite size on H capacity. X value of α- and β-PdH_x in the nanocrystalline Pd was 0.1 and 0.32, respectively. In addition, T_C of the miscibility gap decreased to 435K (570K for bulk Pd). As the result, it is noted that H solubility can increase in α-PdH$_x$ but decrease in β-PdH$_x$ when Pd is nano-sized.

This finding of the narrowed miscibility gap in nanocrystalline Pd can be considered to a higher degree of atomic disorder in the lattices at/near Pd surfaces. For nano-sized Pd, surface tension of Pd can deform the Pd lattices near the surface, but degree of the lattice deformation can decrease with increasing of distance from the surface. The deformed Pd lattices can cause a higher difficulty in H occupation at the octahedral sites. Kishore et al. [60] utilized spherical Pd nanoparticles (particles size: 4-5 nm) to estimate that 68-69% Pd lattices behaved as the surface/subsurface lattices (i.e. 31-32% as bulk-like lattices). Kuji et al. [59] proposed an explanation for the sacrifice of H capability in nano-sized Pd that the deformed lattices led the certain octahedral sites to have a smaller effective volume for H occupation, which caused a higher occupation energy and even some octahedral sites in highly deformed lattices being not available for H occupation. Reduction of H capability in β-PdH$_x$ was up to 50% in the nano-sized Pd (grain size: 10 nm).

Additionally, Sachs et al. [61] investigated effects of particle size on H capability of β-PdH$_x$ using surfactant-stabilized Pd nanoparticles. X values of β-PdH$_x$ were approximately 0.2, 0.26 and 0.3 for 2 nm, 3 nm and 5 nm nanoparticles, respectively. Although the x value for 5 nm Pd nanoparticles was not defined well due to lack of data points in between 0.2 and 0.42, the estimated value (0.3) was with a good agreement with 0.32 proposed by Kuji et al. [59]. The reduction of H capability in nanocrystals was also found in other metals/alloys. Jurczyk et al. [62] studied effects of grain size on H capability of magnesium-copper (Mg$_2$Cu) at 573K, and the result showed a 13.5%

reduction (from 2.6 wt.% H to 2.25 wt.% H) when grain size decreased from microns to 30 nm.

For nano-structured Pd, both higher occupation energy and lower amount of octahedral sites cause a lower H capability than bulk Pd. However, some forms of the nano-sized Pd may lead the Pd structure to benefit H absorption. For example, both nanoparticles and nanoporous structure have a high surface curvature. The highly curved surface contains a high amount of surface atoms residing at step edges, kinks and vacancies. Surface atoms near the surface defects have a weaker binding to the subsurface atomic layer because the surface atoms have fewer nearest neighboring atoms. The weaker binding can lead the surface atoms to offer higher reactivity toward dissolved H atoms [42]. Sachs et al. [61] verified that the surface atoms near surface defects (e.g. step corners and edges) can favor additional binding to the dissolved H atoms.

Interestingly, Cox et al. [63] proposed an amazing x value (x = 3) of PdH_x for Pd nanoparticles containing less than 50 atoms, which means the nanoparticles were ~1 nm in particle size. In other words, H atoms can be not only stored at octahedral sites in Pd lattices but also chemisorbed by the surface atoms near surface defects. Considering positions of the stored/chemisorbed H atoms, the chemisorbed H atoms which were hung out of the lattices (actually, anchored on the surface) might not significantly change lattice parameters as the stored H atoms which resided at octahedral sites in Pd lattices. However, the H atoms anchored on the surface can degrade rates of H_2 physisorption and dissociation due to less reaction sites on the highly H-covered surface.

In addition to offering extra positions for H anchoring, the atoms near surface defects can be nucleation sites of β-PdH_x due to the high interaction entropy and high H content in the local region (only several lattices nearest surface defects). For the nano-sized Pd structures with high surface-to-volume ratio (i.e. nanoparticles and nanoporous structure), β-PdH_x is easy to be formed because of the lower H capability (x: ~0.3 for 5 nm Pd but 0.58 for bulk Pd) and high amount of nucleation sites near the highly curved surface. In the nano-sized Pd structures, nucleation density of β-PdH_x near surface can be a critical issue affecting hydridation and dehydeidation behavior. However, not much attention has been given to the issue of nucleation density by experiments.

Asakuma et al. [64] numerically analyzed H absorption and desorption mechanisms with tuning nucleation density of hydride in metal clusters (e.g. β-PdH_x in nano-sized Pd). With a lower nucleation density, every nucleus of β-PdH_x can grow into interior of the metal cluster with no contact with neighboring β-PdH_x cluster until the metal cluster completely transformed to β-PdH_x. Conversely, with a higher nucleation density, a β-PdH_x shell can be formed before the core transformed to the hydride phase. As the result presented by Asakuma et al., it can be addressed that a core-shell structure might be formed during initial stage of hydridation when nucleation density of β-PdH_x is high enough. Furthermore, a higher nucleation density may form a close shell earlier during hydridation, which is supported by the simulation proposed by Crespo et al. [65].

Formation of the core-shell structure in nano-sized Pd, i.e. the α-PdH_x core surrounded by a β-PdH_x shell, can lead subsequent hydridation to be more difficult because diffusion of H atoms in α-PdH_x is faster than in β-PdH_x. After formation of the β-PdH_x shell, H atoms needed for full hydridation require to penetrate the shell with a lower diffusion coefficient. As diffusivity (D_0) and activation energy (E_a) of H diffusion in α-PdH_x [53] and β-PdH_x [66], diffusion coefficients of H in α-PdH_x and β-PdH_x are 3.7 $\times 10^{-7}$ cm^2 s^{-1} and 9.8×10^{-8} cm^2 s^{-1}. Therefore, diffusion rate of H in β-PdH_x is 3.8 times slower than in α-PdH_x, which means subsequent H absorption can take longer time when the β-PdH_x shell is formed.

Both Pd nanoparticles and np-Pd can perform high sensitivity to H_2 due to their high surface area. As worse mechanical stability for H sensing applications, Pd nanoparticles usually require decorating on a substrate, e.g. nanowires or nanotubes. However, the nanoparticle form might have another problem leading to decayed performance after using for long time – H-induced Ostwald ripening. This phenomenon of H-induced Ostwald ripening in Pd nanoparticles was recently proposed by Vece et al. [67]. The ripening phenomenon can cause change in continuity of Pd nanoparticles and reduction of surface area during long-term hydridation.

In this dissertation, np-Pd and np-PdNi thin films were used to investigate hydridation and dehydridation behavior for nano-sized Pd and Pd-based alloys. The result might offer a new sight for investigating H absorption and desorption mechanisms of Pd sized as small as 5 nm (even smaller than 5 nm). Relevant results and discussion will be presented in Chapter 8.

2.4 Os-Ru Thin Film in Dispenser Cathodes

Os-based alloys, including osmium-iridium (Os-Ir) and Os-Ru, were firstly proposed as coating materials used in W-based dispenser cathodes in 1970 [68], which was patented by US Philips Corporation, NY. Emission unit of the cathode was composed of an Os-based alloy coated W pellet, which was prepared by powder metallurgical processing for the mixture of W and BaO-CaO-Al_2O_3 (with a molar ratio of 5:2:3) powders. Although Os can be toxic after oxidation, the Os-based alloy has surface attractive force to tight activated Ba atoms and to polarize the Ba atoms for reducing work function of the cathode.

A similar design of porous W dispenser cathodes was proposed by Falce in 1979 [69]. Using this patented design, lifetime of the cathode was improved to 44,000 hrs (operated at 1050°C_B) with a higher emission density than conventional dispenser cathodes. Cortenraad et al. [70] presented that emission density of porous W dispenser cathode with an Os-Ru coating (80 at.% Os and 20 at.% Ru, 50-500 nm thick) was 30 A cm^{-2}, which is higher than Ir coatings (20 A cm^{-2}) and rhenium (Re) coatings (~15 A cm^{-2}) at T = 1030°C_B. The increase in emission density was corresponded to a lower work function of the cathode with a Os-Ru coating (1.85 eV), comparing to 1.85 eV for Ir coatings and 1.93 eV for Re coatings. Using low-energy ion scattering presented that Os-Ru coatings had the highest Ba ion density (3.5×10^{14} ions cm^{-2}), which was higher than Ir (2.9×10^{14} ions cm^{-2}) and Re (2.7×10^{14} ions cm^{-2}). It is clear that Os-Ru is an ideal material for lowering work function, decreasing operation temperatures and enhancing emission density of the dispenser cathodes.

Os-Ru (or Os) thin films can be deposited by chemical vapor deposition (CVD) [71, 72]. However, deposition requires to be processed at elevated temperatures (e.g. 300°C [71]). The elevated temperatures might affect impregnated BaO-CaO-Al_2O_3 in W pellets. Moreover, precursor materials used for CVD of Os-Ru films are toxic. Therefore, sputtering is a desired method for deposition of Os-Ru films because of processing safety and lower processing temperatures (e.g. room temperature). Microstructure and film texture of Os-Ru can be changed by sputtering parameters, including film thickness, sputtering power, deposition temperature and pressure, distance between the substrate and the target, and power of substrate biasing.

2.5 W Interdiffusion in Os-Ru Thin Films

There are two factors which can limit lifetime and performance of the Os-Ru coated dispenser cathodes: depletion of Ba impregnant and degradation of the Os-Ru film. Depletion of Ba impregnant is caused by evaporation of Ba during high-temperature operation in vacuum. Roquais et al. [73] proposed that evaporation rate of Ba significantly increased with increasing porosity of the porous W substrate (e.g. 22% porosity exhibiting an evaporation rate as 2.6 times higher than 16% porosity). Therefore, higher porosity of the porous W substrate can limit lifetime of the cathodes due to its higher Ba evaporation rate. However, higher porosity can lead the cathode to perform higher emission density [74]. So, porosity of the W substrate should be compromised in between lifetime and performance of the cathodes.

As Semicon Associates' experience, almost none of their cathodes failed due to depletion of Ba impregnant. Instead, failure of most cathodes was caused by excessive diffusion of W in the Os-Ru film. The W diffusion can degrade the top-coating layer. In Os-Ru films, some W (~40 at.%) is needed to enhance electron emission. However, high W content (>80 at.%) in Os-Ru films can cause failure of the cathodes [75]. The excessive amount of W was from interdiffusion between the Os-Ru film and the W substrate during high-temperature operation. So, it is critical for improving lifetime and performance of the cathodes that W diffusion into the Os-Ru film should be hindered during operation.

As-deposited Os-Ru films were polycrystalline. Considering about diffusion of W atoms in the polycrystalline Os-Ru film, there are two types of diffusion paths: volume diffusion and grain boundary diffusion. As volume diffusion, atomic planar density is critical to W diffusion. Film texture can play an important role to affect W diffusion rates. As grain boundary diffusion, grain size can be a key issue for W diffusion rates. Larger grains are desired because the grain structure has fewer grain boundaries as diffusion paths for W atoms.

Crystal structure of Os-Ru is hexagonal close packed (HCP) lattices. Basal plans, i.e. (0002), have the highest planar density. The densest planes can offer a higher resistance for W penetration. In other words, (0002) may be the desired film texture for hindering volume diffusion of W atoms. For decreasing grain boundary diffusion of W, Os-Ru films have to be deposited with larger grains and no cracks. Both issues are relevant to microstructure and texture of Os-Ru films. Unfortunately, not much attention has been paid on microstructure and texture of Os-Ru films.

Jones et al. [76] presented scanning electron microscopy (SEM) micrographs of as-deposited and activated cathode surfaces, but no microstructure of the film was proposed. Isagawa et al. [77] investigated morphology of W surfaces prepared with different processing methods, but no characterization was performed with the film. Several studies characterized surface composition and depth profile using x-ray photoelectron spectroscopy (XPS) or Auger electron spectroscopy (AES) [78-81], but no microstructure of the film was presented.

By cooperating with Semicon Associates, Bell [82] presented a systematical investigation of substrate biasing during film deposition with microstructural and compositional characterizations. As microstructural observation (plan-view and cross-section) and compositional analysis, Bell summarized that a substrate biasing voltage of 50-100 V (DC) can improve stability of film thickness and composition during annealing.

In this dissertation, effects of film thickness and substrate biasing power on microstructure and texture of Os-Ru thin films were investigated by linking to the results of chemical analysis. Stability of film microstructure, texture and composition were compared with specimens provided by Semicon Associates.

Chapter 3

Experiments

This chapter will present general information of experimental methods used in the study. Experiments include thin film deposition (Section 3.1), dealloying (for nanoporous specimens, Section 3.2) and characterization (Section 3.3). Detailed information of experiments will be presented in each chapter of results and discussions (Chapters 4-9).

3.1 Magnetron Sputtering Deposition

Magnetron sputtering offers a high ionization yield to generate plasma for thin film deposition. In a high vacuum sputtering chamber, the ionized argon (Ar) atoms can be driven toward the target surface (precursor material) by electric field, resulting in ejection of target atoms (or atom clusters). Magnetic field ***B*** is perpendicular to electric field ***E*** above the target surface. The electric and magnetic field leads electrons to drift with helical or cycloid paths, which can enhance ionization efficiency of Ar within a circular region of plasma (see Figure 3.1a).

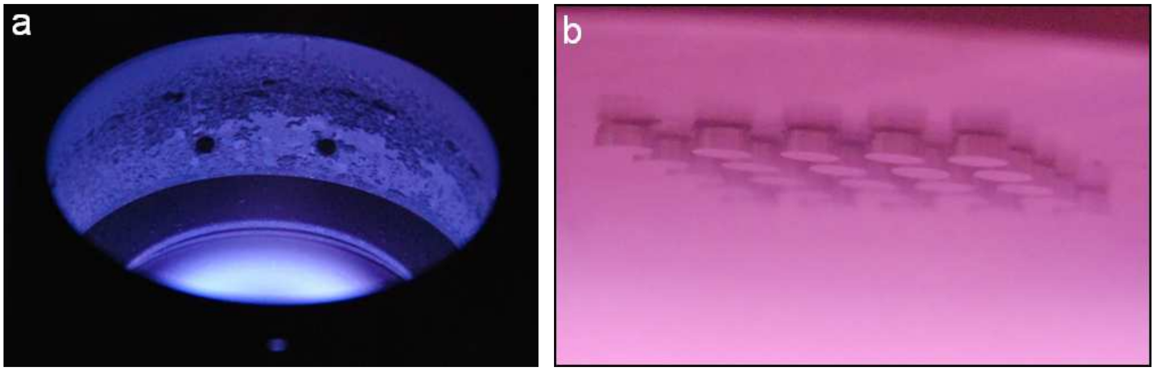

Figure 3.1 Plasma (a) above the target and (b) near the substrate carrier in an Ar atmosphere. The target and substrate are Os-Ru and W pellets, respectively.

During deposition of thin films, substrates can be etched back by Ar^+ ions when the substrate carrier is biased with an applied potential (RF) for generating plasma near the substrate surface. The etching back process is substrate biasing. Substrate biasing can result in high compressive stresses in the as-deposited film and even be able to change the film texture. However, substrate biasing can decrease deposition rate by several percents (e.g. 5% for deposition of Ni films with substrate biasing). Figure 3.1b shows plasma for substrate biasing during film deposition.

In this study, thin films were deposited on substrates using magnetron sputtering (ORION system, AJA International Inc., North Scituate, MA, USA). Substrates included single-crystalline (100)-oriented Si (180 or 380 μm thick, CrysTec GmbH, Berlin, Germany), Kapton sheets (50 μm thick polyimide, DuPont Kapton, type 200 HN) and W pellets. Deposition of thin films was performed in a vacuum chamber (base pressure: 1.3 $\times 10^{-6}$ Pa or 1.0 $\times 10^{-8}$ torr) with an Ar atmosphere at pressure of 2.5 $\times 10^{-3}$ torr. Before deposition, substrates were cleaned by ion etching back with bias power of 35 W (RF) at 2.5 $\times 10^{-2}$ torr for 1.5 min for cleaning the substrate surface and create nucleation sites. Interlayer (e.g. Ta) was deposited for enhancing adhesion of the film to the substrate (e.g. Si). During film deposition, substrate carrier rotated for obtaining a better uniformity of film thickness and composition. Additionally, substrate carrier was biased all the time during film deposition for some specimens.

Target configuration of the ORION system is shown in Figure 3.2. Four targets can be set in the chamber, including Ni (or Ag), Os-Ru (or Pd), Pd (or Au) and Ta. In Figure 3.2, gun 1 was not capped and the target was removed. Thirteen magnets surround the central magnet. These magnets can create a magnetic field above the target, yielding circular plasma on the target surface. Shutters of other three guns are closed. Details of film deposition will be presented below.

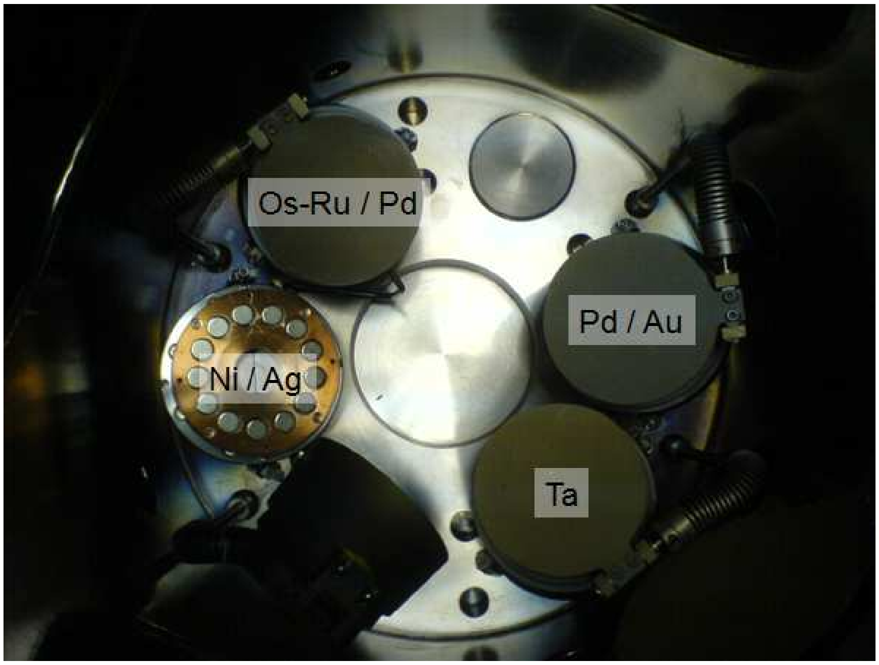

Figure 3.2 Target configuration in the sputtering chamber of the ORION system. Magnets beneath the target can be seen by gun 1 (Ni or Ag), which was not capped.

3.1.1 Deposition of PdNi Precursor Alloy Films

Composition of precursor alloy is critical to the porous structure prepared by dealloying. Film composition of the precursor alloy (e.g. PdNi) can be adjusted by tuning deposition rates of the co-sputtering targets. Deposition rate of each target was determined individually at a given deposition power using a stylus profilometer (Dektak 6M). For obtaining thickness difference on a flat surface, straight lines were drawn by a marker (Sharpie) on surfaces of a glass plate. After film deposition with a certain thickness on the glass plate, specimens were merged in ethanol (95% purity) to dissolve the marker lines. Film over the marker lines became free-standing and eventually was peeled off from the glass surface. By using the profilometer, surface profile and film thickness can be determined with nm scale. Figure 3.3 shows a typical profile over the peeled edge.

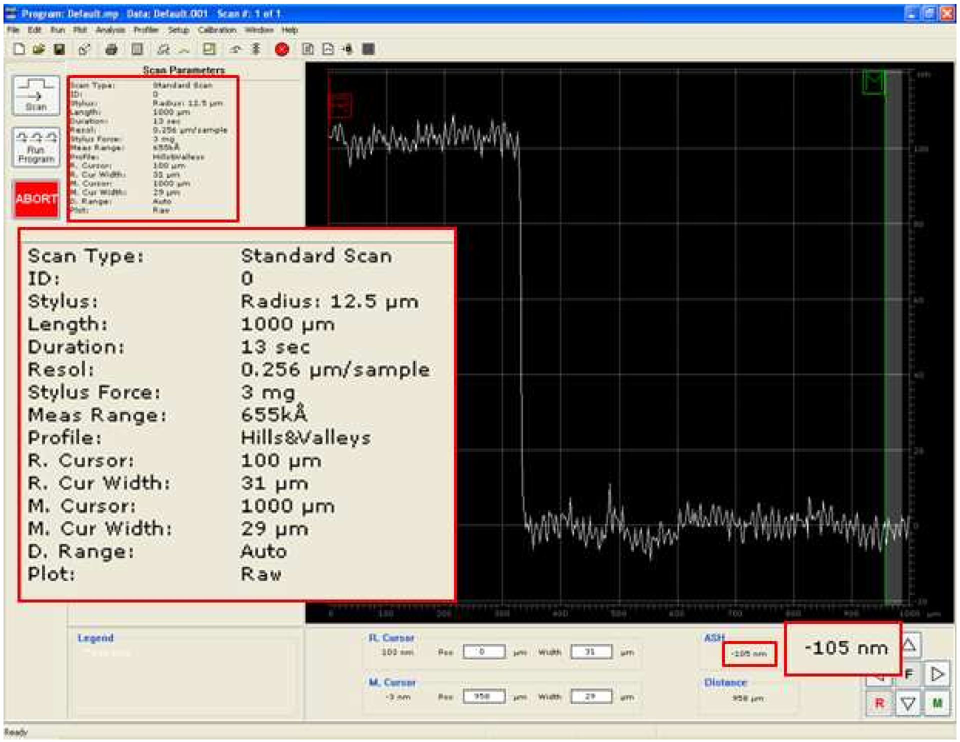

Scan Type: Standard Scan
ID: 0
Stylus: Radius: 12.5 µm
Length: 1000 µm
Duration: 13 sec
Resol: 0.256 µm/sample
Stylus Force: 3 mg
Meas Range: 655kÅ
Profile: Hills&Valleys
R. Cursor: 100 µm
R. Cur Width: 31 µm
M. Cursor: 1000 µm
M. Cur Width: 29 µm
D. Range: Auto
Plot: Raw

R. Cursor 100 nm Pos 0 µm Width 31 µm
M. Cursor -3 nm Pos 958 µm Width 29 µm
ASH -105 nm
Distance 958 µm

-105 nm

Figure 3.3 Thickness measurement of a PdNi thin film by Dektak surface pofilometer. Measurement was taken over the peeling edge of a marker line. Measuring parameters are shown on the left, and the measured thickness of the PdNi film was 105 nm.

`

Results of the Dektak measurement were used to calculate deposition rates for individual target materials. The deposition rate was used to tune composition of precursor alloys for subsequent dealloying. In the study of nanoporous Pd-based films, composition of the precursor alloy was optimized by making strip specimens with a composition gradient. For example, one end of the strip specimen was Pd-rich and the other end was

Ni-rich. Content of Pd or Ni between the two ends was gradually decreased with increasing distance from the Pd- or Ni-rich end, respectively. Similarly, composition of ternary precursor alloys (e.g. AuPdAg) was determined using the same method but three strip specimens were needed to determine composition gradients between each two targets.

After obtaining the optimal composition of PdNi precursor alloys (18-25 at.% Pd and 75-82 at.% Ni), all PdNi films were deposited on the 3-inch Si wafer with substrate biasing at a power of 35 W (RF). A 2 nm Ta interlayer was deposited prior to deposition of PdNi alloy films. Deposition power applied to Pd and Ni targets was 20-30 W (DC) and 350 W (DC), respectively. PdNi films were deposited with a thickness of 25, 45, 90 or 200 nm. Substrate biasing led the PdNi films to have a high compressive stress (up to 1.4 GPa) in the as-deposited films, which can enhance dealloying rates. For deposition of AuPdAg precursor alloy films on the 3-inch Si wafer, the substrate was not biased during the film deposition, yielding lower compressive film stresses (~ 200 MPa). Method of stress measurement will be presented in Section 3.3.1. The optimized composition of AuPdAg alloys were 16 at.% Au, 11 at.% Pd and 73 at.% Ag or 21 at.% Au, 7 at.% Pd and 72 at.% Ag. After film deposition, precursor alloy films were dealloyed in a proper etchant solution (see Section 3.2 for details of dealloying processes).

3.1.2 Deposition of OsRu Films

Substrates for deposition of Os-Ru films were W pellets. These W pellets were prepared by Semicon Associates Inc., using standard powder metallurgical processes to compress W powders (General Electric, US, average particle size: 4.5 μm) into round pellets. The W pellets were 3 mm in diameter and 1.27 mm in height. The as-compressed pellets were sintered at 2200°C for 1 hr to reach a porosity of ~16%. The top surface of each sintered W pellet was CNC-machined into a concave shape and the concave top was the surface for Os-Ru coating.

After cleaning in solvents, the W pellets were arranged and stacked on sample carrier by small pieces of carbon tape for film deposition (see Figure 3.1b). There were two sputtering systems used in this study: an ORION sputtering system at the University of Kentucky and an Omega coater (Omega Industries Inc., MN, US) at Semicon Associates Inc. Base pressure of the Omega coater is 2.7×10^{-4} Pa (2.0×10^{-6} torr). Os-Ru target set in the ORION system was provided by Semicon Associates Inc. with a composition of 60 at.% Os and 40 at.% (measured by EDS).

Semicon Associates Inc. deposited Os-Ru films using the Omega coater at an Ar pressure of 2.7 Pa (2.0×10^{-2} torr) and a deposition rate of 10 nm/min. Os-Ru films deposited by the ORION system (at UK) were performed at an Ar pressure of 3.3×10^{-1} Pa (2.5×10^{-3} torr) and a deposition rate of 16.7 nm/min. The UK films were deposited with applying substrate biasing power of 0, 5, 10 and 20 W (RF), being equivalent to 0, 115, 163 and 239 V (DC), respectively.

In order to measure in-plane stress of Os-Ru films, Os-Ru films were also deposited on Si substrates, including 3-inch wafers and Si strips, 50 mm (L) × 5 mm (W). For improving adhesion of the Os-Ru films to the Si substrate, a 10 nm W interlayer was deposited prior to deposition of the Os-Ru film. As measurements of the film stress using a wafer curvature system (see details in Section 3.3.1), Semicon films had a much lower compressive stress (~20 MPa) than the UK films (5.8-6.5 GPa). Effects of the compressive stress on film structure and texture will be discussed in Chapter 10. After film deposition, some Os-Ru specimens were annealed at $1050°C_B$ (brightness temperature) for 10 min in a mixed N_2-H_2 atmosphere (75% N_2 + 25% H_2). Both as-deposited and annealed Os-Ru films were characterized by XRD, SEM and EDS (see details in Section 3.3) for investigating stability of the film composition, texture and structure during annealing.

3.2 Dealloying

3.2.1 Dealloying of PdNi Precursor Alloys

Before using PdNi as the precursor alloy for producing np-Pd or np-PdNi, PdAg was selected as the precursor and dealloyed in nitric acid. However, PdAg alloys had a low selectivity of dissolution in nitric acid: both Pd and Ag dissolved in concentrated nitric acid and were not able to dissolve in diluted nitric acid. Therefore, PdNi alloy was chosen for dealloying in sulfuric acid. PdNi precursor alloy films were dealloyed in sulfuric acid (25 vol.% or 98 vol.% concentration). For achieving a finer nanoporous structure, some PdNi films were dealloyed in diluted sulfuric acid (25 vol.%) with surfactants, including oleic acid ($C_{17}H_{33}COOH$, 90% purity, Alfa Aesar, USA) and oleylamine ($C_{18}H_{35}NH_2$, 70% pure, Alfa Aesar, USA). The surfactants were added to 100 ml diluted sulfuric acid (25 vol.%) by 2 ml of each. Dealloying time was significantly varied with film thickness and concentration of sulfuric acid. Details of dealloying time will be presented in each chapter.

During dealloying, dealloying progress was tracked by the PdNi alloy peak in XRD scans, and dealloying completion was determined by the time where the PdNi alloy peak completely disappeared. After dealloying completed, specimens dealloyed with no surfactants were rinsed with ethanol (95% purity) for 20-30 sec and soaked in ethanol for 15 hrs to remove residual sulfuric acid. Specimens dealloyed with surfactants were cleaned in boiling ethanol for 30 min, rinsed with ethanol for 20-30 sec, and soaked in ethanol for 15 hrs to remove residual surfactants and sulfuric acid before subsequent characterization.

3.2.2 Dealloying of AuPdAg Precursor Alloys

AuPdAg precursor alloy films (70 nm thick) were dealloyed in diluted nitric acid (35 vol.%) with no surfactants for 35-60 min. Ag can be dissolved in nitric acid rapidly, but Pd also can be significantly removed when dealloyed for a long time. Dealloying progress was tracked by integrated intensities and diffraction angles of the AuPdAg peak in XRD scans. As the tracked result, most Ag atoms were dissolved in the first 30 min, and then a significant loss of Pd occurred in 35-60 min. Dealloying for 60 min can lead almost all Pd to be dissolved. For maintaining some Pd in the final np-AuPd structure, AuPdAg precursor alloy films were dealloyed for 45 min. Dealloyed specimens were rinsed with ethanol for 20-30 sec, and soaked in ethanol for 15 hrs to remove residual nitric acid before characterization.

3.3 Characterization

3.3.1 Wafer Curvature

In-plane stress of thin films deposited on a solid substrate (e.g. Si) can be measured using a wafer curvature system because the stressed film can change curvature of the substrate. Figure 3.4 shows a schematic of substrate curvature changed by the film under a tensile or compressive stress state. As the measured curvature change of the substrate, the film stress (σ_f) can be expressed by the equation:

$$\sigma_f = \frac{E_s}{(1-\nu_s)}\left(\frac{h_s^2}{6Rh_f}\right) \tag{3.1}$$

where E_s is Young's modulus of the substrate, ν is Poisson's ratio of the substrate, h_s is substrate thickness, h_f is film thickness and R is radius of the curved substrate [1]. A typical technique for measuring substrate curvature changes associated with film stresses is to scan the substrate before and after film deposition (or dealloying) by a laser source. Principle of the technique is a laser beam reflected by the film surface (or substrate surface before film deposition) with an angle θ, which corresponds to angles of the curved substrate. When the laser beam moves along a fixed direction, the laser beam is reflected by a different angle. By comparing the change in substrate curvature scanned before and after film deposition (or dealloying), film stress can be calculated by Stoney's equation (eq. 3.1).

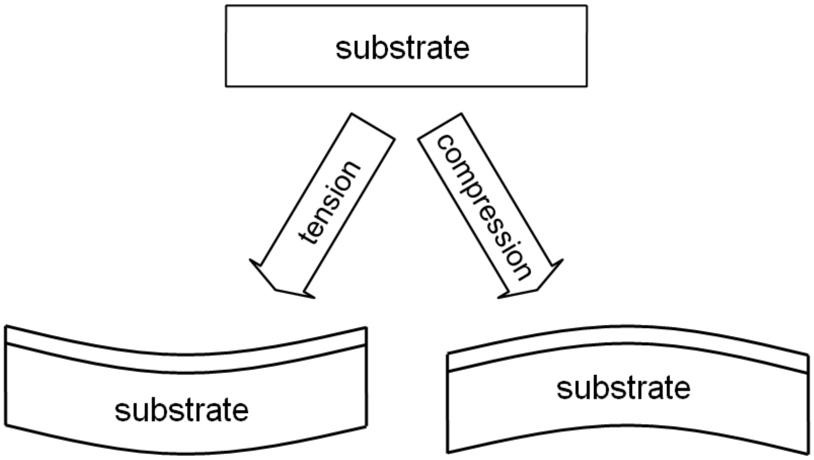

Figure 3.4 Schematic of substrate curvature associated with bi-axial tensile (left) or compressive stress (right).

In this study, film stresses were measured using a wafer curvature system (FLX-2320-S, Toho Technology Co.). The system has two laser sources (wavelength: 670

nm and 785 nm), which can be either automatically switched for obtaining a higher reflectivity or manually fixed to use one of them in some cases. Diametric scans were taken with an interval of 15° to generate a stress map and average film stresses representative of the entire film. Figure 3.5 shows an example of the stress maps for a PdNi precursor alloy film (90 nm thick) before and after dealloying. A significant stress relaxation (~1.4 GPa) during dealloying was obtained by comparing average stresses of the as-deposited and dealloyed films. Stress of the Ta and Pd interlayer (2 nm of each) was subtracted from the total film stress. Average stress obtained from the stress maps was normally used in the study. For np-Pd and np-PdNi specimens that need to be measured for their stress change during hydridation and dehydridation, film stress was measured in an atmosphere-controlled chamber along a certain orientation for the 3-inch specimen, along which reference measurement of the substrate curvature was made before film deposition.

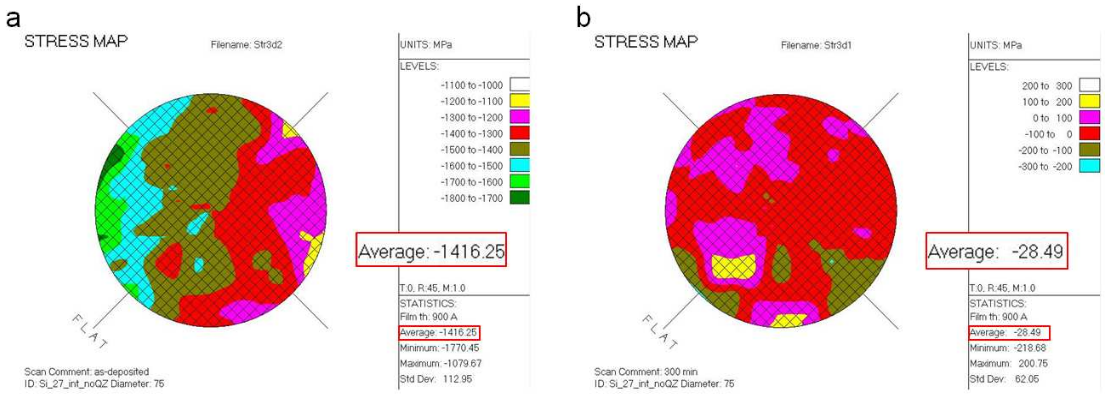

Figure 3.5 Stress maps of (a) as-deposited PdNi precursor alloy (90 nm thick) and (b) dealloyed np-Pd films generated by the wafer curvature system. The stress was 1.4 GPa (in compression) in the as-deposited film and decreased to 28 MPa (in compression) after the film dealloyed for 5 hrs.

3.3.2 XRD

Siemens D500 x-ray diffractometer was used in this study for tracking dealloying progress and determining film texture. XRD scans were performed with scan rates of 0.1-4°/min and a step size of 0.01°. The incident x-ray was Cu K_α line, operated at 40 kV and 30 mA. Wavelength of the x-ray source was 1.541 Å. For the study of nanoporous metal thin films, XRD was performed to track dealloying progress with change in integrated intensity and peak shift of the PdNi (111) peak, appearing at 43.5-43.8° (2θ). Because both Pd and Ni are with a FCC lattice structure, the PdNi alloy film was determined as (111)-textured and compositional change of the PdNi film was able to be tracked during dealloying based on lattice parameters of pure Pd and pure Ni (Pd: 3.8908 Å, Ni: 3.5239 Å [2]). Dealloying completion for PdNi and AuPdAg precursor alloy films was also determined by disappearance of the PdNi/AuPdAg alloy peak. Figure 3.6 shows a typical example of tracking of the PdNi phase during dealloying, which was a 90 nm PdNi film dealloyed in diluted sulfuric acid (25 vol.%) for 0-5 hrs. Additionally, XRD was used to determine texture of as-deposited and annealed Os-Ru films. All XRD scans were calibrated with either Si (400) or W (110) peak.

3.3.3 SEM and EDS

Microstructure of thin film specimens was characterized by plan-view and cross-section. For the microstructural observation, two SEMs were used in this study: Hitachi S900 and S3200. Acceleration voltages of S900 and S3200 were 3 kV and 20 kV, respectively. Both SEMs were operated in secondary electron imaging mode. An EDS system attached to the S3200 SEM was used for characterizing film composition. Specimens were mounted on sample holders (Cu holders for S900 and Al holders for

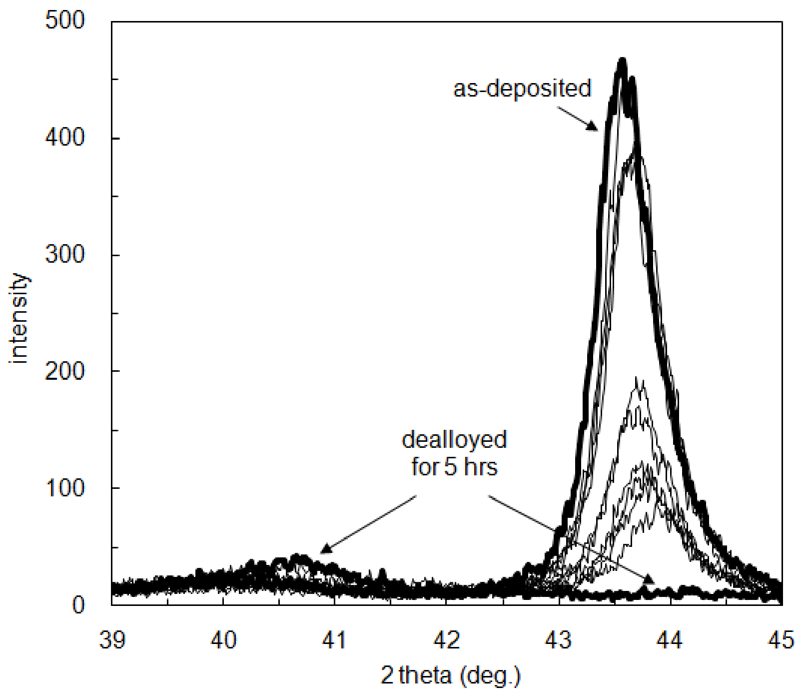

Figure 3.6 Dealloying progress of a 90 nm PdNi precursor alloy film dealloyed in diluted sulfuric acid for 0-5 hrs tracked by XRD. Integrated intensity of the PdNi (111) peak (43.5-43.8°) decreased with increasing of dealloying time. The PdNi peak eventually disappeared and Pd (111) peak showed up at ~40.6° when dealloyed for 5 hrs.

S3200) using colloidal graphite paint. No conductive layers were coated on nanoporous thin films for SEM and EDS characterization, but some Os-Ru specimens were coated by a Au-Pt conductive layer with a thickness of few Å for improving imaging quality (not for EDS measurements). Some specimens were tilted during observation if necessary.

A consistent working distance of 15 mm was applied to all EDS measurements. For all EDS measurements, the strongest peak of each element was selected to calculate compositions, e.g. L-line for Pd, K-line for Ni, M-line for Au, L-line for Os, L-line for Ru, M-line for W and K-line for Si. No selected peaks were overlapped for all specimens.

Composition presented in the study was taken an average from at least 3 measurements for each specimen.

3.3.4 STEM

Microstructure of np-Pd ultrathin film (25 nm, 10 at.% Ni) was also characterized using a scanning transmission electron microscopy (STEM, JEOL 2010F), operating at an accelerating voltage of 200 kV. STEM is an advanced microscopic function affiliated with TEM. During characterization, the specimen was passed through by high energy electrons, which is the principle of TEM operation. But, STEM allows the operation similar to SEM that the election beam scans over the sample in a raster. Detailed features (in nm scale) are able to be imaged with using STEM.

Sample preparation for STEM mainly included several techniques: (1) deposition of PdNi on SiN_x-coated Si, (2) ultrasonic cutting, (3) dimpling, (4) chemical etching and (5) dealloying. After deposition of the PdNi precursor alloy film, the specimen was flipped over and mounted on a glass slide by melted crystal bond. The mounted specimen was ultrasonic cut into discs (3 mm in diameter). As-cut discs were removed from the glass slide by heating and then carefully mounted at the surface center of a cylindrical quartz rod using melted crystal bond (film side still facing toward the rod).

The disc-mounted quartz rod was cautiously centered on the rotating stage of dimpler. Dimpling was done by 3 steps of polishing with colloidal diamond pastes (with sequence of 6, 1 and 0.1 μm diamond particles). Dimpling was stopped when the disc thickness was less than 10 μm. The disc edge was protected by micropaint for avoiding accident corrosion of the PdNi film from the disc edge. Subsequently, the dimpled specimen was chemically etched by HNO_3 : HF : acetic acid (2:1:1, in volume ratio) under observation with a stereo microscopy. The etchant can dissolve remained Si layer (from few to 10 μm) at the thinnest portion of the circular ground area. The etching was immediately stopped by soaking in ultrapure water when a dark pore was observed under the microscopy. The dark pore is the area where the SiN_x layer was exposed.

After etching, the etched disc was removed from the quartz rod by soaking in acetone. Hence, the disc was dealloyed in diluted sulfuric acid with surfactants for 1 hr (see details of dealloying in Section 3.2.1). The dealloyed disc specimen was cleaned in heated ethanol (not boiling) for 30 min and soaked in ethanol for 15 hrs to remove residual surfactants and sulfuric acid. After drying in the air, the disc specimen was ready for STEM characterization.

Chapter 4

Preparation and Hydrogen Sensing Behavior of Np-Pd Thin Films

4.1 Introduction

Interactions between hydrogen and transition metals can lead to reversible formation of metal hydrides, with potential applications in H storage and purification. Pd interacts strongly with H and the two can exist as a solid solution hydride at room temperature, where H atoms occupy octahedral sites in the face-centered cubic (FCC) structure of Pd. For a H/Pd stoichiometric ratio between 0.01 and 0.6, the hydrides exist as immiscible α and β phases that both have FCC structures [1]. In addition, nanostructured Pd is believed to exhibit unique hydrogen absorption and desorption behavior, as well as a narrowing of the miscibility gap. These effects are attributed to highly uncoordinated sites at the edges and corners of ledges on crystal surface planes [2, 3]. In order to enhance its hydrogen absorption capability via size reduction of Pd clusters, Pd has been prepared primarily in two forms, namely nanoparticles [3-5] and thin films [6, 7]. These materials hold promise for application in hydrogen storage and purification, catalysis, and energy engineering. However, dispersed Pd nanoparticles must be stabilized on a substrate in order to be used in applications requiring large amounts of exposed surface area. For example, Ding et al. [8] deposited Pd thin films on nanoporous anodic alumina templates to serve as actuating coatings for hydrogen sensing.

A blanket thin film of Pd deposited on a substrate offers improved mechanical stability, but limited surface area. Using standard thin film deposition techniques, it is difficult to simultaneously achieve both high surface area and good intrinsic mechanical integrity for the application of nanoscale Pd-based materials. In this study, nanoporous Pd (np-Pd) thin films were prepared under different dealloying conditions and were compared with respect to their structure and susceptibility to cracking.

Dealloying, or selective dissolution, is a reliable process for obtaining porous structures from an alloy containing two or more metallic elements. It is used to prepare nanoporous metals, with np-Au being a prime example. Although dealloying to produce np-Au has been reported by several research groups [9-11], and although the mechanisms of dealloying have also been discussed and simulated in some detail [12, 13], Pd has received very little attention, with two groups reporting the fabrication of bulk np-Pd [14, 15], but no studies of thin film np-Pd. However, np-Pd films should be effective for applications such as heterogeneous catalysis and hydrogen sensing.

Similar to the use of AuAg alloys to produce np-Au, PdNi alloys were used as precursors to make np-Pd. Alloys of Pd and Ni are completely miscible at room temperature, which is helpful for obtaining a uniform np-Pd structure after dealloying. Another reason for choosing the Pd-Ni system is high selectivity between Pd and Ni during dissolution in sulfuric acid (Ni dissolves much more quickly). Additionally, there is a large difference in atomic size between Pd and Ni, and thus the lattice parameter varies significantly (~10%) between pure Pd and pure Ni. This size discrepancy allows the tracking of dealloying progress by x-ray diffraction (XRD), which is not possible with the Au-Ag system due to the very similar lattice parameters of Au and Ag. The approach has been used for tracking phase changes in Ni-Cu during dealloying [16]. The current study focused on the preparation of np-Pd thin films by dealloying, including identification of the point at which dealloying was completed, and on the microstructure and hydrogen absorption/desorption behavior of np-Pd films.

4.2 Experiments

PdNi alloy films were magnetron co-sputtered onto Si substrates (CrysTec GmbH, Berlin, Germany) using an Ar plasma in a high vacuum system (base vacuum better than 1×10^{-6} Pa) at room temperature. Substrates were (100)-oriented, 180 µm or 380 µm thick, single crystalline Si wafers coated with 10 nm amorphous silicon oxide and 50 nm amorphous silicon nitride. The amorphous silicon nitride surface was cleaned, prior to film deposition, by substrate biasing at 35 W (RF power) for 1.5 minutes. 10 nm Ta and 10 nm Pd films were sputtered as interlayers to improve adhesion between the final np-Pd film and the substrate. Deposition of PdNi alloy films with different compositions was achieved by varying the sputtering power for the Pd and Ni targets. Substrate biasing (35 W, RF power) was applied during alloy film deposition, resulting in 90 nm and 300 nm films with a strong {111} film texture. Film thickness was subsequently measured by surface profilometry (Veeco Dektak 6M Stylus Profiler) and was found to differ from the expected thickness (based on known deposition rate) by less than 4%.

The as-deposited alloy films were dealloyed in either concentrated (98 vol.% stock solution) or dilute (25 vol.%) sulfuric acid, which can remove Ni atoms from the alloy phase and transform Pd into a nanoporous structure. Initially, concentrated nitric acid was used to dealloy PdNi and PdAg alloy films. However, Ni was not removed efficiently from the PdNi precursor. Additionally, both Pd and Ag were dissolved by nitric acid.

As-dealloyed specimens were rinsed and immersed in ethanol (95%) for at least 1 hr to remove remnant sulfuric acid in the nanoporous structure. For tracking the progress of dealloying, XRD (Siemens model D500) was used to determine the presence of the

PdNi alloy phase in the films. Consistent parameters were used for all specimens: 38°-45° scan range, 0.01° step size, and either 0.1°/min or 4°/min scan speed. The position of the Si (400) peak was measured for every sample, to determine and correct any peak shift in the XRD scans. Microstructure of np-Pd films was observed in plan view with a scanning electron microscope (Hitachi S900) operated at 3 kV in secondary electron mode. Composition of the as-deposited and dealloyed PdNi films was determined by energy dispersive X-ray spectroscopy (EDS, Hitachi S3200 SEM). Stress changes during hydrogen absorption/desorption of np-Pd thin films were measured with a wafer curvature system (FLX-2320-S, Toho Technology Co.) equipped with an atmosphere-controlled chamber. Ambient hydrogen content was adjusted from 0% to 20% (by volume) and then back to 0% by mixing zero-grade hydrogen (99.9% purity) with ultrahigh purity nitrogen (99.999%), with each gas controlled by a separate flow controller. Stress was measured at 20 sec intervals during hydrogen absorption/desorption. During measurements of response time, when hydrogen flow was simply turned on/off and not changed in small steps, stress was measured at 15 sec intervals. All stress measurements were made at room temperature.

4.3 Results and Discussion

Dealloying of PdNi alloys in a sulfuric acid solution involves two mechanisms: (1) dissolution of Ni atoms at interfaces between the alloy and the sulfuric acid, and (2) diffusion of Pd adatoms across the surface of the alloy and/or np-Pd ligaments [13]. The microstructure of np-Pd, e.g. shape, curvature, and size of pores and Pd ligaments, is determined by the competition between Ni removal from the alloy and Pd surface diffusion.

4.3.1 Tracking the Extent of Dealloying

Dealloying of a 300 nm PdNi alloy film in concentrated sulfuric acid (98% stock solution) for 0 to 10 min was tracked by XRD, as illustrated in Figure 4.1. Based on the lattice parameters of pure Pd and Ni, their (111) peaks should appear at 40.1˚ and 44.5˚, respectively. XRD scans for each specimen were calibrated against the Si (400) peak position, which should lie at 69.1˚. In Figure 4.1, a diffraction peak at ~43.6˚ in each scan (except for the scan of the PdNi film dealloyed for 10 min) is attributed to the Ni-rich PdNi precursor alloy. Integrated intensity of the alloy peak decreased as dealloying progressed, until the peak eventually disappeared. Final disappearance of the peak, which occurred abruptly and rapidly, indicated that the PdNi alloy phase could not be detected by XRD, even though remnant Ni was detected by energy dispersive X-ray spectroscopy (EDS). New peaks corresponding to np-Pd were not observed in XRD scans of most dealloyed films, e.g. that shown in Figure 4.1. According to the peak shift relative to the expected peak positions for pure Ni and pure Pd, the Pd concentration of the as-deposited alloy film was ~19 at.%, in agreement with the value of 18 at.% measured by EDS. During dealloying, Pd concentration in the PdNi alloy varied slightly from 19 at.% to 22 at.%, as determined from XRD scans.

Cross-sectional and plan view scanning electron microscope (SEM) images of the 300 nm PdNi films dealloyed with 98% sulfuric acid for 2 and 10 min are shown in Figure 4.2. In Figure 4.2a, cross-sectional micrographs (with the sample tilted by 10˚) of the film dealloyed for 2 min exhibited a multilayered structure: from bottom to top, one can see the Si substrate, ~50 nm amorphous silicon nitride, ~15 nm total thickness of Ta and Pd interlayers, 185 nm porous PdNi layer, and a 45 nm top layer. The top layer above

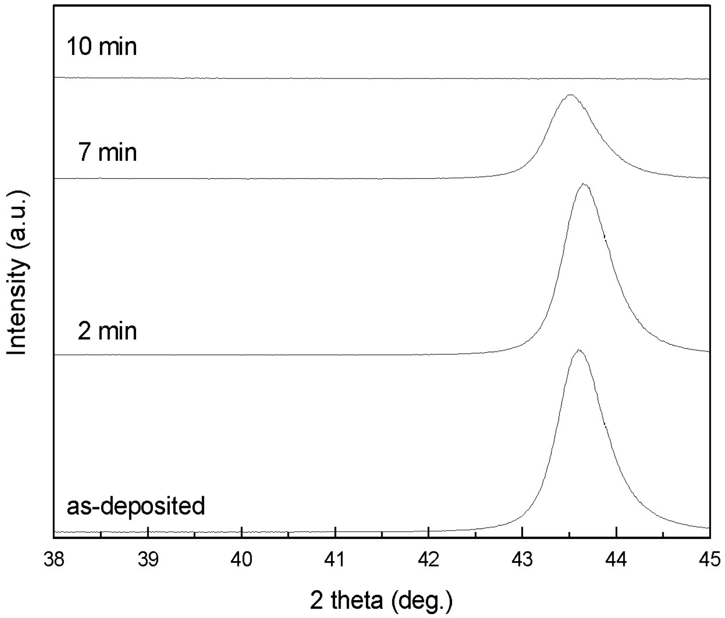

Figure 4.1 Evolution of dealloying in a 300 nm PdNi film immersed in concentrated (98%) sulfuric acid, as tracked by the integrated intensity of the PdNi alloy peak at ~43.6˚ in XRD scans. The alloy peak is still strong after dealloying for 7 min, but disappears completely by 10 min dealloying time.

the porous PdNi film exhibited a uniform thickness ~45 nm. As seen at higher magnification of an area where the top layer was partially peeled away (Figure 4.2b), this top layer sat on a rougher porous PdNi layer. The porous PdNi layer exhibited elongated pores, with dimensions ~20 nm wide and 150 nm long, which were oriented roughly perpendicular to the Si substrate. The inset in Figure 4.2a is a plan view observation of the partially dealloyed PdNi film. In this inset, white clusters ~20 nm in diameter were distributed over most of the surface, except for a number of dark areas, and the cluster/hole size was the same as the grain size in as-deposited precursor films.

Figures 4.2c and d show plan view and cross-sectional SEM images of the microstructure of the PdNi film dealloyed for 10 min (at which point the alloy phase was

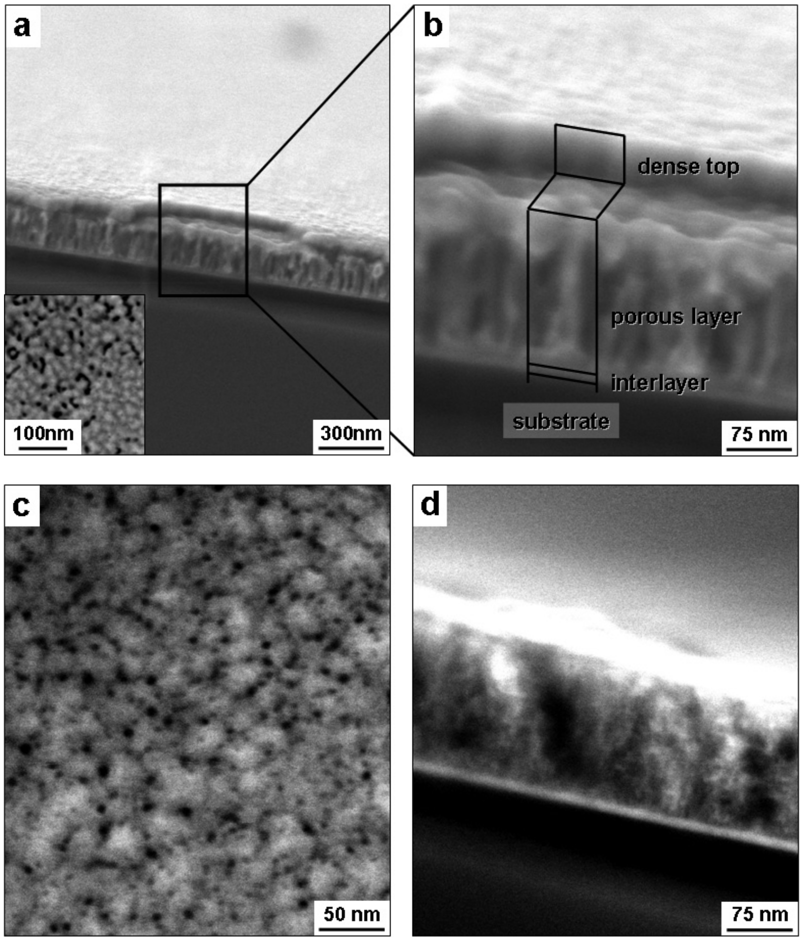

Figure 4.2 **(a)** and **(b)** Cross-sectional SEM micrographs of a 300 nm PdNi film dealloyed by 98% sulfuric acid for 2 min (partial dealloying), which produced a multilayered structure: Si substrate, amorphous silicon nitride coating, Ta and Pd interlayers, np-Pd film, and a dense top layer. A plan view observation is shown in the inset of (a). **(c)** Plan view and **(d)** cross-sectional SEM micrographs of the film dealloyed for 10 min, which resulted in a nanoporous structure with no dense top layer.

no longer detected by XRD). Pd clusters 15-30 nm wide were surrounded by pores ~5 nm in diameter. The cross-sectional image shown in Figure 4.2d reveals a porous structure through the film thickness, but the top layer shown in Figures 4.2a and b has disappeared; moreover, pores are less than 10 nm in diameter, in agreement with plan view observations (Figure 4.2c). The thickness of the dealloyed film decreased by ~45%, from 300 nm to 165 nm. Sun and Balk [17] reported that the thickness of 25Au-75Ag alloy films decreased by ~20% during dealloying to form np-Au, much less than the contraction observed here for np-Pd. The final thickness of np-Pd (165 nm) is believed to result from contraction of the porous PdNi layer shown in Figure 4.2b (185 nm, not including the 45 nm dense top layer). The top layer shown in Figure 4.2b peeled away from the underlying film at longer dealloying times, and this appears to be responsible for the rapid disappearance of the PdNi alloy peak from XRD scans.

Composition of the thin film varied during dealloying and was determined using EDS, as shown in Figure 4.3. Total Pd content increased slightly during the first 2 min of dealloying, from ~15 to ~19 at.%. As dealloying time progressed from 7 min to 10 min, however, Pd concentration increased rapidly from 37 to 78 at.%, after which it exhibited a plateau at ~78 at.%. The slight change in Pd content during the first 2 min of dealloying is consistent with the slight decrease in integrated intensity of the alloy diffraction peak shown in Figure 4.1, i.e. a small portion of precursor PdNi was dealloyed to form np-Pd and thus the total Ni content decreased. This is also consistent with the formation of porosity within the first 2 min of dealloying (see Figures 4.2a-b). During continued dealloying (to 7 min), total Pd content increased significantly (Figure 4.3) and the alloy diffraction peak experienced a concomitant decrease in integrated intensity (Figure 4.1). Starting at 10 min dealloying time, the np-Pd film exhibited a plateau in Pd content, suggesting that the dealloying process had run its course. Given that a post-dealloying Ni content of 22 at.% was detected by EDS, the remnant Ni may reside in the np-Pd ligament structure. As seen in Figure 4.1, the alloy diffraction peak disappeared completely by 10 min dealloying time, and SEM (Figure 4.2d) revealed a fully porous film with no dense top layer. The lack of a np-Pd diffraction peak in Figure 4.1 is typical of this material, for which diffraction peaks are low or non-existent. This may be due to the small diameter of ligaments, which cause extreme peak broadening and may be susceptible to rotation out of the diffracting condition.

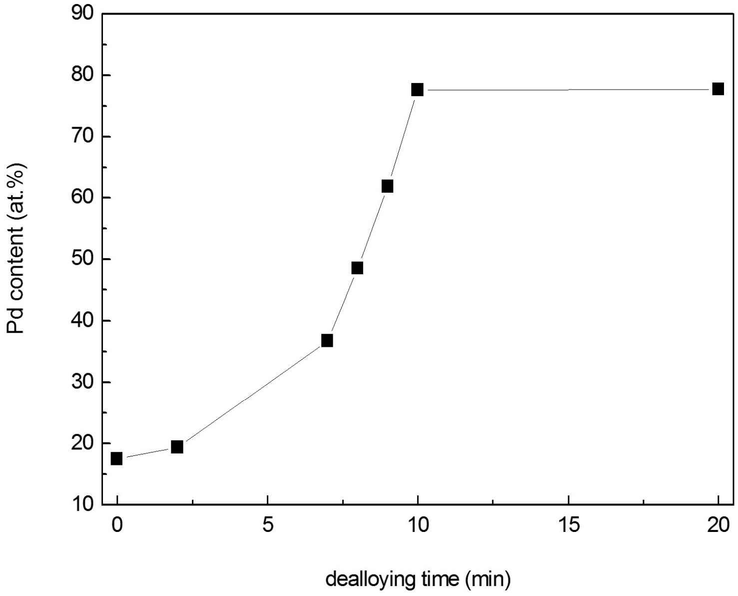

Figure 4.3 Changes in Pd content of PdNi alloy films at dealloying times from 0 to 20 minutes. Pd content increases rapidly between 7 and 10 min dealloying time, and exhibits a plateau at ~78 at.% beyond this point.

4.3.2 Effect of Dealloying Rate on Nanoporous Structure

To investigate the effect of dealloying rate on microstructure of np-Pd, 90 nm PdNi alloy films were dealloyed in concentrated (98% stock solution) and dilute (25%) sulfuric acid, and the PdNi alloy peak was tracked by XRD, as shown in Figure 4.4. Figure 4.4a presents a series of XRD scans of a PdNi alloy film in the as-deposited state, and after dealloying (of the same sample) for 10 sec to 120 sec in concentrated sulfuric acid. Similar to dealloying of the 300 nm PdNi film shown in Figure 4.1, the peak attributed to the precursor alloy at ~43.6° was observed in each scan, except for a dealloying time of 120 sec. Pd concentration in the PdNi alloy, as estimated from the PdNi alloy peak position, was ~19 at.% before dealloying. This peak shifted to higher angles during dealloying, indicating that the interplanar spacing of the {111} diffracting planes decreased. This is consistent with changes in the biaxial film stress measured at various stages of dealloying: stress was initially highly compressive (-1.4 GPa), but relaxed to -28 MPa (compressive) at 120 sec. This net tensile change in film stress would cause the spacing between diffracting planes to decrease. Figure 4.4b shows a series of XRD scans for a second PdNi film, as-deposited and subsequently dealloyed for 5 min to 5 hr in dilute sulfuric acid. The PdNi alloy peak disappeared after 5 hr dealloying time,

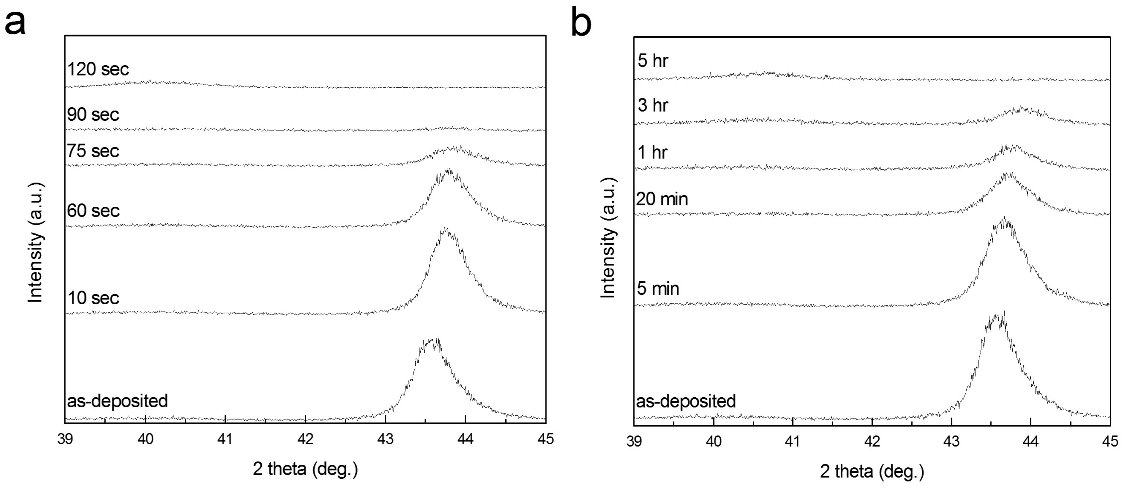

Figure 4.4 Evolution of 90 nm PdNi films dealloyed in **(a)** 98% and **(b)** 25% sulfuric acid, as tracked by the integrated intensity of the PdNi alloy peak at ~43.6° in XRD patterns. During dealloying, the PdNi peak shifted to progressively higher angles, perhaps due to changes in film stress. In XRD scans of both films at long dealloying times, a low, broad peak observed near the expected Pd position of 40.1° is likely due to np-Pd.

indicating that a disproportionately longer dealloying time was required when the sulfuric acid concentration was decreased from 98% to 25%. Dealloying in the dilute acid was at least two orders of magnitude slower than in the concentrated acid.

As shown by the plan view SEM micrographs in Figure 4.5, np-Pd films processed in concentrated versus dilute sulfuric acid exhibited significant microstructural differences. When dealloyed in concentrated sulfuric acid, np-Pd consisted of 10-15 nm wide, particle-like Pd clusters surrounded by pores 5-10 nm in diameter (see Figure 4.5a). However, when processed in dilute sulfuric acid, np-Pd exhibited a sponge-like interconnected structure with elongated Pd ligaments, 10-15 nm long and ~10 nm wide, as shown in Figure 4.5b. However, randomly oriented cracks ~50 nm long and ~20 nm wide were observed throughout the np-Pd film after etching in dilute sulfuric acid. During dealloying, the removal of a majority of atoms tends to cause significant volume contraction [18] and can also shift the film stress toward more tensile values. Cracking

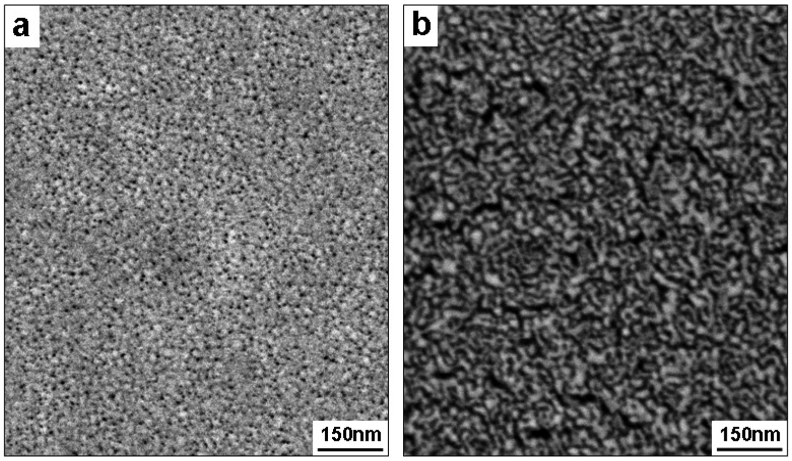

Figure 4.5 Microstructure of np-Pd obtained from 90 nm PdNi films dealloyed in **(a)** concentrated (98%) and **(b)** dilute (25%) sulfuric acid solutions. The films exhibit particle-like and sponge-like structures, respectively, with cluster/ligament size on the order of 10 nm.

tends to relax any film stress that is present, as does the rearrangement of Pd atoms during ligament coarsening. All of these effects would cause the initially compressive stress in PdNi films to relax toward zero, as was observed here.

4.3.3 Effect of Pd Concentration on Nanoporous Structure

Composition of the PdNi precursor alloy was varied to investigate the effect of Pd content on the final structure of np-Pd films. The desired microstructure for these films was a 3-D interconnected network of Pd ligaments and open pores, with no film cracks. The initial Pd content was 18, 22 or 25 at.% for PdNi alloy films with a thickness of 90 nm. All films were dealloyed for 5 hr in dilute (25%) sulfuric acid. In Figure 4.6, the three types of thin film np-Pd exhibited similar porous structures, but with different degrees of cracking. The Pd ligaments seen in Figures 4.6a and b (18 at.% and 22 at.% Pd precursor films, respectively) were ~10 nm wide and 10-20 nm long. In contrast, the ligaments imaged in Figure 4.6c (from the 25 at.% Pd precursor alloy) were much finer, i.e. ~5 nm wide and 10-15 nm long. Additionally, Figure 4.6b shows that the np-Pd film was crack-free, whereas cracks were apparent in Figures 4.6a and c. It appears that film cracking could be mitigated by setting the initial Pd content at 22 at.%. This agrees with earlier studies that found optimum precursor compositions for producing crack-free films. For example, Lu et al. [11] proposed that cracking in np-Au films can be avoided by increasing the Au content in the precursor alloy to an intermediate level. Additionally, Sun et al. observed significant cracking in np-Au films obtained from 25 at.% Au films [17], but they found no cracking when the precursor Au content was increased to 30 at.% [19].

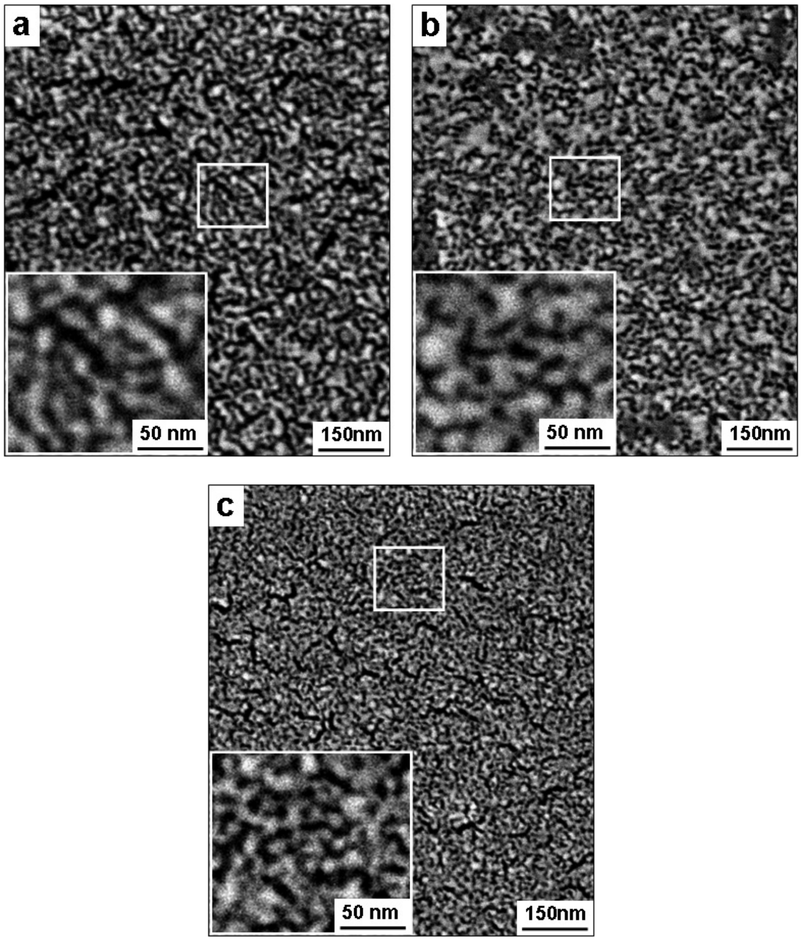

Figure 4.6 Microstructure of np-Pd produced from 90 nm PdNi precursor alloy films with **(a)** 18 at.% Pd, **(b)** 22 at.% Pd, and **(c)** 25 at.% Pd. All films were dealloyed in 25% sulfuric acid and exhibited an open, sponge-like structure with ligaments and pores smaller than 10 nm. Cracks were observed in the films obtained from 18 at.% Pd and 25 at.% Pd precursor films, but not in the 22 at.% Pd film shown in (b).

4.3.4 Hydrogen Absorption/Desorption Behavior of np-Pd Films

In Pd hydrides, H atoms occupy octahedral interstitial sites in the Pd matrix. During hydridation and dehydridation, which cause reversible transformation between pure Pd and hydride phases, the resulting lattice expansion and contraction lead to stress changes in the film that can be used to track hydrogen absorption and desorption. The volume occupied by equivalent unit cells in each lattice is ~11% higher in β-PdH_x (x = ~0.6 at 1 atm) than in pure Pd [20, 21]. In the current study, the stress of np-Pd films exposed to varying amounts of atmospheric hydrogen was measured in order to evaluate hydrogen sensitivity. Np-Pd was produced from 90 nm PdNi precursor films dealloyed in dilute sulfuric acid for 5 hr. Hydrogen content was increased from 0 to 20 vol% in 5 steps and then sequentially decreased to 0 vol% using the opposite sequence. After each step, hydrogen content was held constant for 3 min and stress measurements were taken every 20 sec. The film stress at each step was taken as the average of all measurements at a given hydrogen content, and the stress change (versus the initial stress of -28 MPa, measured without hydrogen present) was calculated. As seen in the plot of hydrogen absorption/desorption behavior in Figure 4.7, film stress became more compressive with increasing hydrogen content, leading to a maximum change of -54 MPa in 20 vol% hydrogen.

As the amount of atmospheric hydrogen was decreased, film stress relaxed toward its original value. However, the stress did not immediately recover when hydrogen was reduced to 0 vol%, but maintained a residual stress change of -20 MPa (compression). After 10 min, the residual compressive stress had relaxed nearly to the original stress (-4 MPa residual change). This lag in stress recovery may be due to trapping of H atoms within the np-Pd ligaments. This trapped H could require a longer time to be completely released, due to capillary densification of gases in the small pores at pressures below the equilibrium vapor pressure [22]. This effect can be understood by considering the much smaller channel diameter (~10 nm pore size, as opposed to a mean free path of 70 nm for hydrogen at 1 atm), which hinders the escape of hydrogen from the nanoporous structure.

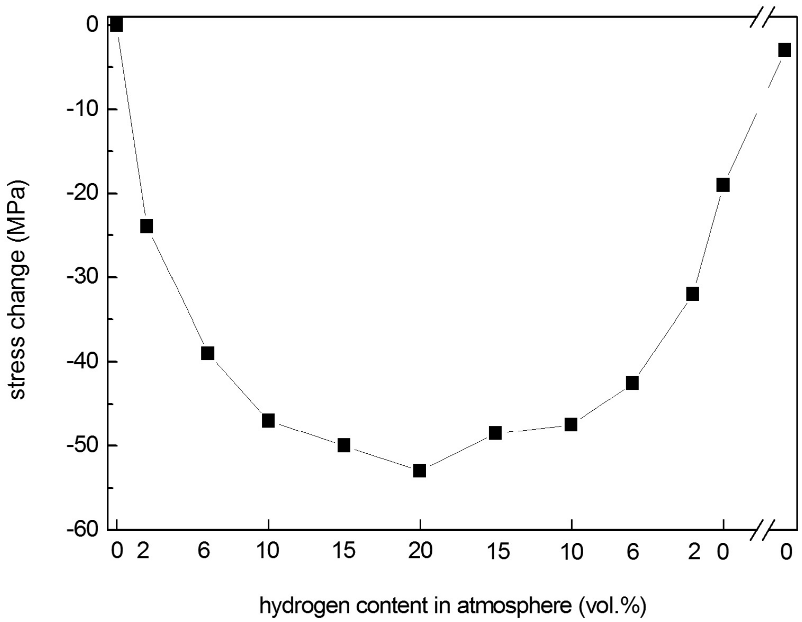

Figure 4.7 Hydrogen absorption/desorption behavior of 90 nm np-Pd film in an atmosphere where hydrogen content increased from 0% to 20% (by volume) and then decreased back to 0%. The np-Pd film stress became increasingly compressive with higher hydrogen content, and remained at a significant level after removal of hydrogen from the atmosphere. After 10 min in flowing nitrogen, stress returned to approximately the same value as that measured for the as-dealloyed film before exposure to hydrogen.

Sensitivity of the np-Pd film to hydrogen was also tested by abruptly switching between hydrogen content of 0 and 10 vol% in the flowing, mixed nitrogen-hydrogen atmosphere. Stress in the 90 nm np-Pd film was measured at 15 sec intervals during the test. Results were compared with a fully dense, 100 nm thick Pd film, shown in Figure 4.8. The initial stress in the dense Pd and np-Pd films were +85 and +6 MPa, respectively. When the hydrogen content was switched to 10 vol%, stress immediately began to shift to a compressive state. The dense Pd film exhibited a gradual change in stress to -287 MPa, with two plateau regions that were separated at a time of ~5 min. In contrast, the np-Pd film stress rapidly changed when the hydrogen content was switched from 0 to 10 vol%, initially settling at -28 MPa within 30 sec and later shifting to a plateau at -41 MPa after ~8 min. When the hydrogen content was switched back to 0 vol%, the np-Pd film displayed a much shorter response time than the dense Pd film, and stress relaxed nearly to the original value. Overall, np-Pd exhibited greater sensitivity to hydrogen than the dense Pd film. This is likely due to the higher amount of surface area and shorter diffusion length in individual Pd ligaments. In the np-Pd film, H atoms are more easily absorbed at the ligament surfaces and can penetrate into the interior regions of ligaments.

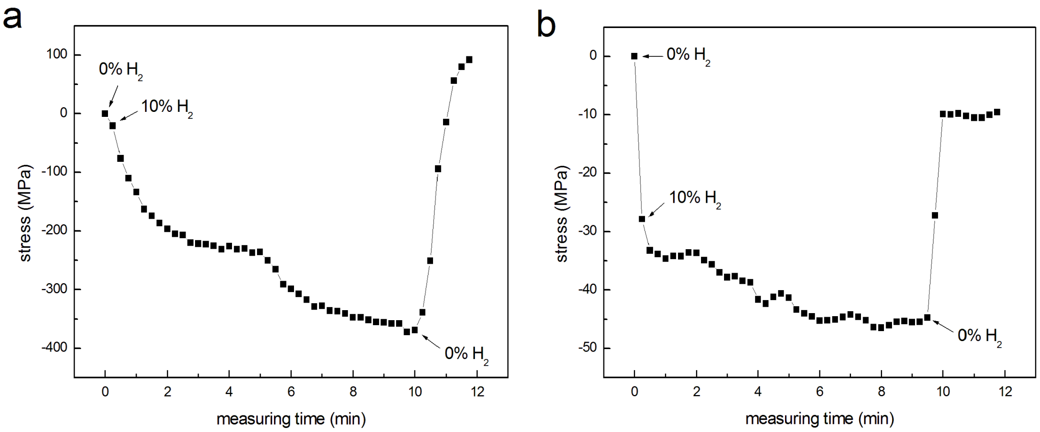

Figure 4.8 Stress changes measured in **(a)** 100 nm dense Pd film and **(b)** 90 nm np-Pd film, in an atmosphere where hydrogen content was rapidly changed from 0% to 10% (by volume). The np-Pd film stress reaches a plateau much more quickly than the dense Pd film (which also exhibits an intermediate plateau). The points at which hydrogen flow was switched on/off are indicated on each plot.

4.4 Summary

Np-Pd films were prepared by dealloying PdNi alloy films in sulfuric acid. Evolution of dealloying in 90 nm and 300 nm PdNi alloy films was monitored with XRD, by tracking the position and integrated intensity of the PdNi alloy peak. PdNi alloy films dealloyed in dilute sulfuric acid yielded np-Pd films with a sponge-like and interconnected ligament structure, with ligaments/pores ~10 nm in size. Film cracking was observed in np-Pd films obtained from precursor alloys with high and low Pd content, but an intermediate composition (22 at.% Pd) resulted in crack-free films. Hydrogen absorption/desorption behavior of np-Pd was evaluated by measuring changes in film stress. The fine pore/ligament structure and high amount of surface area resulted in high sensitivity and rapid response times upon hydrogen exposure, suggesting that np-Pd may be a promising material for hydrogen sensing.

Chapter 5

Achieving Finer Pores and Ligaments in Np-PdNi Thin Films

5.1 Introduction

Nanoporous metals can be produced by dealloying, a chemical or electrochemical process that dissolves one or more metallic components from a precursor alloy. During dealloying, dissolution of the less noble component and surface diffusion of the more noble component occur continuously, alternately dominating the evolution of porous structure. As part of the non-equilibrium dealloying process that takes place at the dissolution front, adatoms of the more noble component can agglomerate on alloy surfaces and eventually form interconnected ligaments with open pores [1, 2]. As dealloying proceeds, the in-plane stress of an alloy film on substrate can change significantly, with an initial shift toward higher/tensile stress followed by a relaxation in stress. This is attributed to Ag dissolution dominating the initial stage of dealloying, transitioning to surface diffusion of Au and ligament coarsening after the less noble metal has been nearly depleted [3]. The final porous structure can be significantly influenced by these two mechanisms and when the transition between them occurs [4]. A concentrated etching solution or longer time for adatom surface diffusion enhances ligament coarsening. However, for applications that require maximum surface area, a coarse ligament structure may be undesirable [5].

Due to the strong interaction between Pd and hydrogen, nanostructured Pd, including nanoparticles [6, 7] and thin films [8, 9], is promising for applications such as hydrogen sensing. Nanoporous-Pd (np-Pd) was first reported by Kabius et al. [10], but no further studies on np-Pd have been published. The nanoporous structure in np-Pd thin films offers a high amount of surface area, and smaller pores and ligaments should be beneficial when surface absorption of hydrogen is the rate-limiting step. Indeed, np-Pd thin films (with some Ni content), with pores and ligaments on the order of 10 nm [11, 12], exhibit rapid changes in stress upon exposure to a hydrogen-containing atmosphere.

Oleic acid and oleylamine are used as dispersion agents for preparing metallic nanoparticles, e.g. Pd- and Pt-based metals [13, 14], because these molecules can attach to the metal surfaces via physisorption due to van der Waals attraction [15, 16], or via chemisorption with covalent bonding [17, 18]. Oleate ions ($C_{17}H_{33}COO^-$) can easily adsorb on the Pd surface, and this micelle structure (metal coated with surfactant molecules) can prevent agglomeration during preparation and storage of nanoparticles. To produce np-PdNi thin films with finer porosity in this study, oleic acid ($C_{17}H_{33}COOH$, 90% purity, Alfa Aesar, USA) and oleylamine ($C_{18}H_{35}NH_2$, 70% pure, Alfa Aesar, USA) were added as surfactants to diluted sulfuric acid (25 vol.%) for dealloying of co-sputtered PdNi alloy (90 nm thick, 18 at.% Pd, 82 at.% Ni). It was hypothesized that surface diffusion of Pd adatoms and ligament coarsening would be hindered by oleate ions attached to Pd surfaces.

5.2 Experiments

PdNi alloy thin films were deposited by magnetron co-sputtering Pd and Ni onto single-crystalline (100)-oriented Si (180 μm thick, coated with 50 nm amorphous Si_xN_y, CrysTec GmbH, Berlin, Germany). The base pressure of the sputtering chamber (ORION system, AJA International Inc., North Scituate, MA, USA) was 1.3×10^{-6} Pa (1.0×10^{-8} torr). 2nm Ta and 2 nm Pd interlayers were sputtered prior to deposition of the 90 nm

PdNi film. Substrate biasing was applied with an RF power supply (35 W) during deposition of the alloy film, resulting in a strong {111} film texture.

Oleic acid and oleylamine were added (2 ml each) to dilute sulfuric acid (25 vol.%, 100 ml) to create a solution for dealloying the as-deposited PdNi films. The extent of dealloying was tracked with x-ray diffraction (XRD, Siemens model D500, operated at 40 kV and 30 mA with a step size of 0.01˚), until the alloy peak disappeared. Ultrasonic agitation was used to enhance the dealloying process for some specimens. All dealloyed films were cleaned in boiling ethanol (95% purity) for 30 min, rinsed with ethanol for 20-30 sec, and soaked in ethanol for 15 hrs to remove residual surfactants and etchant before characterization. Microstructure of np-PdNi films was observed in plan view with a scanning electron microscope (SEM, Hitachi S-900, operated at 3 kV in secondary electron mode). Film composition was analyzed using energy dispersive X-ray spectroscopy (EDS, Hitachi S3200 SEM). In-plane film stress was measured with wafer curvature (FLX-2320-S, Toho Technology Co., Japan).

5.3 Results and Discussion

For all films and etching solutions, the initial PdNi alloy peak disappeared from XRD scans after 5 hrs dealloying time. The disappearance of the precursor alloy peak was taken as an indication that dealloying was complete and the original dense film had been transformed into a nanoporous structure. Figure 5.1 shows the nanoporous structure of np-PdNi films processed with and without surfactants. Both micrographs exhibit interconnected ligaments and pores. Ligaments in the np-PdNi film dealloyed without surfactants (Figure 5.1a) were ~10 nm wide and ~30 nm long. However, ligaments in the np-PdNi film dealloyed with surfactants (Figure 5.1b) were noticeably finer, <5 nm wide and ~10 nm long, and were surrounded by pores with an average diameter of ~5 nm. The addition of surfactants to the etching solution proved to be effective for inhibiting ligament coarsening during dealloying. The adsorption of surfactants on the ligament surfaces should increase the resistance to diffusion of Pd adatoms, limiting the mobility of Pd adatoms. In other words, Pd adatoms were partially immobilized by the surfactant-enhanced etchant, which limited the surface diffusion and agglomeration of Pd to a smaller, more localized region of the dissolution front.

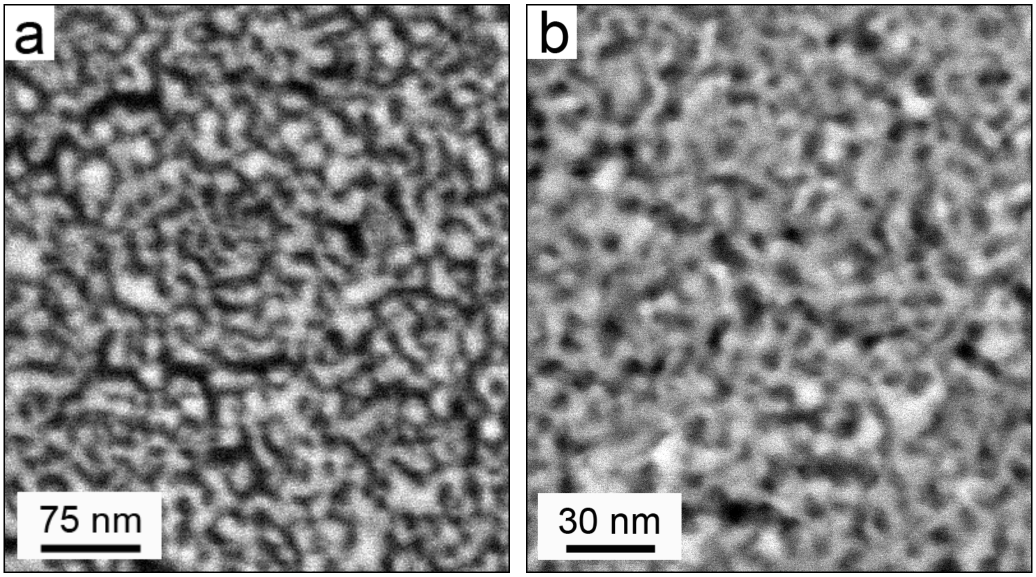

Figure 5.1 Microstructure of np-PdNi films processed in dilute sulfuric acid (a) without and (b) with surfactants. Both micrographs show interconnected ligament structures, but the np-PdNi film dealloyed with surfactants exhibits significantly finer nanoporosity.

Changes in film composition during surfactant-enhanced dealloying were determined using EDS measurement of Pd and Ni content. The stress in a separate thin film specimen was measured at the same dealloying time intervals. Plots of film composition and stress are shown in Figure 5.2. As dealloying proceeded, Pd content (data points indicated by open circles, with values on the y-axis at the left) increased from 18 at.% to 54 at.%. Two plateaus were observed in the plot of Pd content, between dealloying times of 1-5 min and 10-20 min, as seen in the inset of Figure 5.2. Within these time intervals, Pd content was nearly constant at ~31 at.% and ~38 at.%, respectively. The final remnant Ni content measured in the np-PdNi films was substantial (46 at.% at the end of dealloying), although XRD scans did not detect a PdNi alloy peak in samples dealloyed for 5 hrs. Longer dealloying times (>12 hrs) resulted in no additional Ni loss. The amount of retained Ni was much higher than in np-PdNi films dealloyed without surfactants, where the final composition was 77 at.% Pd and 23 at.%

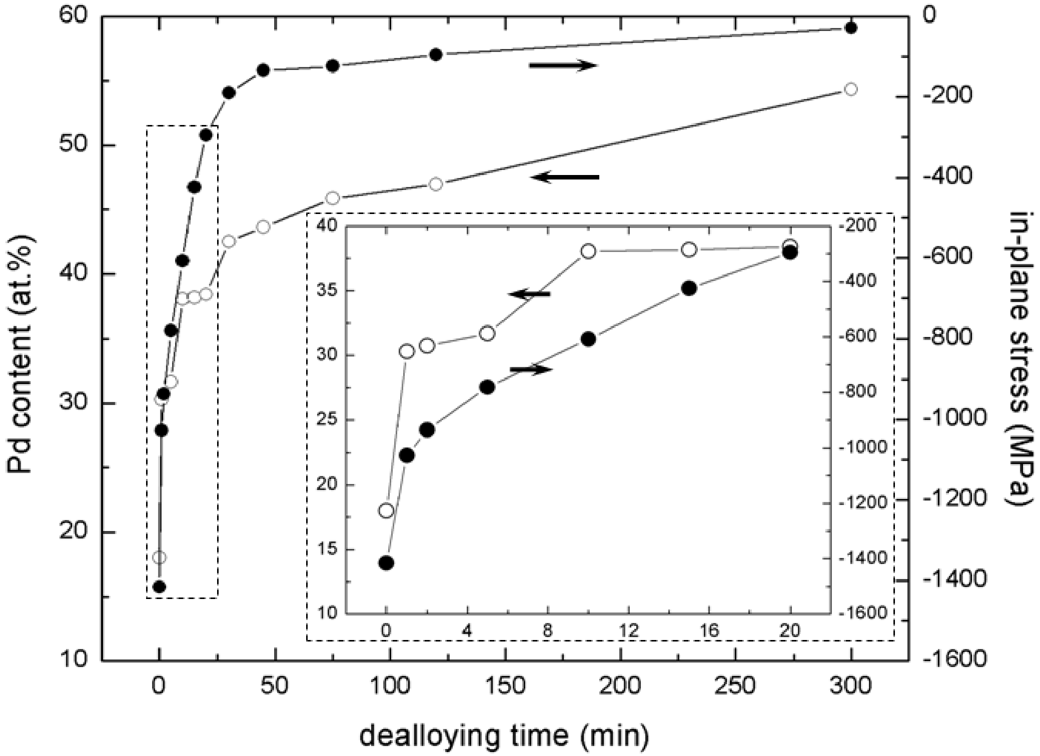

Figure 5.2 Changes in Pd content and film stress during dealloying with surfactants. Pd content (open circles, values on y-axis at left) increased from 18 at.% to 54 at.%, and film stress (black circles, right y-axis) relaxed from -1420 MPa to -28 MPa (in compression).

Ni, after dealloying times of 5 hrs and 12 hrs. This may be due to surfactant molecules attached to Pd surface atoms, since the tethered surfactant covers a portion of the ligament surface and could prevent acid from reacting with a number of Ni surface atoms that would otherwise be etched from the ligaments.

The dissolution of Ni involves removal of a large portion of the original precursor alloy volume, which shifts the film stress toward a more tensile (or less compressive) state. This is due to the high amount of volume contraction that typically occurs during dealloying [19], and the constraint on film contraction imposed by the solid Si substrate. Surface diffusion of Pd along np-PdNi ligaments would relax any film stress. Stress in the as-deposited PdNi film was highly compressive (-1420 MPa), due to substrate bias applied during film deposition. During dealloying, this compressive stress decreased rapidly due to dissolution of Ni and surface diffusion of Pd, and the dealloyed film was nearly stress-free (-28 MPa).

In order to shorten the time required for producing np-PdNi, ultrasonic agitation was used to enhance dealloying. Figure 5.3a shows the morphology of an as-deposited PdNi film, with average grain size ~20 nm. Figures 5.3b-d reveal changes in film microstructure after dealloying with surfactants and ultrasonic agitation for 15 min, 30 min and 60 min, respectively (dealloying was considered complete at 60 min, as determined by XRD scans and disappearance of the precursor alloy peak). After 15 min dealloying (Figure 5.3b), the PdNi film exhibited numerous pores ~5-10 nm in diameter, as well as brighter areas that appeared to be undissolved clusters of original PdNi alloy. Longer dealloying times led to a decrease in the number of alloy clusters (compare Figures 5.3c-d with 3b). In Figure 5.3d, the np-PdNi film dealloyed with surfactants and ultrasonic agitation for 1 hr exhibited interconnected ligaments and pores, both with

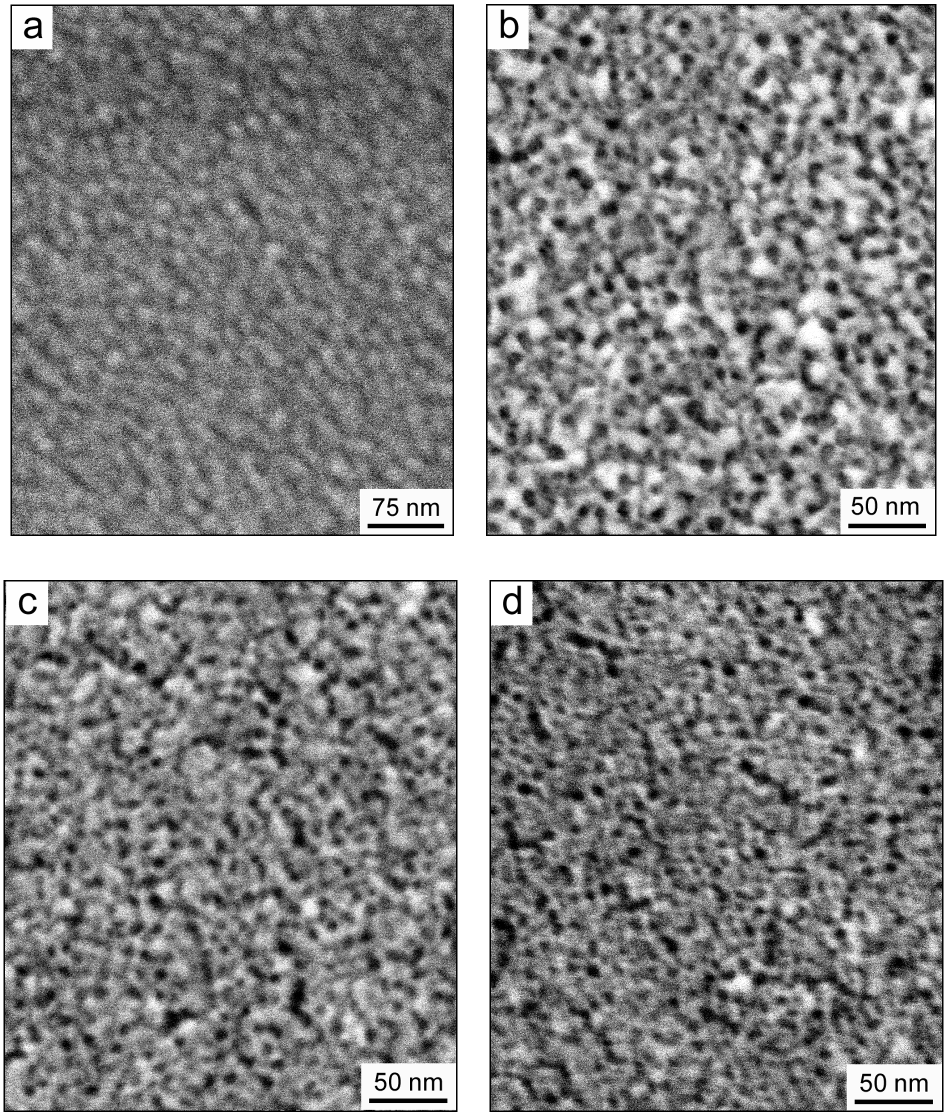

Figure 5.3 Microstructure of PdNi films dealloyed with surfactants and ultrasonic agitation for (a) 0 min (as-deposited), (b) 15 min, (c) 30 min and (d) 60 min. Grain size of the as-deposited PdNi film was ~20 nm. Nanoporosity was uniform and as small as 5 nm in size (for np-PdNi films dealloyed for 30-60 min).

dimensions ~5 nm. Comparing Figures 5.1b and 3d, no significant differences were observed in these nanoporous structures, including interconnectivity of ligaments and size of ligaments/pores. Thus, ultrasonic agitation was helpful in accelerating the dealloying process but did not alter the final nanoporous structure of np-PdNi films.

The improved processing route described here results in np-PdNi films that exhibit an improved response time when exposed to a hydrogen-containing atmosphere. Preliminary studies reported in [11, 12] showed that np-PdNi with coarser ligaments and pores (~10 nm) reached a hydrogen-induced stress plateau within 1 min, as compared to 5-10 min for a dense Pd film. The np-PdNi with fine porosity, discussed in the current paper, exhibited an even faster response time, reaching a plateau within 15 sec. A more detailed investigation of this behavior is underway.

5.4 Summary

In summary, the average ligament width and pore diameter in dealloyed np-PdNi films were decreased by ~50% after adding surfactants to the etching solution. It is proposed that the refinement of nanoporosity is due to partial immobilization of Pd adatoms, which hinders surface diffusion along ligaments. Changes in film composition and stress indicated that dissolution of Ni and relaxation of film stress proceeded rapidly in the initial stage of dealloying. In addition, ultrasonic agitation was found to accelerate the dealloying process while maintaining fine nanoporosity. These np-PdNi films with smaller pores may be well suited for applications that require higher amounts of surface area, such as hydrogen sensing.

Chapter 6

Effects of Substrate Curvature on Dealloying of Nanoporous Thin Films

6.1 Introduction

Dealloying is a straightforward process for producing a nanoporous material by selectively dissolving one or more metallic components from a precursor alloy. Typically, the less noble component is etched from the alloy with a strong oxidizing acid, and the remaining, more noble atoms undergo surface diffusion and agglomeration to form an interconnected network of ligaments with open porosity [1]. The typical length scale for pores and ligaments in nanoporous metals is 2-10 nm. A range of nanoporous metals has been investigated in bulk form, as thin films, or as nanostructured materials, including nanoporous gold (np-Au) [2-4], palladium (np-Pd) [5, 6], copper (np-Cu) [7], and nickel (np-Ni) [8]. In addition, gold-palladium (AuPd) alloys have been investigated as materials for bio-coating [9], hydrogen sensing [10-13] and catalysis [14, 15]. Such applications require high surface area for improved performance, and thus nanoporous AuPd thin films would offer excellent chemical and structural properties for these areas.

Two primary mechanisms, namely surface dissolution and surface diffusion, operate during the dealloying process and can significantly affect the final nanoporous structure. Several aspects of nanoporosity formation and its relation to processing parameters have been investigated. For example, temperature of the dealloying etchant affects the pore/ligament size of np-Au [16]. Crack-free thin films of np-Au on Si substrates can be achieved using a two-step dealloying method [17]. In addition, electrolyte concentration and film stress may play a significant role in determining dealloying rate and final nanoporous structure. There are many potential factors that can influence both surface dissolution of the less noble alloying element and surface diffusion of the more noble element, thereby shifting the dealloying stages dominated by each mechanism. The results presented here suggest that substrate curvature is also a critical factor for dealloying rate and the nanoporous structure that evolves. This aspect has not been investigated before, but is important to the fabrication of nanoporous metal films on irregular and non-planar substrates, which may be important for application of these novel materials.

6.2 Experiments

In this study, thin films of a gold-palladium-silver (AuPdAg) alloy were deposited on flat single-crystalline (100)-oriented Si (380 μm thick, CrysTec GmbH, Berlin, Germany) as well as on curved Kapton sheet (50 μm thick polyimide, DuPont Kapton, type 200 HN) by co-sputtering Au, Pd, and Ag. Film deposition was performed by magnetron sputtering (ORION system, AJA International Inc., North Scituate, MA, USA). The base pressure of the sputtering system was 1.3×10^{-6} Pa (1.0×10^{-8} torr). Both substrates were coated with a 10 nm tantalum (Ta) interlayer prior to deposition of the 70 nm AuPdAg alloy film, to improve adhesion to the substrate. As-deposited films were dealloyed via free corrosion (no applied potential) in diluted nitric acid (35 vol.%) for 45 minutes at room temperature, then rinsed several times and soaked in ethanol (95% purity) for 15 hours before characterization.

Composition of the as-deposited AuPdAg alloy film was 20.3 at.% Au, 7.0 at.% Pd and 72.3 at.% Ag, as measured by energy dispersive x-ray spectroscopy (EDS) in a scanning electron microscope (SEM, Hitachi S3200). This composition was consistently measured at all film locations on both flat and curved substrates. Texture of the as-deposited film was determined by x-ray diffraction (XRD, Siemens D500) and consisted only of a strong (111) component. Microstructure of the alloy and np-AuPd films was characterized with a Hitachi S900 SEM, operated at 3 kV in secondary electron mode. Initial attempts at dealloying of the flat AuPdAg alloy film resulted in non-ideal compositions: after 30 min dealloying time, too much Ag (> 35 at.%) remained in the film, while after 60 min dealloying time, nearly all Pd had been removed (< 1 at.% final Pd content). In order to minimize the remnant Ag and maximize the Pd content in the nanoporous film, a dealloying time of 45 min was used in this study. Final composition of the film on curved substrate was dependent on local curvature.

6.3 Results and Discussion

Figure 6.1 shows the morphology of the as-deposited AuPdAg film and the dealloyed np-AuPd film on a flat Si substrate. Grains in the as-deposited film ranged in size from 15 to 25 nm. After dealloying, the flat film exhibited fine pores and ligaments with an average diameter of 15 nm, close to the size of grains in the as-deposited film (compare Figure 6.1a and inset of Figure 6.1b). A number of cracks, 10-25 nm wide and ~100 nm long, were observed throughout the np-AuPd film. Lu et al. reported that 30 at.% of the more noble constituent (Au in their case) is needed to prevent crack formation in nanoporous thin films on flat substrates [18]. Sun et al. also reported an optimal composition of the precursor alloy (30 at.% Au and 70 at.% Ag) for producing crack-free np-Au films on Si [17]. Thus, cracking of the np-AuPd film in the current study may result from too little Au/Pd (27.3 at.% total) in the precursor alloy. Furthermore, although Pd is more noble than Ag, it dissolves slowly in nitric acid, leading to significant Pd loss at long dealloying times. After 45 min dealloying time, composition of the np-AuPd film on flat Si substrate was 87.6 at.% Au, 4.2 at.% Pd and 8.2 at.% Ag. By comparing the relative amounts of Au and Pd before and after dealloying, and assuming that no Au is lost during dealloying, it is calculated that 77% of the initial Pd content was lost during dealloying. This significant Pd loss reinforces the idea that crack formation in the dealloyed film is due to a low noble metal content, as the amount of Au plus remnant Pd accounts for only 22 at.% of the initial film composition.

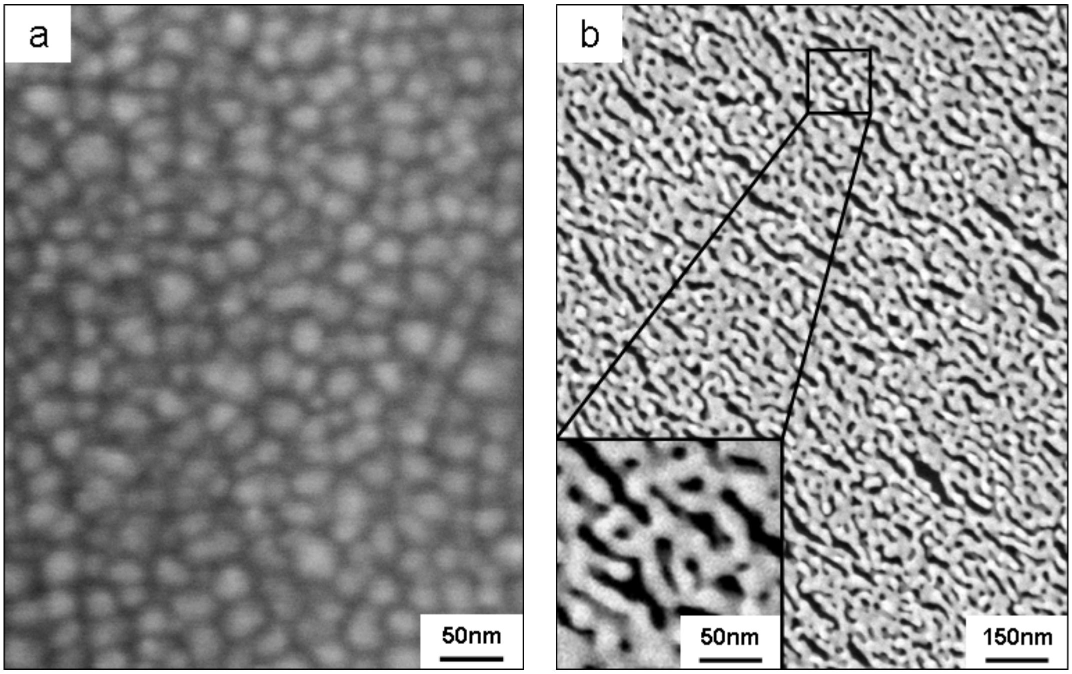

Figure 6.1 Morphology of (a) the as-deposited AuPdAg alloy film and (b) the dealloyed np-AuPd film on Si substrate. Grain size in the as-deposited film was 15-25 nm. The np-AuPd film exhibited ligaments and pores with an average size of 15 nm. A number of cracks, 10-25 nm in width and ~100 nm in length, appeared in the dealloyed np-AuPd film.

For the np-AuPd film on curved Kapton substrate, the distribution and geometry of cracks as well as the final nanoporous structure varied considerably as a function of local substrate curvature. During film deposition and dealloying, the Kapton substrate was held in a curved shape by a polymer template (high-density polyethylene, HDPE). The top surface of the HDPE template was corrugated, with periodic ridges that were 2 mm high and round at the top. Radius of curvature at the top of each ridge was 0.5 mm, and center-to-center distance between neighboring ridges was 3 mm, i.e. the gap between ridges was 2 mm. The Kapton substrate was placed between two templates with this shape, and these templates were then squeezed together to induce periodic curvature in the Kapton. The substrate remained clamped in this manner for 20 minutes, after which one template was removed to expose the Kapton for film deposition. The substrate retained the periodic, corrugated shape. Both the HDPE template and Kapton sheet were resistant to corrosion in the nitric acid solution, allowing the corrugated Kapton sheet to remain fixed on the bottom template, with no change in curvature during deposition, dealloying and subsequent rinsing/cleaning. For SEM and EDS characterization, the np-AuPd film on corrugated Kapton was carefully removed from the template, cut into small pieces (2 mm × 4 mm), and then affixed to a flat sample holder using colloidal graphite paint at one corner. Care was taken to prevent the Kapton from flexing during the cutting and mounting process. It appears that no significant flexing occurred, as the np-AuPd film did not exhibit a deformed ligament morphology. Moreover, the cracking patterns at various locations of the film are the opposite of what would be expected if the Kapton substrate had flexed and caused cracks in the film (see discussion below).

Cracking at different locations in the curved np-AuPd film is shown in Figure 6.2. The distance between the valley (point A) and the ridge (point E) was approximately 4 mm. Note that this is the distance along the substrate surface, not the half-width of the periodic distance between template ridges. SEM micrographs were taken at intervals of 1 mm between adjacent points A-E. The substrate curvature at points A (concave) to E (convex) varied between 1.48, 1.23, 0, -0.91 and -1.51 mm^{-1}, respectively. These values were measured from a cross-sectional image of the corrugated Kapton sample (shown in the image at the center/bottom of Figure 6.2). Each micrograph in Figure 6.2 consists of two images taken at the same location, but at high versus low magnification (on the left and right, respectively). Low-magnification images of the np-AuPd film in the concave

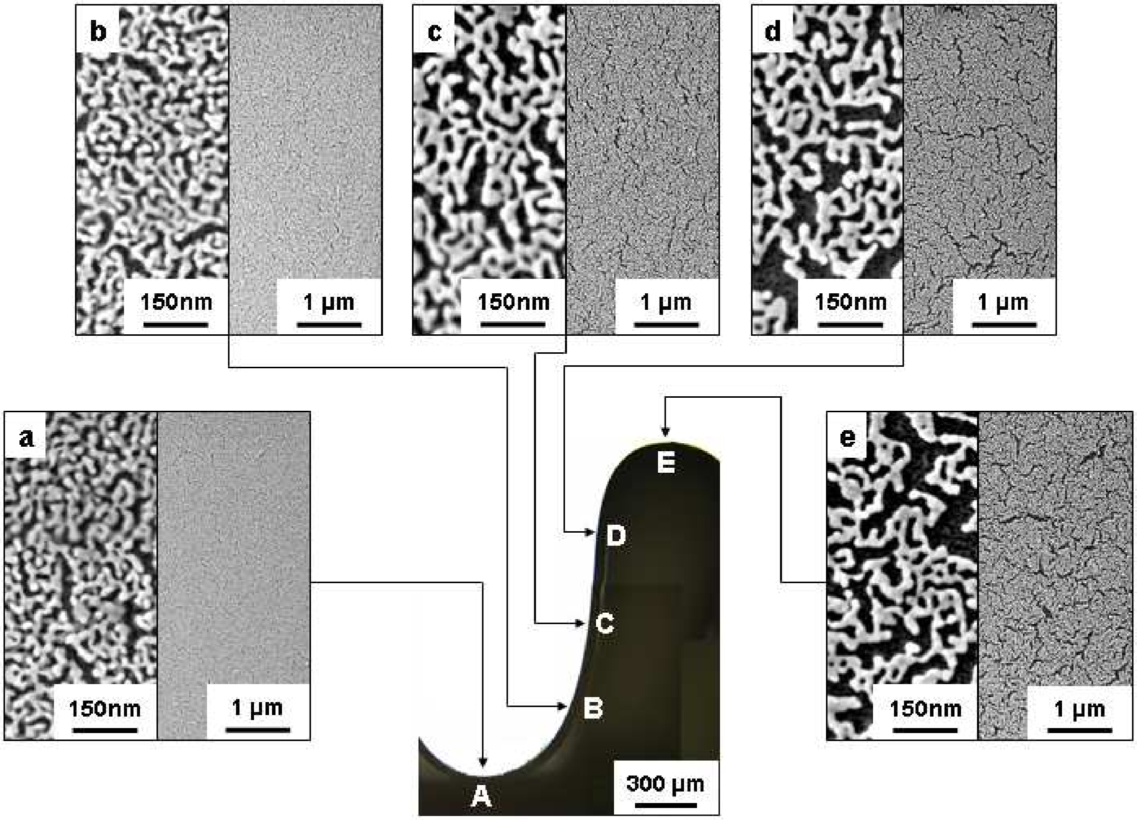

Figure 6.2 SEM micrographs at regular intervals along the surface of the curved np-AuPd film sample, from (a) concave region in a valley to (e) convex region on a ridge. Curvature values at points A-E were 1.48, 1.23, 0, -0.91 and -1.51 mm^{-1}, respectively. The areal density and size of cracks increased from the valley (point A) to the ridge (point E).

region (points A and B) revealed few cracks, while the flat and convex regions (points C-E) exhibited significant cracking. Additionally, beginning at point C, crack width increased as the substrate transitioned from flat to convex and cracks were apparent even at low magnification. The high-magnification images reveal detailed features of the nanoporous structure and cracks. In the concave region (points A and B), the ligaments and pores were 10-15 nm in size, with crack widths on the same order or slightly larger than this. Conversely, in the convex region (points C-E), cracks were wider and more open.

The latter crack morphology is similar to prior observations of cracking in thin film np-Au on flat Si substrates [19], where the lower Au content (25 at.% in the precursor alloy) caused significant film cracking. Note, however, that the amount of Au/Pd appearing in the dealloyed np-AuPd films (in the current study) was only 22 at.% of the precursor film composition. Thus, the film presented in Figure 6.2 would be expected to exhibit a greater degree of cracking at all locations. However, this cracking was suppressed in the concave regions of the film (location A and, to a lesser extent, location B), compared to the flat film in Figure 6.1. Additionally, the ligaments surrounding the cracks in Figure 6.2 did not appear to have undergone deformation, but instead were in an as-dealloyed state, which speaks against the possibility that substrate flexure during cutting and mounting led to the film cracking observed here.

The nanoporous structure at locations C-E was noticeably different from that in the concave region (A-B). In addition to more extensive and wider film cracking, the ligaments at points C-E were wider, longer and more crooked. The crooked shape of these ligaments may be due to their length and higher aspect ratio. These differences in crack and ligament geometry caused the nanoporous structure in the convex region to have a lower density than in the concave region. In fact, the film in the convex region (locations C-E) appears to consist of a single layer of ligaments, whereas the denser film areas in the concave region (A-B) exhibit multiple ligament layers (one can observe underlying ligaments below open pores, seen through the top of the film). This is consistent with a separate study on films with a similar Au-Pd-Ag composition, where after dealloying, a precursor film with uniform thickness exhibited multiple layers of ligaments on a flat substrate but only a single ligament layer on a hemispherical bump in the substrate [20].

Composition of the dealloyed, curved np-AuPd film at locations A-E is shown in Figure 6.3. Ag content decreased from 23.9 at.% at the valley (point A) to 3.7 at.% at the ridge (point E). As the Ag content decreased, Au content increased from 69.6 at.% (at A) to 96.3 at.% (at E), but at the same time Pd content decreased from 6.5 at.% (at A) to 0 at.% (at E). The total content of Au and Pd increased from 76.1 at.% at the valley to 96.3 at.% at the ridge. The dissolution rate for Ag was significantly higher in the convex region of the film (ridge, point E), as evidenced by the higher amount of remnant Ag in the concave region of the film (valley, point A) and by more extensive film cracking in the convex region. Additionally, the ratio of Au (or Au+Pd) to remnant Ag in the dealloyed film was calculated at each location A-E. When plotted as a function of the substrate curvature (calculated from Figure 6.2), the elemental ratio exhibits a linear dependence on curvature between points A-D, i.e. over a curvature range of -0.91 to 1.48 mm^{-1}. The degree of dealloying was proportional to the decrease in curvature toward more negative (convex) values. For point E, the elemental ratio increased significantly, suggesting that beyond some critical negative curvature (-1.0 to -1.5 mm^{-1}), the dissolution of Ag and Pd was enhanced even more strongly by changes in curvature.

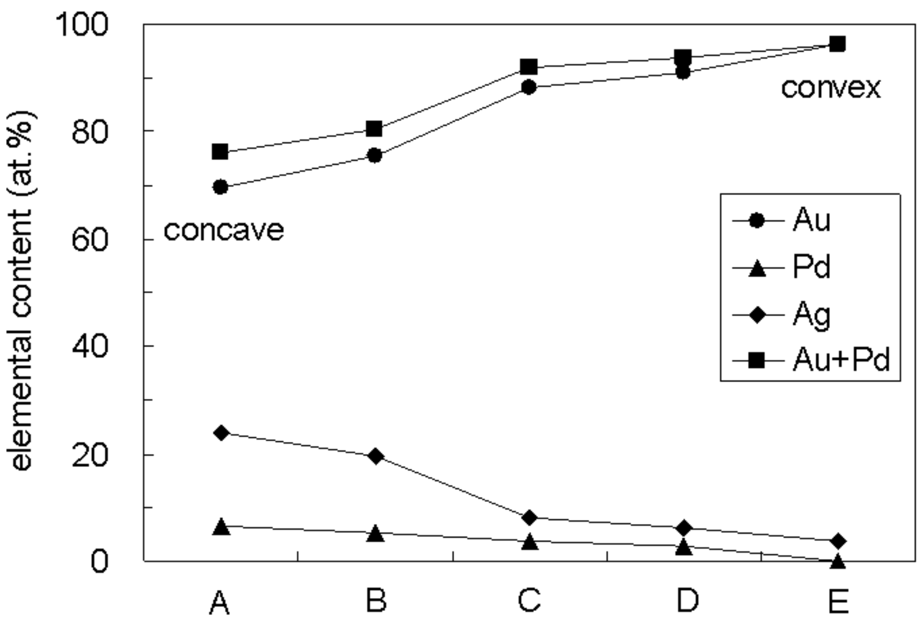

Figure 6.3 Composition at intervals along the surface of the curved np-AuPd film, measured from the valley (A) to the ridge (E). Points A-E are the same as those mapped in Figure 6.2. Remnant Ag content decreased from 24 at.% in the valley to 4 at.% on the ridge. Pd also decreased from point A to point E, and was undetectable at the ridge.

As discussed earlier, dealloying is dominated in turn by dissolution of the sacrificial element (e.g. Ag in this case) or by surface diffusion (e.g. Au and Pd). Dissolution at the dealloying front dominates in the initial stage of dealloying, when Ag is lost rapidly and pores are etched in the alloy. As Ag content decreases and pore formation nears completion in a given region of the sample, the newly formed ligament surfaces offer a pathway for surface diffusion of Au and Pd to take over as the dominant process. In the stage dominated by surface diffusion, Ag content remains low and ligaments coarsen due to the flux of Au and Pd. This model of dealloying was described by Erlebacher [21, 22]. Additionally, Schofield et al. [23] verified this transition in dominant mechanism by tracking changes in remnant Ag content as well as lattice parameter of AuAg foils during dealloying.

For nanoporous structures formed by dealloying for a given amount of time, ligaments should be coarser if the transition from Ag dissolution to Au/Pd surface diffusion occurs more quickly. An earlier transition time would occur if the dissolution rate were higher. In the current study on np-AuPd, the film in the convex region (point E) experienced relatively rapid dissolution of Ag from the surface and thus underwent a longer period of surface diffusion than did the film in the concave region. The rapid rate of Ag removal in the convex region led to a higher areal density of cracks, which were also wider than those in the concave region. This difference in dissolution rates and transition times between dominant mechanisms may be due to different stress levels in the film. It is suggested that the convex film may have a higher tensile biaxial stress (or a lower compressive stress) than the concave film. A stress state that is more tensile should enhance dissolution of the sacrificial element and increase the likelihood that film cracking will occur. Additionally, dissolution should proceed more rapidly at high energy surfaces such as grain boundaries, and grain boundary dissolution may proceed more easily when the film experiences a higher tensile (or lower compressive) stress.

6.4 Summary

In summary, characterization of np-AuPd on flat and curved substrates revealed differences in the dealloyed films. For the Kapton substrate with curvature that varied periodically between concave and convex, the np-AuPd film exhibited a transition in ligament geometry, cracking and film composition. The concave region contained relatively few cracks, shorter and thinner ligaments, and higher amount of remnant Ag. Conversely, the convex region exhibited numerous and wide cracks, thicker and higher aspect ratio ligaments, relatively low residual Ag, and no detectable Pd. The observed differences in dealloyed structure and composition may be due to a more tensile stress state in the convex region, which led to a faster Ag dissolution rate and earlier transition to ligament coarsening.

CHAPTER 7

Transition from Single- to Multi-layered Structures in Np-AuPd Ultrathin Films

7.1 Introduction

Dealloying, or selective dissolution, is a common process for dissolving one or more metal components from an alloy. By using a proper dealloying electrolyte with a high selectivity of corrosion between alloying constituents, less noble elements can be easily dissolved from the alloy. Meanwhile, more noble elements undergo surface diffusion to form a 3-D nanoporous structure with interconnected ligaments that range in size from several nm to tens of nm. Dealloying is a reliable process for producing a variety of nanoporous metals in bulk form, as thin films, or even as nanowires, with nanoporous gold (np-Au) [1-4], palladium (np-Pd) [5, 6], copper (np-Cu) [7] and nickel (np-Ni) [8] as examples.

To understand and model the mechanism(s) of formation of nanoporous structures during dealloying, this process has been investigated by both atomistic simulation and microstructural observation [9-11]. According to this model, dealloying (either by free corrosion or electrochemical dealloying) involves surface dissolution of the less noble constituent(s) and surface diffusion of the more noble constituent(s). Surface dissolution and surface diffusion proceed simultaneously, but these two mechanisms alternately dominate at different stages of dealloying. In general, surface dissolution of the less noble constituent proceeds relatively faster in the initial stage of dealloying, due to a high amount of the sacrificial metal component in the precursor alloy. In contrast, surface diffusion of the more noble constituent along existing ligaments and formation of new surface area at the dissolution front dominate the microstructural evolution during the subsequent stage, accompanied by an increase in surface area due to new porosity formation. Ligaments are formed due to aggregation of the more noble constituent on sample surfaces, with the aggregation driven by spinodal decomposition at solid-electrolyte interfaces.

Np-Au is typically created by dealloying gold-silver (Au-Ag) precursor alloys, using Ag as the sacrificial alloying component because of its ideal miscibility with Au and high selectivity of dissolution (compared to Au). Given the proper precursor alloy composition and dealloying conditions, np-Au can be produced as a supported thin film with no cracks [12] or in bulk form with no volume contraction [13]. These np-Au structures exhibit ligaments and pores with dimensions of 10-15 nm; that is, the cell size (sum of ligament width and pore diameter) is ~25 nm. In order for a nanoporous film to have structural stability, the film thickness should be greater than the cell size. Otherwise, a 3-D porous network cannot exist after dealloying because the structure must contain at least one layer of Au ligaments and one layer of pores. Once the nanoporous film is thinner than (or close to) the critical thickness, i.e. the cell size, an unstable situation may arise for the nanoporous structure, e.g. leading to additional ligament coarsening via surface diffusion and aggregation. This coarsening may result in thicker, single-layered ligaments [12]. The creation of single layers of ligaments should result from the interplay of several factors, including surface diffusion rates on various crystal planes, surface and interface energies of the ligaments and substrate, and wetting behavior between the ligaments and substrate surface. The simultaneous interaction of these factors during dealloying is complicated, but as discussed below, the contact morphology of single-layered Au ligaments on the substrate surface appears to be significantly different from the connected structure of Au ligaments in a multi-layered porous network. Understanding these differences in contact morphology and the transition between single- and multi-layered nanoporous structures will help clarify important details related to the formation of nanoporous thin films. The motivation for choosing np-AuPd stems from potential applications in bio-coatings [14], hydrogen sensing [15-18] and catalytic coatings [19, 20].

7.2 Experiments

AuPdAg alloy films with a thickness of 70 nm were deposited onto a 380 μm thick, single-crystalline (100)-oriented Si substrate (CrysTec GmbH, Berlin, Germany) using a magnetron sputtering system (ORION system, AJA International Inc., North Scituate, MA, USA). The base pressure of the sputtering system was 1.3×10^{-6} Pa (1.0×10^{-8} torr), and the Si substrates had previously been coated with 10 nm amorphous silicon oxide (a-SiO_x) and 50 nm amorphous silicon nitride (a-SiN_x) layers. A 10 nm tantalum (Ta) layer was deposited on the Si substrate prior to deposition of the AuPdAg alloy film, to improve adhesion of the AuPdAg film.

In order multi-layered structures, a AuPdAg alloy film was deposited through a Cu grid onto the Si substrate, which patterned the film into a periodic array of squares. The Cu grid was 20 μm ± 3 μm in thickness, with individual grid squares having round corners and an edge length of 90 μm (see the as-deposited, patterned AuPdAg film in Figure 7.1a). The precursor film was dealloyed via free corrosion (no applied potential) in diluted nitric acid (35 vol.%) for 45 minutes at room temperature. Nominal thickness of the dealloyed film was ~35 nm, resulting in only two layers of AuPd ligaments at the center of the coated surface. The edge regions of grid squares were used to investigate the transition from single-layered to multi-layered porous structure in the np-AuPd film. Dealloyed samples were rinsed with ethanol (95 % purity) and soaked in fresh ethanol for ~12 hrs prior to characterization. Film microstructure was characterized using a scanning electron microscope (Hitachi S-900, operated at 3 kV in secondary electron mode) and a FEI Strata 235 Dual Beam FIB system (operated at 5 kV in secondary electron mode). Composition of as-deposited and dealloyed films was analyzed with energy dispersive x-ray spectroscopy on a Hitachi S-3200 SEM. Film texture was determined using a Siemens D500 x-ray diffractometer operated at 30 kV and 40 mA, with Cu Kα x-rays.

7.3 Results and Discussion

In this study, co-sputtered AuPdAg precursor alloy films (16 at.% Au, 11 at.% Pd and 73 at.% Ag, as measured by energy dispersive x-ray spectroscopy) were used to produce np-AuPd thin films. After dealloying, the composition of the np-AuPd film was 79 at.% Au, 16 at.% Pd and 5 at.% Ag. The dealloying process transformed the curved sides and edge regions of the np-AuPd grid squares into sloped/stepped edges (see Figures 7.1b-c), due to in-plane film contraction during dealloying of 0 to ~20% (the film contracted more at its surface than at the interface to the substrate). The resultant edge region allowed investigation of the transition from single-layered AuPd clusters to a multi-layered np-AuPd film with a 3-D porous network.

During dealloying, film thickness decreased from 70 nm (as-deposited) to ~35 nm (dealloyed), as measured at the centers of grid squares. This represents a thickness contraction of 50%. It is noted that 70% of Pd atoms were lost during dealloying, and the np-AuPd film exhibits a Au:Pd atomic ratio of ~5:1, with some remnant Ag in the

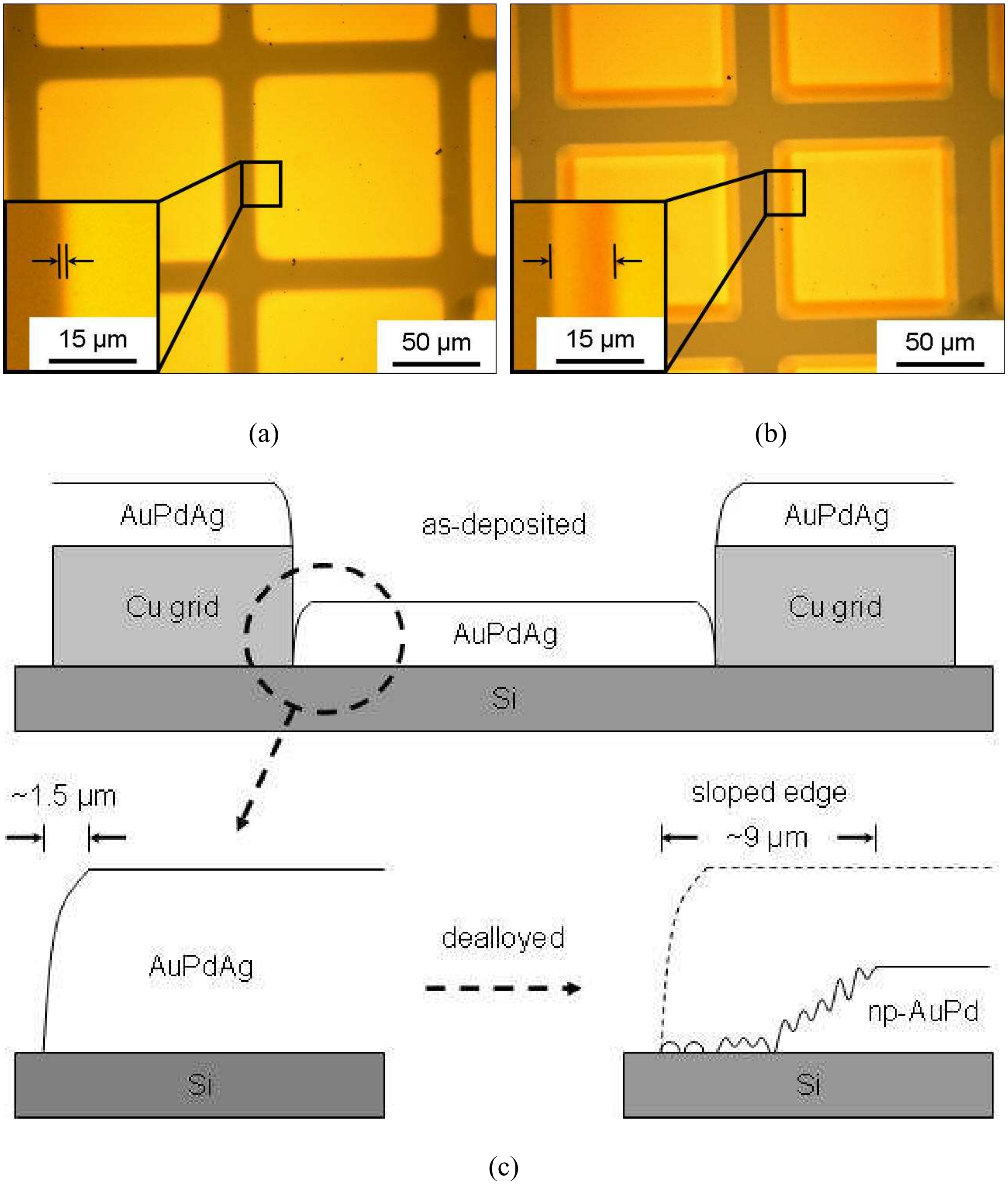

Figure 7.1 Optical micrographs of (a) as-deposited AuPdAg and (b) dealloyed np-AuPd films patterned in a square array. During dealloying, the edge regions of np-AuPd grid squares contracted inhomogeneously, yielding a sloped and stepped transition region; this is seen in the inset of (b), and shown schematically in (c).

film. X-ray diffraction indicated a significant shift of the AuPdAg alloy peak (initially at $2\theta = 38.66^\circ$) toward the expected position of the Au/Ag peak (Au and Ag have essentially the same lattice parameter of 4.08 Å, corresponding to a diffraction angle of $2\theta = 38.26^\circ$ for Cu-K_α radiation) during the dealloying time range between 45 min and 60 min, i.e. most Pd loss from the ternary alloy phase occurred during this time frame.

When observing dealloyed AuPd morphology at regular intervals along the sloped/stepped edges of patterned squares, it is seen that the AuPd clusters exhibit an interesting transition from nanodots (in the thinnest region) to a 3-D nanoporous multilayer structure (in thicker regions), as shown in Figure 7.2. The micrographs in Figures 7.2a-l were taken along a line perpendicular to a grid edge, at intervals of 800 nm between successive micrographs, using a scanning electron microscope (SEM, Hitachi S-900, operated at 3 kV in secondary electron mode). At the thinnest edge, AuPd clusters appeared in plan-view as circular dots with a size of 5-15 nm. Most nanodots were distributed uniformly with spacing on the order of 10 nm. As seen in Figure 7.2a, spacing was larger between AuPd nanodots with larger diameter. Thus it appears that the AuPd nanodots accumulated Au and Pd atoms from their surrounding regions and depleted these regions of Au/Pd, as would be expected during particle coarsening. As film thickness increased to the point where the precursor alloy film first exhibited constant thickness (~1.5 μm from the edge) and as shown in Figures 7.2b-c, neighboring AuPd nanodots connected and created elongated clusters. In Figure 7.2d, the AuPd clusters were more interconnected and formed a 2-D network with few “hanging ligaments”. With increasing film thickness, the AuPd clusters grew longer and coarser (see Figures 7.2c-g) until a second layer of AuPd ligaments began to form. This second layer of ligaments can be seen in Figure 7.2h (marked by dashed ovals), which represents the onset of a 3-D

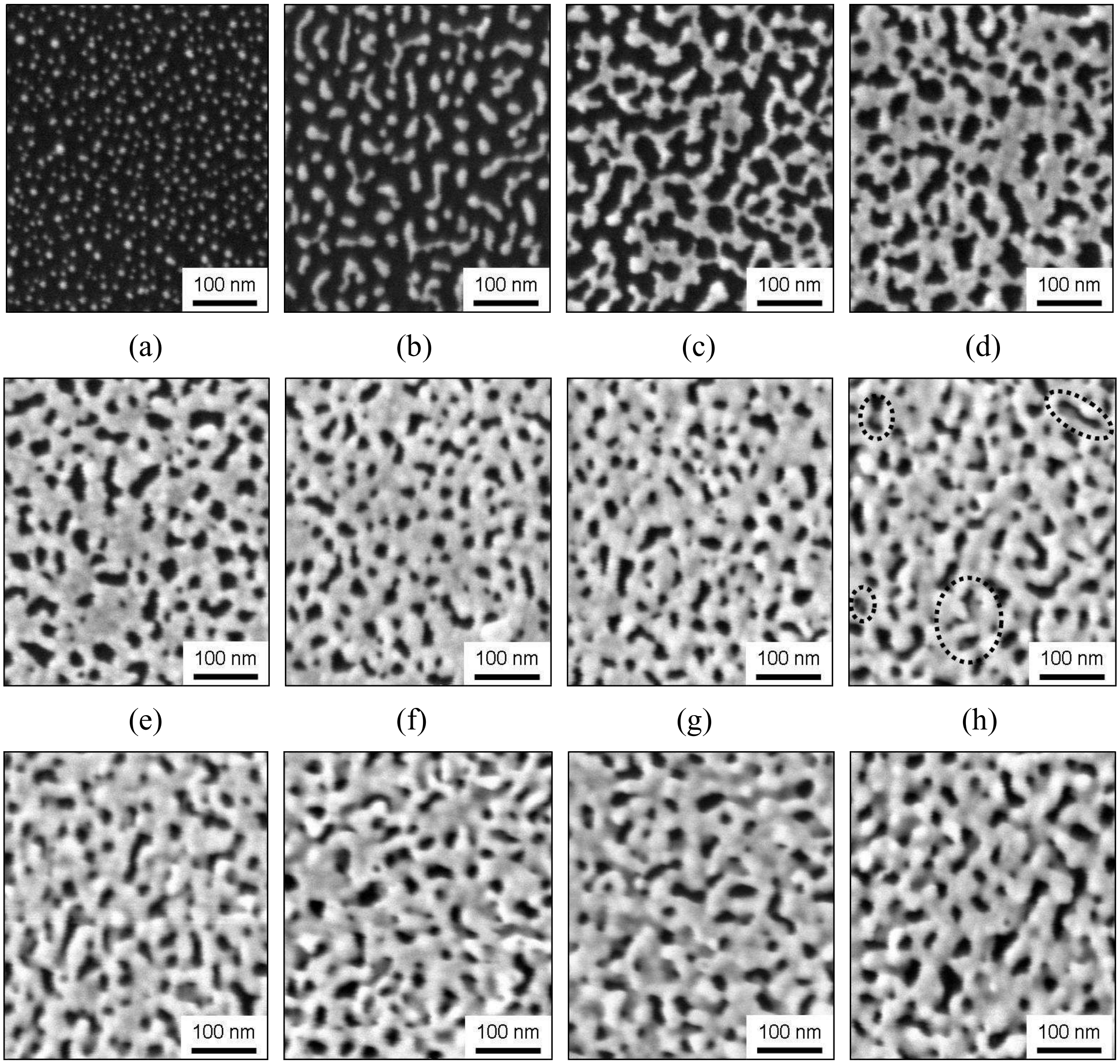

(a) (b) (c) (d)

(e) (f) (g) (h)

(i) (j) (k) (l)

Figure 7.2 Morphological change in AuPd clusters (or ligaments) observed along an edge of the patterned, dealloyed np-AuPd film, as imaged from the thinnest film edge to the terrace edge with an interval of ~800 nm between micrographs. AuPd clusters transitioned from dispersed nanodots, shown in (a), to a 3-D nanoporous structure with interconnected AuPd ligaments at the terrace edge, shown in (l). A second layer of AuPd ligaments was first observed in (h), as indicated by dashed ovals.

multilayer network. Observing the microstructures shown in Figures 7.2h-l, an increasing number of AuPd ligaments in the bottom layer can be seen through the open porosity of the film surface.

Interestingly, the AuPd ligaments and pores in the top layer (see Figures 7.2f-l) were rather uniform in size, despite significant changes in film thickness along the sloped/stepped edge, even with the creation of a second layer of ligaments. Additionally, many pores in the top AuPd layer (e.g. Figures 7.2j-l) were open down to the Si substrate, with no AuPd ligaments in the bottom layer appearing beneath these pores. Thus the ligament structure observed here does not appear to be completely random in 3-D; instead, the bottom layer of ligaments seems to have a preferred orientation. The details of how the top AuPd layer can be supported above the substrate by the bottom AuPd layer is a critical and interesting question, and must be clarified to understand the transition from single- to multi-layered structures. This will be discussed below.

As film thickness increased along the sloped/stepped edges of grid squares, the structure of AuPd clusters transitioned from isolated AuPd nanodots to an interconnected 2-D network. This can be seen by comparing the micrographs in Figures 7.2b-c. Additionally, the electron micrograph in Figure 7.3 (obtained with a FEI Strata 235 Dual Beam FIB system, operated at 5 kV in secondary electron mode) reveals a rather abrupt, albeit meandering transition between nanodots (dark region on the left) and the ligament network (bright region on the right). This difference in interconnectivity of AuPd clusters can be seen clearly in the inset of Figure 7.3. An isolated AuPd cluster near the interface, but surrounded by the continuous ligament network (and marked by an arrow), appears darker, suggesting that image brightness is closely related to interconnectivity of the AuPd clusters.

Based on SEM images of the tilted sample at a location where the grid square was scratched away, thus allowing a nearly cross-sectional view of the thin film, it appears that the continuous ligament network (bright region in Figure 7.3) has a higher surface level than the nanodot region on the left. This would explain the abrupt change in brightness under SEM imaging as the film transitions from isolated nanodots to a continuous ligament network. This line is located near the edge region of the original precursor grid squares, where the film changed from constant thickness to a rounded edge as shown in Figure 7.2c. In the outermost <1.5 μm of the precursor alloy edge region, the amount of Au/Pd atoms was insufficient to produce a continuous ligament network. The abruptness of the transition line is likely due to a high slope of the alloy surface and rapid change in Au/Pd available for forming nanodots or ligaments. Even the fully thick precursor alloy film yielded only 1-2 ligament layers after dealloying. The AuPd nanodots and ligaments on either side of the transition interface were ~15 nm wide. Although the size of individual clusters does not change significantly at this interface, there does appear to be a critical amount of Au/Pd atoms needed to yield an interconnected, single-layered np-AuPd network.

Once the amount of Au/Pd atoms exceeds the critical value needed to form a continuous single layer of np-AuPd, a second layer of AuPd ligaments can begin to form. With the appearance of this second layer, additional questions arise: How does the 2-D ligament pattern transition to a 3-D nanoporous network with interconnected porosity? In the 3-D porous structure, is the contact behavior of AuPd ligaments near the substrate different from those near the film surface?

In order to address these questions, np-AuPd films were produced on a convex substrate that, after dealloying, exhibited open cracks and revealed the through-thickness ligament structure. Figure 7.4a shows a film produced on a convex substrate (a semi-spherical droplet of Crystalbond coated by a 10 nm Ta interlayer). Near the center

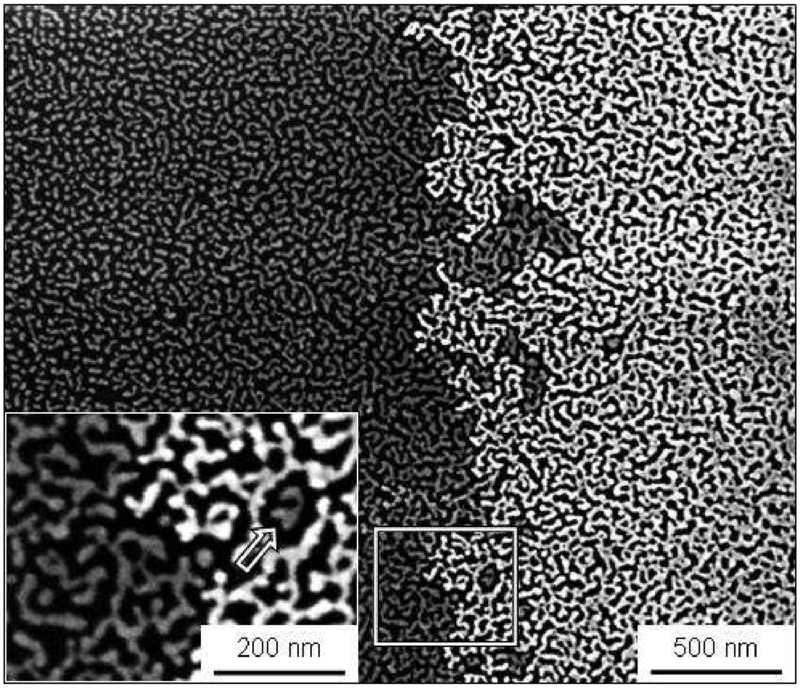

Figure 7.3 This SEM micrograph reveals an abrupt transition between isolated AuPd nanodots and clusters (darker region on the left) and an interconnected, 2-D np-AuPd ligament network (brighter region on the right). Inset shows an isolated AuPd cluster (marked by an arrow) that is darker than the surrounding, continuous ligament network. The difference in brightness is due to differing height of the AuPd top surfaces in each region.

of this image (also see inset), AuPd ligaments can be seen in a nearly cross-sectional view. Most ligaments in the first layer (closest to the substrate) were perpendicular to the substrate and appeared to terminate without spreading along the substrate surface. This is different from the morphology of single-layered AuPd clusters, shown in Figures 7.2b-g and 3. The 3-D np-AuPd structure in Figure 7.4a consists of a ligament network supported from below by numerous individual “nanolegs”. Figure 7.4b presents additional observations of the np-AuPd structure that reinforce this interpretation. Here, a freestanding np-AuPd film with 10 nm Ta bottom layer was released by dissolving the

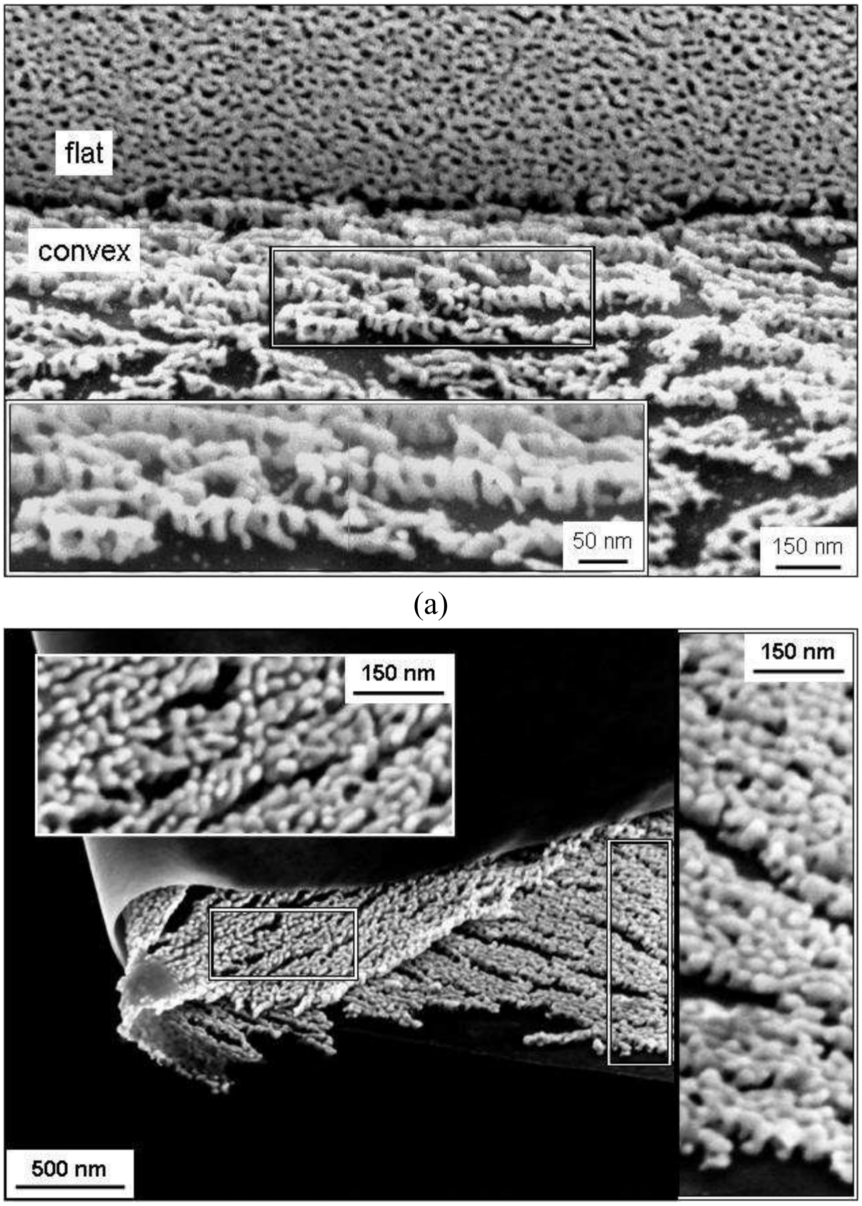

(a)

(b)

Figure 7.4 (a) Np-AuPd films on a convex substrate exhibited open cracks and a high number of ligaments oriented perpendicular to the substrate. (b) This np-AuPd film and underlying Ta interlayer were released from a dissolvable substrate after dealloying; the film was folded on itself, showing both the bottom of the film toward the substrate (top inset) and the top surface of the nanoporous film (inset at right). Ligaments at the bottom of the film are perpendicular to the substrate, as opposed to lying flat on the substrate surface.

Crystalbond droplet after dealloying, and the nanoporous film became folded at this location. Two areas (Figure 7.4b insets) were enlarged to view the AuPd ligaments at the top film surface (inset at right) and near the Ta layer at the bottom (inset at left). The bottom layer of ligaments is seen to terminate in circular ends that serve as attachment points to the substrate, i.e. they are nanolegs as described above for Figure 7.4a. These nanolegs generally do not contact each other, but simply support the top layer of interconnected np-AuPd ligaments.

The variation in structure of the nanoporous layers at the substrate versus the film surface can be partially attributed to surface oxidation of the Ta interlayer. During dealloying, the majority of Ag and Pd atoms are etched from the precursor film, exposing most of the Ta surface to the strongly oxidizing nitric acid solution. This creates a surface layer of tantalum oxide that resists further chemical attack, but the np-AuPd ligaments do not bond with this chemically inert oxide. Only the locations of incipient AuPd clusters are able to retain sufficient metallic Ta to yield a strong ligament-substrate bond. As there is no wetting between AuPd and tantalum oxide, the first layer of ligaments consists of nanolegs that stand perpendicular to the substrate. Above this, the random nature of AuPd agglomeration results in a 3-D network of ligaments and pores. Although this explanation does not predict a preferred orientation for the nanoleg axes, it is expected that the nanolegs are oriented along <111> directions, as a dealloyed metal retains the original crystallographic orientation of its precursor alloy. In this case, <111>-oriented nanolegs are similar to Au nanorods prepared by electrochemical deposition through a template [21].

The findings presented here allow the final structure of nanoporous AuPd films to be tuned by adjusting the thickness of the precursor alloy film. In order to produce a 2-D network of interconnected ligaments that lie on the substrate (similar to the right side of Figure 7.3), the AuPdAg alloy film should be 30 nm thick. The 50% thickness decrease that occurs during dealloying will result in ~15 nm thick ligaments, the same size observed in Figure 7.3. Alternatively, for a single-layer np-AuPd network supported by nanolegs, the thickness of the AuPdAg alloy film should be ~60 nm. While the exact thicknesses of AuPdAg precursor alloy films for producing a given nanoporous structure are particular to the material system discussed here, this approach should be generally applicable, e.g. to thin films of nanoporous Au, Pt, Pd, Cu.

7.4 Summary

The edge regions of patterned np-AuPd grid squares revealed a transition from isolated nanodots to single-layer ligament networks and finally to multilayer nanoporous films, with concomitant changes in ligament structure. Nanodots were created in the thinnest edge regions, where the available volume of Au/Pd was insufficient to produce an interconnected network. In thicker areas, single-layer films consisted of a 2-D network of ligaments. In the thickest film regions, a 3-D nanoporous network of interconnected ligaments was generated. However, the bottom layer of this film consisted of individual “nanolegs”, oriented perpendicular to the substrate, which supported the porous network above. It is proposed that nanoleg formation was enhanced by oxidation of the Ta interlayer over most of the substrate area, except at locations of incipient AuPd agglomeration where bonds with metallic Ta were established. The final structure of ultrathin nanoporous noble metal films can be controlled by tuning the thickness of the precursor alloy film.

CHAPTER 8

Hydridation and Dehydridation Behavior of Np-PdNi Thin Films

8.1 Introduction

Pd is a typical transition metal with high reactivity to H_2. As pressure-composition isotherms of the Pd-H system [1-3], Pd exhibits a good capability for H absorption at low and elevated temperatures due to a wide miscibility gap in between α- and β-PdH_x phases. With varying H content in the hydride, PdH_x can alternate between α ($x = 0.015$, $T = 293K$) and β ($x = 0.58$) phases [3].When Pd exposes in an atmosphere containing H_2, H atoms can be absorbed in face-center cubic (FCC) Pd lattices after dissociation of H_2 on Pd surfaces. Under an appropriate surface/subsurface condition of the Pd for H_2 dissociation [4-8], H atoms can be trapped at tetrahedral sites on the surface, octahedral sites in the FCC lattices, grain boundaries, dislocation cores, and vacancy sites in Pd matrix [9, 10]. This H absorption can cause volume expansion of Pd lattices and lead to local stress/strain [10, 11].

For enhancing reactivity between Pd and H_2 by increasing surface area of Pd, Pd has been reported to be produced in several forms, including nanoparticles [12, 13], nanocrystals [14-16], thin films [17, 18], and Pd thin films coated on a porous substrate [19] or nanowires [20]. Additionally, Pd was produced in a nanoporous form to increase surface area [21, 22]. Under preparing Pd in these forms by nano-engineering, the miscibility gap differs from large-sized Pd, and Pd surface condition plays a more dominant role in H absorption/desorption [14, 15, 23].

In the nano-sized Pd, H content increases in α-PdH_x ($x < 0.06$, but 0.015 for bulk Pd), but decreases in β-PdH_x ($x > 0.3$, but 0.58 for bulk Pd) [24, 25]. This change in H content leads to a narrower miscibility gap of H in Pd, and nucleation of nanocrystalline β-PdH_x occurs with a higher H content than in bulk Pd. As surface-to-volume ratio increasing in the nano-sized Pd, surface/subsurface condition (e.g. crystal planes and surface impurities) and lattice imperfection (e.g. vacancies, dislocations, grain boundaries and deformed lattices) are more critical to affect H absorption/desorption behavior [10, 15, 16, 26, 27]. The increased surface area of the nano-sized Pd offers much more sites on Pd surfaces for H_2 adsorption/dissociation and followed chemisorption. However, the higher surface area of the nano-sized Pd cannot bring a higher capability of H absorption (actually, reducing the capability by 50%) because of a lower H content in β-PdH_x and anisotropic deformation of Pd lattices [15]. But interestingly, an abnormally high capability of H (H/Pd = 3, and even 8 for some transition metals) was obtained when Pd particles were as small as 1 nm due to extremely high surface curvature, which provides a high amount of sites at steps and edges of low-index Pd crystal planes for H absorption [23, 28]. Although capability of H content in the nano-sized Pd may be not increased with increasing the surface area, this nano-sized Pd desirably exhibits a high reaction rate with H_2, yielding this material to be ideal for H_2 sensing applications with short response time even if in an atmosphere containing a low amount of H_2. For satisfying requirements of structural strength and surface area for H_2 sensing devices, the nanoporous thin film might be a good candidate material for sensing, i.e. Pd or Pd-based alloys.

Dealloying, or selective corrosion, is a reliable process for dissolving one or more metal components from a precursor alloy. By using a proper etching solution with a high selectivity of corrosion between alloyed elements, less noble elements can be dissolved from the alloy more easily. Meanwhile, more noble elements can form a nanoporous structure with 3-D interconnected ligaments that range in size from several nm to tens of nm. Dealloying has been used for producing a variety of nanoporous metals, such as nanoporous gold (np-Au) [29-31], copper (np-Cu) [32], Nickel (np-Ni) [33] and palladium (np-Pd) [21, 34]. In order to achieve a finer porous structure, adding surfactants to etching solution was helpful in decreasing ligament/pore size down to 5 nm [35], which should yield high performance for H_2 sensing.

In this study, nanoporous np-PdNi thin films were prepared by dealloying co-sputtered Pd-Ni precursor alloy films, and the np-PdNi were cycled in a mixed N_2-H_2 atmosphere containing different H_2 content to investigate hydridation and dehydridation behavior. In addition to microstructure of the np-PdNi thin films, effects of ligament/pore size, film thickness and content of the remained sacrificial element (i.e. Ni) on H_2 cycling measurements will be presented and discussed.

8.2 Experiments

PdNi precursor alloy films were co-sputtered on a Si substrate (CrysTec GmbH, Germany) using Ar plasma in a high vacuum sputtering system (ORION, AJA International Co., base pressure ~1×10^{-6} Pa). The Si substrate was (100)-oriented single crystal, 180 μm thick, double-side polished, 3-inch in diameter, and coated with a 50 nm amorphous SiN_x layer on both the sides. The amorphous SiNx surface was cleaned prior to film deposition by ion etching back at 35 W (RF power) for 1.5 min in Ar plasma to clean up the surface and create nucleation sites. For improving adhesion of the PdNi film, Ta and Pd interlayer (2 nm for each) was in turn deposited prior to deposition of the PdNi film. PdNi films were deposited with a given film thickness of 25, 90 or 200 nm with substrate biasing in Ar plasma at 35 W (RF power). Composition of the PdNi alloy was

18 at.% Pd and 82 at.% Ni. The film composition was optimized to prevent film cracking during followed dealloying and to obtain an ideal nanoporous structure.

As-deposited PdNi films were (111)-textured and dealloyed in diluted sulfuric acid (25 vol.%) until the PdNi (111) peak disappeared in x-ray diffraction (XRD) scans. Dealloying time depends on film thicknesses of the as-deposited PdNi alloy (e.g. 1, 5 and 17 hrs for 25, 90 and 200 nm films, respectively). Oleic acid ($C_{17}H_{33}COOH$, 90% purity, Alfa Aesar, USA) and oleylamine ($C_{18}H_{35}NH_2$, 70% pure, Alfa Aesar, USA) were added to the diluted sulfuric acid as surfactants for immobilizing surface diffusion of Pd atoms during dealloying [35]. Dealloyed specimens were cleaned in boiling ethanol (95 % purity) for 30 min, rinsed with ethanol for 20-30 sec, and soaked in ethanol for 15 hrs to remove residual surfactants and sulfuric acid before subsequent characterization.

Film texture of as-deposited and dealloyed films was analyzed by XRD (Siemens model D500). PdNi alloy peaks in all XRD scans were calibrated by Si (400) peak, 69.15° (2θ). Consistent scanning parameters were applied to all specimens: 0.01° step size and 0.1°/min scan rate. Microstructure of the np-PdNi films was characterized using a SEM (Hitachi S900, operated at 3kV with secondary electron imaging mode) and STEM (JEOL 2010FX, operated at 200kV). Composition of as-deposited and dealloyed films was determined using the EDS attached to Hitachi SEM S3200. H_2 cycling behavior of np-PdNi films were measured by film stress change with the np-PdNi on 3-inch wafers, performed using a wafer curvature system (FLX-2320-S, Toho Technology Co.) in an atmosphere-controlled chamber. The cycling atmosphere was N_2 (ultrahigh purity, 99.999 %) mixed with H_2 (0-grade, 99.9 %), and H_2 content was varied from 0 vol.% to 20 vol.%. during the cycling measurement. Time interval of film stress measurement was 15 sec.

8.3 Results

After completion of dealloying with surfactants, all films exhibit a microstructure with nanoporosity. Figure 8.1 shows plan-view microstructure of 25nm-30Ni, 90nm-coarse, 90nm-fine and 200 nm np-PdNi films, see details in Table 8.1. Ligaments in these films with fine ligaments (i.e. 25nm-30Ni, 90nm-fine and 200 nm films) were 3-5 nm wide and 5-10 nm long, and pores were 5-10 nm in diameter. Several abnormally large pores were observed in the 200 nm film. Some clusters showing a higher brightness in Figure 8.1a were suggested as the remnant PdNi alloy, which was not completely

Table 8.1 Remnant Ni content (determined by EDS) and thickness of np-PdNi films. thickness was estimated by assuming film contraction of 45% during dealloying, and was also measured from cross-sectional SEM micrographs. Due to different dealloying processes, 25 and 90 nm films exhibited variations in remnant Ni content (low vs. high) and ligament size (fine vs. coarse). Note that ligament size of most films was ~5 nm, but was 10 nm for the "90 nm coarse" film.

PdNi alloy thickness (nm)	remnant Ni (at. %)	estimated/measured film thickness after dealloying (nm)	ligament size (scale of porosity)
25	10	15/----	fine
25	30	15/----	fine
90	46	50/50	fine
90	23	50/50	coarse
200	45	110/110	fine

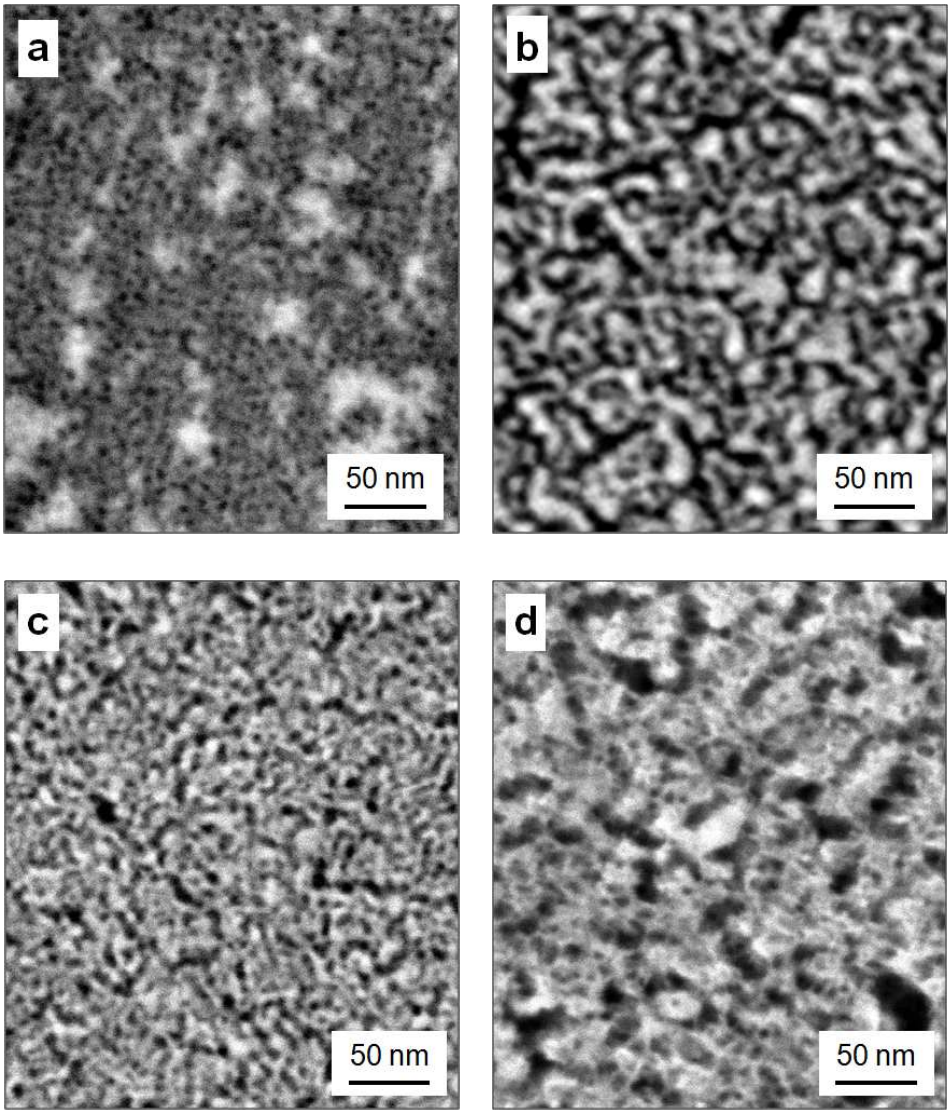

Figure 8.1 Microstructure of (a) 25nm-30Ni, (b) 90nm-coarse, (c) 90nm-fine and (d) 200 nm np-PdNi films. Pore and ligament sizes in micrographs a, c and d were ~5 nm (except some abnormally large pores observed in micrograph d). Pores and ligaments in micrograph b were ~10 nm. All np-PdNi films exhibited 3-D interconnected ligaments and open pores.

dissolved during dealloying. Comparing to 200 nm film (Figure 8.1d), thinner films (25 and 90 nm films, Figures 8.1a-c) exhibited a more uniform porous structure in ligament and pore sizes. It is due to the shorter time needed for dealloying completion for thinner alloy films. The shorter dealloying time resulted in some more stable conditions of the nanoporous films, such as film thickness contraction and surfactants reactivity in the etchant solution. Additionally, the thinnest film exhibits the lowest remnant Ni content in the final nanoporous film under the same dealloying condition (e.g. 30 at.% Ni remained in 25 nm films but 42-46 at.% Ni in thicker films).

In the study, five np-PdNi specimens were used to investigate effects of film thickness, remnant Ni content and ligament size on hydridation and dehydridation behavior. 25 nm np-PdNi films have fine ligaments but different remnant Ni content, 10 at.% and 30 at.%, which were denominated by 25nm-10Ni and 25nm-30Ni, respectively. The 25 nm films were used to investigate effects of remnant content. 90 nm np-PdNi films have different ligament size (with different remnant Ni content), named by 90nm-fine and 90nm-coarse. The 90 nm films were able to show effects of ligament size when effects of remnant Ni content were clarified. The 200 nm np-PdNi film has fine ligaments and the same remnant Ni content as 90nm-fine specimen, using for investigating effects of film thickness. (See details in Table 8.1)

Using a different etchant recipe with a higher etching selectivity to Ni for dealloying, np-PdNi films can be produced with a lower remnant Ni content of 10 at.%, which was 30 at.% in 25 nm films dealloyed by the recipe the same as for thicker films. Figure 8.2 shows plan-view morphology of the 25nm-10Ni np-PdNi film, observed using STEM. In the STEM micrograph, it is seen that ligaments were 2-4 nm wide and 6-9 nm long, and pores were 5-10 nm in diameter. By taking a closer observation, some ultrafine pores were seen on ligaments. These ultrafine pores were ~1 nm in diameter, which led some ligaments to have some ultrafine porosity. Estimated thickness of this np-PdNi film was 15 nm, which is close to the cell size (one ligament plus one pore). So, it is suggested that the film contains only 1-2 cells through the film thickness.

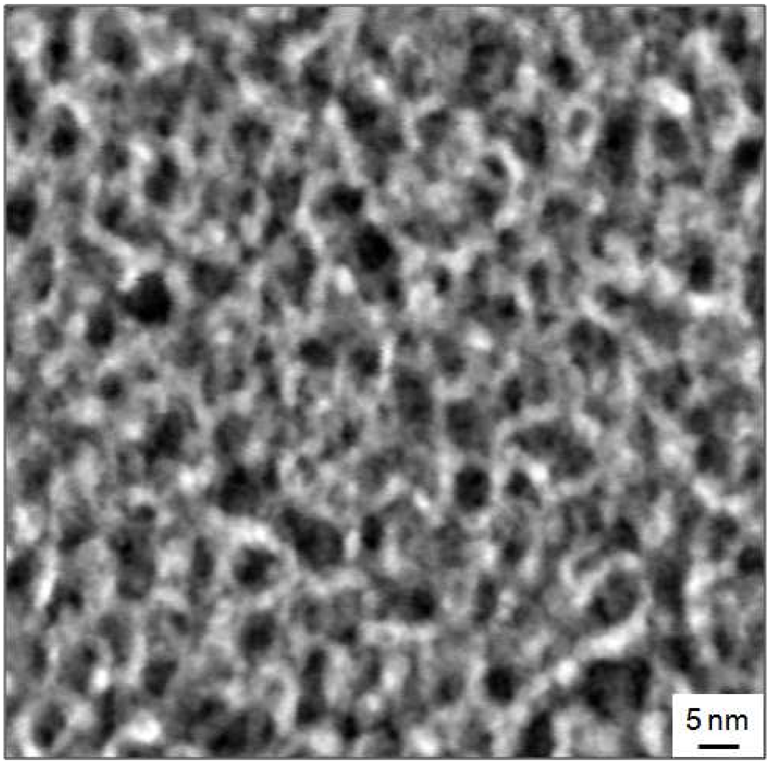

Figure 8.2 STEM micrograph of 25nm-10Ni film. Most ligaments were 2-4 nm wide and 6-9 nm long. Pores were 5-10 nm in diameter. Some ultrafine pores were observed on ligaments with a pore size of ~1 nm in diameter.

Pd lattices can expand during hydridation due to occupation of H atoms at interstitially octahedral sites in Pd FCC lattices, which lattice expansion leads the Pd to be more compressive (or less tensile) due to the solid, thick substrate (Si). Conversely, dehydridation can cause contraction of Pd lattices and an accompanied tensile (or less compressive) stress [10, 11, 15, 36]. So, change in film stress is able to evaluate H absorption and desorption of Pd or Pd-based thin films, including np-PdNi and dense Pd.

Stress of the dense Pd and np-PdNi films was measured during the H_2 cycling test that H2 content was switched from 0 vol.% to 10 vol.% and held for 10 min; then, the H_2 content was switched off (0 vol.%). In Figure 8.3, the film stress was normalized by effective film thicknesses for np-PdNi films, such as 15 nm for the 90 nm np-PdNi film (with coarse ligaments, 23 at.% Ni remnant) and 42 nm for the 200 nm np-PdNi film (with fine ligaments, 45 at.% Ni remnant). When H_2 content was switched on at 10 vol.%, stress of the dense Pd film (100 nm thick) and np-PdNi films rapidly became compressive. The dense Pd film exhibited two plateaus in the compressive stress region. The film stress gradually reached the first plateau (-230 MPa) by 5 min and the second plateau (-370 MPa) by 10 min. The np-PdNi films showed a significant difference in stress transition. Stress of the coarse np-PdNi film (90 nm thick) increase by ~200 MPa in compression within 30 sec, and the compressive stress gradually reached -270 MPa in 10 min. However, fine np-PdNi films (200 nm thick) exhibited the rapidest stress change by -63 MPa in the first 15 sec, and the film stress was slowly equilibrium to -25 MPa by 10 min. This stress equilibrium during hydridation was not observed for np-PdNi films with coarse ligaments. When H_2 content was switched off (0 vol.%), stresses of the np-PdNi films recovered back to the original stress in 15-30 sec, but the dense Pd film took 1 min for stress recovery.

Performance of these films during hydridation and dehydridation can be considered by two factors: response time and capability. As stress curves shown in Figure 8.3, the fine np-PdNi film showed the shortest response time but its capability of H absorption (determined by stress change) was the lowest. Conversely, the dense Pd film exhibited the slowest rate to saturation (the highest compressive stress) and the highest capability of H absorption. It is interestingly found that np-PdNi films showed different stress transition during hydridation if the films were with fine or coarse ligaments. This is addressed as effect of ligament size and will be discussed later

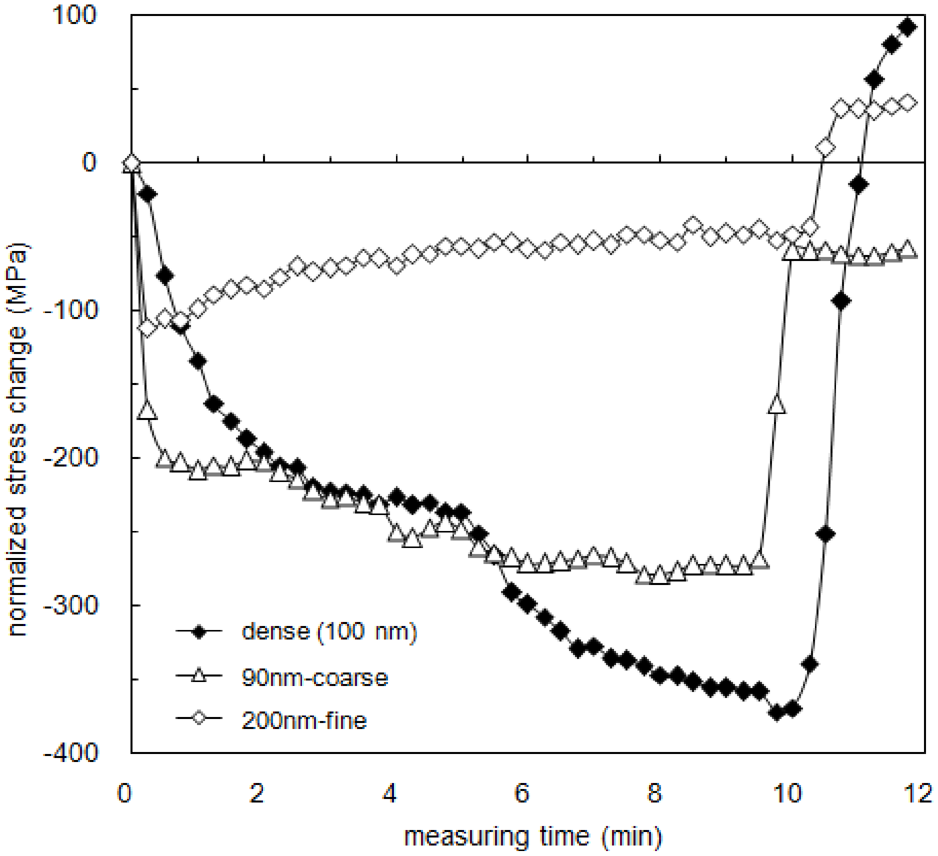

Figure 8.3 Stress changes in 100 nm dense Pd, 90nm-coarse and 200 nm np-PdNi films, measured when H_2 content was switched between 0 and 10 vol.% in the N_2-H_2 mixed atmosphere. The dense Pd film exhibited two plateaus and the longest time to saturation of stress. The 90nm-coarse np-PdNi film displayed a more rapid response than the dense Pd film. The 200 nm np-PdNi film exhibited the shortest time to saturation of stress, probably due to its thinner ligaments.

Hydridation and dehydridation behavior of np-PdNi films with fine ligaments was repeatedly tested in an atmosphere with a H_2 content switching in between of 0 or 10 vol.% by three cycles. Change in film stresses during this H_2 cycling test is shown in Figure 8.4. The tested np-PdNi films were with fine ligaments and the same remnant Ni content of ~45 at.%, but film thicknesses were 90 nm and 200 nm. As stress curves shown in Figure 8.4a, these np-PdNi films presented good repeatability of change in film stress, which change was corresponded to H absorption and desorption in np-PdNi films. 90 nm np-PdNi film exhibits a stress difference ~60 MPa in between hydridation (10 vol.% H_2) and dehydridation (0 vol.% H_2) stages, but 200 nm np-PdNi film shows a lower stress change of ~35 MPa. This might be due to film contraction during dealloying for the thicker films to be more than the thinner films (e.g. film thickness contracted during dealloying by 45 % and 63 % for 90 nm and 200 nm as-deposited alloy films, respectively). Under the higher film thickness contraction, thickness of the dealloyed 200 nm film used for calculating film stress was over-estimated (see Table 8.1) and resulted in a lower stress change.

Interestingly, stresses of these np-PdNi films during hydridation were not at a steady value, but the initial high compressive stress was released with measuring time. This stress equilibrium can be seen clearly in the first cycle but gradually alleviated in the followed cycles. It is suggested that equilibration of film stress might be caused by H diffusion from ligament surface to the core, and the stress can be at a steady value when gradient of H content in the ligament disappeared. Taking 200 nm film as an example, the H diffusion, took 10 min to reach the steady stress (-32.5 MPa) in the first cycle but 7.25 and 5 min in the second and third cycle, respectively, which are indicated by arrows in Figure 8.4a. This result presents that the shorter time was needed for stress equilibration in the followed cycles. Detailed mechanisms of this phenomenon will be discussed in this article.

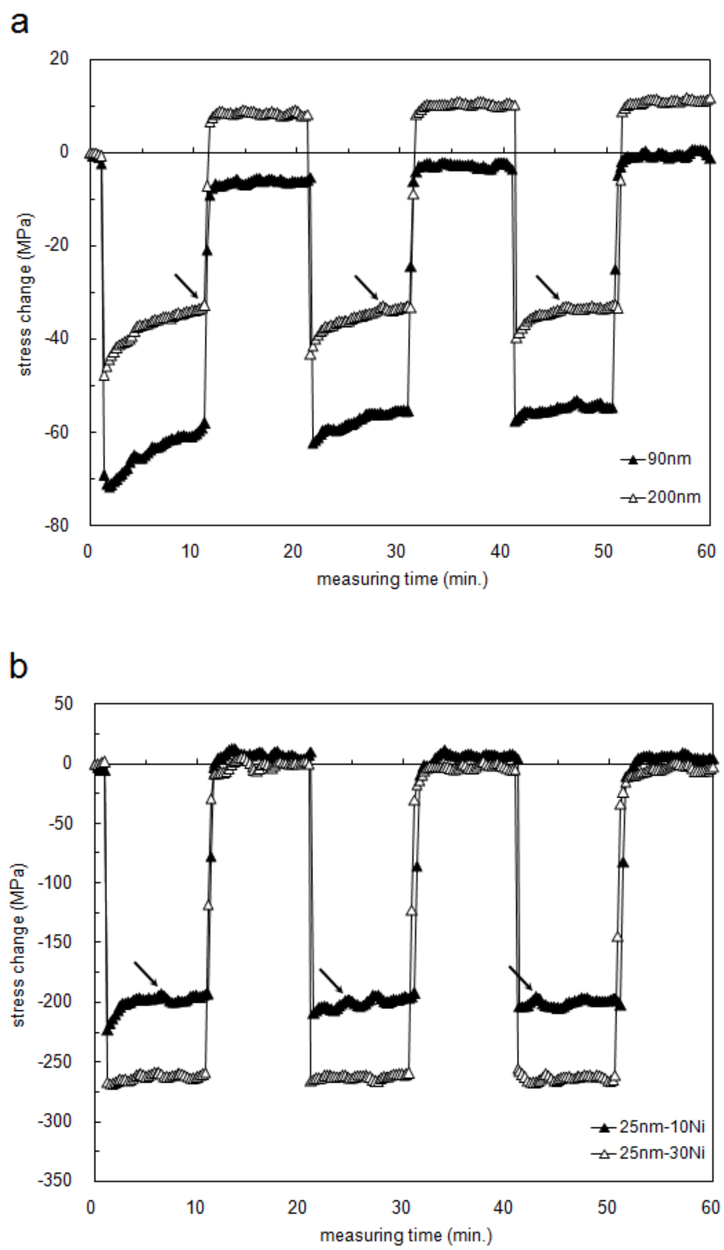

Figure 8.4 Stress curves of (a) 90nm-fine and 200 nm; and (b) 25nm-10Ni and 25nm-30Ni np-PdNi films during H_2 cycling measurements. Hydrogen content in the flowing atmosphere was switched between 0 and 10 vol.%. Arrows indicate the points at which stress is considered to have equilibrated.

The np-PdNi films measured in Figure 8.4b were with fine ligaments and the same film thickness of 25 nm, but these two films have different remnant Ni content of 10 at.% or

30 at.%, named 25nm-10Ni and 25nm-30Ni np-PdNi films. Stress change of 25 nm-10Ni and 25nm-30Ni np-PdNi films between hydridation and dehydridation stages was ~200 MPa and ~270 MPa, respectively. During hydridation, 25nm-10Ni film exhibited clearer stress equilibration than 25 nm-30Ni film. Additionally, stress of 25nm-10Ni film reached a steady value (-195 MPa) by a shorter time for the cycle than the prior cycle (e.g. 5.5 min, 3.75 min and 2 min for the first, second and third cycle, respectively, indicated by arrows in Figure 8.4b), which phenomenon is the same as stress curves shown in Figure 8.4a.

H absorption and desorption behavior of np-PdNi films were also tested in an atmosphere with varied H_2 content (0, 2, 6, 10, 15 and 20 vol.%). Film stress under the atmosphere was averaged by all data points (time interval of each measurement of 15 sec) during the holding time of 3 min for every H_2 content. The averaged film stresses of np-PdNi films are shown in Figure 8.5. Stress curves of 25 nm films were roughly symmetric during H_2 content increasing and decreasing stages. 25nm-30Ni film exhibited more significant stress change than 25nm-10Ni film in all H_2 content. Additionally, the thicker films (90 nm and 200 nm) showed smaller stress changes in the test. Similar to 25 nm films, both thicker films exhibited the highest compressive stress in 20 vol.% H_2. But, stress of 200 nm film in 2 vol.% H_2 was ~90% of the highest compressive stress in 20 vol.% H_2. In other words, 200 nm film can be rapidly saturated by a low amount of H_2 content in the atmosphere. This rapid saturation of H absorption is suggested that the thicker film has the longer and more curved channels (pores) through the film thickness. Moreover, mean free path of gas molecules at 1 atm is ~70 nm, but the channel width (pore diameter) is 5 nm. So, these long channels might be helpful in trapping H_2 molecules for absorption due to higher possibility of collision between H_2 molecules and ligament surface. Conversely, the thinner films exhibit a better symmetric stress change and larger stress change corresponding to varied H content in the atmosphere, which are ideal for applications of quantified H_2 sensing.

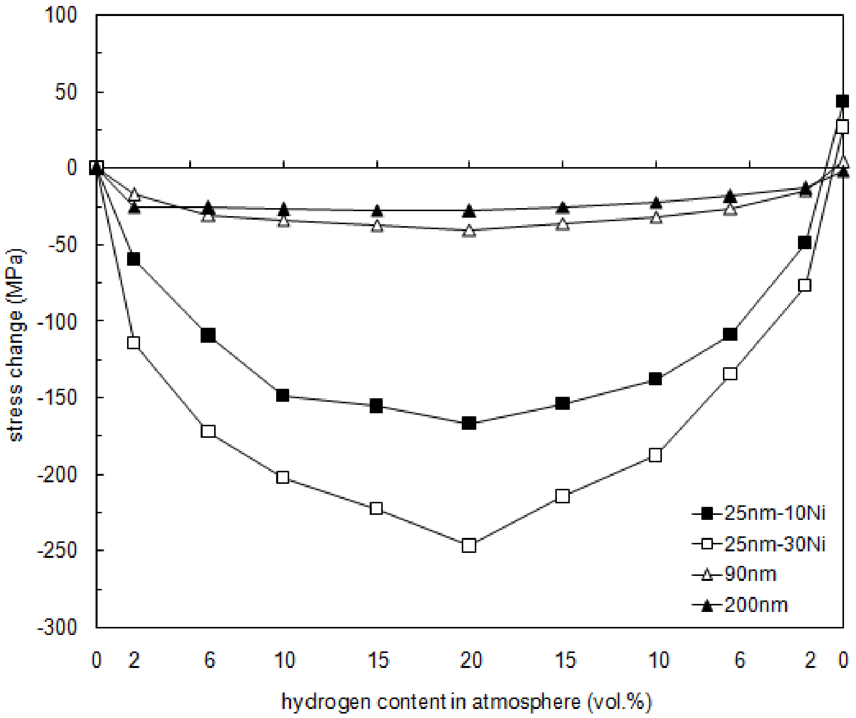

Figure 8.5 Average stress changes in 25nm-10Ni, 25nm-30Ni, 90nm-fine and 200 nm np-PdNi films as H_2 content was stepped through increasing then decreasing levels. The thinner films (25 and 90 nm films) exhibited more symmetric curves during H_2 cycling. The two 25 nm films also showed the highest stress changes at maximum H_2 levels.

8.4 Discussion

As results talked above, two issues need to be discussed in details: hydridation/dehydridation of ligaments and effects of film thickness, ligament size and remnant Ni content on hydridation/dehydridation behavior, for clarifying details about using np-PdNi films for H sensing applications.

8.4.1 Hydridation and Dehydridation of Ligaments

Once H_2 molecules reached ligament surface, some H_2 molecules were successfully physisorbed on ligament surface. These physisorbed H_2 molecules dissociated to H atoms if the pressure and temperature are high enough. Sequentially, the dissociated H atoms were chemisorbed at surface and/or subsurface sites in ligaments. Chemisorption of H atoms led to formation of β-PdH_x in Pd(Ni) lattices. Due to extremely high surface curvature of ligaments (5 nm in diameter), β-PdH_x can densely nucleate on ligament surface, where had high density of atomic steps, kinks and vacancies. After nucleation of β-PdH_x on ligament surface and subsurface, diffusion of H atoms was one of the primary mechanisms to dominate further hydridation of the entire ligament.

Figure 8.6 shows stress curves of 200 nm film during hydridation (10 vol.% H_2, held for 10 min in each cycle), which were taken from the measurement presented in Figure 8.4a. In the figure, stress curve in each hydridation cycle can be divided by 2 or 3 regions exhibiting different slopes. The 2nd cycle is taken as an example for region division based on change in slope, which is divided by 3 regions and the division is presented above the curve. Slope of the 1st region in each cycle was in a range of 3.36-5.61, which is higher than the 2nd region of 0.69-0.73 and the 3rd region of ~0. Additionally, transition time between the 1st and 2nd regions of the 1st, 2nd and 3rd cycles was 3.75, 1.75 and 1.5 min, respectively, and transition time between the 2nd and 3rd regions was 7.25 min for the 2nd cycle and 5 min for the 3rd cycle (no transition of 2nd to 3rd region for the 1st cycle). It is noted that transition time of 1st/2nd and 2nd/3rd regions decreased cycle by cycle. Slopes of each region/cycle were verified with logarithm plots and can be seen as rates of stress relaxation.

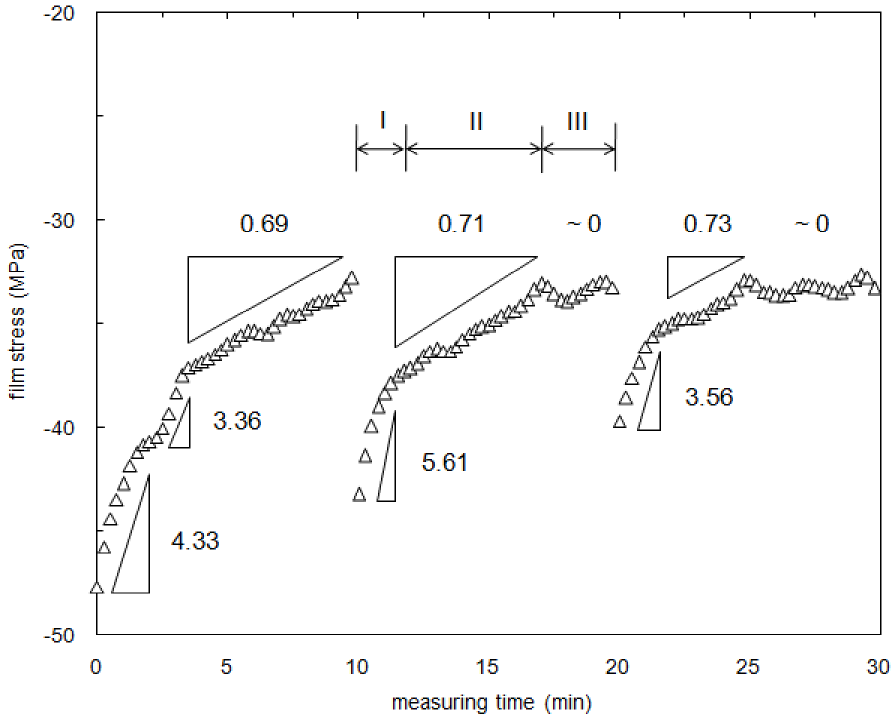

Figure 8.6 Stress relaxation of a 200 nm np-PdNi film during the hydridation segments of three consecutive cycles. Each curve exhibited 2 or 3 stages with different slopes. Although the slope of the 1st stage decreased with each new cycle, the slopes of the 2nd and 3rd stages were consistent in each cycle.

Compressive stress in np-PdNi films during hydridation was caused by expansion of PdNi lattices due to H absorption. Lattice parameter of PdNi lattices has a linear relation to H content. As reported lattice parameters expanded during H absorption [15, 36, 37], expansion of the lattice parameter was 1.8×10^{-2} when x=0.3 in nanocrystalline Pd(Ni)H_x. The expansion value is strain of the porous film under compressive stress. Gibson and Ashby [38] proposed a way to compare the modulus of a solid material and its porous counterpart. According to the Gibson-Ashby scaling law, modulus of the np-PdNi can be written by

$$M^{*}_{np-PdNi} = M_{PdNi}\left(\frac{\rho_{np-PdNi}}{\rho_{PdNi}}\right)^{2} \tag{8.1}$$

where M_{PdNi} and ρ_{PdNi} are the bi-axial modulus and density of the solid PdNi, and $\rho_{np\text{-}PdNi}$ is density of porous PdNi. Therefore, the term of $\rho_{np\text{-}PdNi}/\rho_{PdNi}$ is relative density of the np-PdNi, which was 0.285. Additionally, texture of the PdNi films is (111), which was characterized by XRD before and during dealloying. So, bi-axial modulus of the (111)-textured np-PdNi films can be calculated by

$$M_{111} = \frac{6c_{44}\left(c_{11}+2c_{12}\right)}{c_{11}+2c_{12}+4c_{44}} \tag{8.2}$$

$$M_{PdNi,111} = M_{Pd,111}X_{Pd} + M_{Ni,111}X_{Ni} \tag{8.3}$$

where c_{ij} is stiffness of pure Pd and pure Ni [39], and X is fractions of Pd and Ni in the np-PdNi film.

As equation (8.2), $M_{Pd,111}$ and $M_{Ni,111}$ are 287 GPa and 390 GPa, respectively. Content of Pd and Ni in np-PdNi were 55 at.% and 45 at.%, respectively. Based on the calculated values of bi-axial moduli and measured compositions of Pd and Ni, $M_{PdNi,111}$ is 334 GPa. Using Gibson-Ashby scaling law, bi-axial modulus of np-PdNi is 27.1 GPa. A plot of measuring time vs. strain of the 200 nm np-PdNi film can be generated from measured stresses in Figure 8.6. Figure 8.7 shows strain relaxation curves during hydridation of the 200 nm np-PdNi film. Strain was relaxed both with measuring time and cycle by cycle, which exhibits similar curves to stress relaxation. However, the measured strain was in a range of $1.2\text{-}1.8\times10^{-3}$, which is only one tenth of the calculated strain (1.8×10^{-2}). In addition to elastic deformation of the np-PdNi film, another mechanism is considered to interpret stress/strain relaxation during hydridation –

formation of defects in ligaments. Under a high compressive stress, Pd(Ni) lattices can deform and even create defects to relax the stress. The lattice deformation can be elastically and plastically, and defects may need to be formed because of a significant stress in the 5 nm wide ligaments during hydridation.

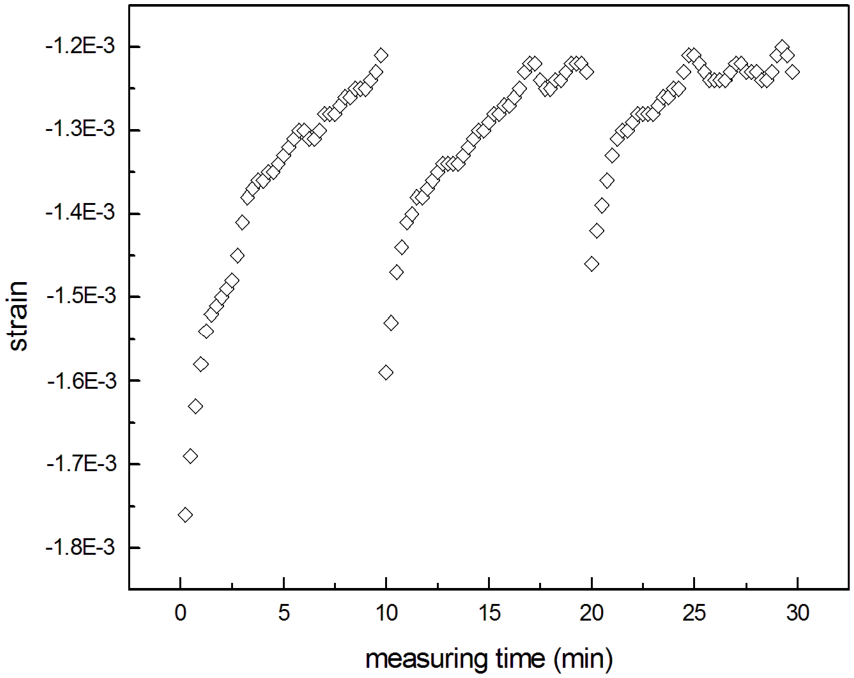

Figure 8.7 Strain relaxation of a 200 nm np-PdNi film during the hydridation segments of three consecutive cycles. Strain values were calculated from stresses measured by wafer curvature system.

It is reported that misfit dislocations can be generated at incoherent boundaries between the β-PdH$_x$ precipitates and the α-PdH$_x$ matrix during hydridation in bulk metals [40, 41]. However, dislocations were not observed in the ligaments by TEM in the study. Also, couple studies present that no dislocations were formed in hydrogenated Pd clusters due to the high energy needed for creation of dislocations in such small clusters (~3 nm) [25, 42]. Based on thermodynamics, formation of linear defects (e.g. dislocations) can create a much higher increase in energy than point defects, such as vacancies. It has been reported that abundant vacancies can be formed during hydridation of Pd [43]. Formation of vacancies was observed in PdH_x at high H_2 pressures [44], high torsion [45] or high temperatures [46]. Furthermore, amounts of vacancies formed during hydridation can be much higher than at the thermal equilibrium state [47-49]. In addition, vacancies in the host lattices (e.g. Pd) have a strong interaction with interstitial atoms (e.g. H), and the interstitial-vacancy interaction may change coherency of lattice structures [50] and local stress fields [51].

Avdyukhina et al. [51] used Pd-Mo alloy (5 at.% Mo) to investigate role of vacancies in the structural relaxation and report that formation of one vacancy in a Pd(Mo) unit cell can cause the unit cell having a volume contraction of 20%, which corresponds to a 7.2% linear contraction of edges of the unit cell. Fukai and Okuma [44] present concentration of vacancies in PdH_x can be 18 at.% at 800°C and a H_2 pressure of 5 GPa, and XRD scans show that a vacancy-ordered structure of Pd_3VacH_4 can be formed with superlattice structure of Cu_3Au phase at 300°C. They also suggest that such a large amount of vacancies and the vacancy-ordered structure may be formed at lower temperatures. The vacancy-ordered structure was also observed by Miraglia et al. in the hydrogenated Pd sheet with vacancy concentration of 20 at.%. Formation of the vacancy-ordered structure requires migration of vacancies within a local area, which is vacancy rearrangement in the host lattices.

Stafford and Bertocci [52] estimated compressive stresses in Pd thin films under H/Pd values of 0.45 and 0.6 were 2.5 GPa and 8.4 GPa, respectively. Nanostructured Pd has a narrower miscibility gap in between α-PdH_x and β-PdH_x phases, which yields lower stresses and volume expansion of the Pd lattices. However, the interfacial stress in PdNi ligaments may be still too high to be relaxed by elastic deformation only, and formation of vacancies may be the other mechanism to relax the residual stress during hydridation. As the difference between calculated strain (1.8×10^{-2}) and measured strain ($1.2\text{-}1.8\times10^{-3}$) of the 200 nm np-PdNi film during hydridation, concentration of vacancies can be estimated by the 7.2% linear contraction of a unit cell containing one vacancy, which is ~5 at.%. The amount of vacancies (5 at.%) means that every five unit cells contain one vacancy.

Figure 8.8 shows log-log plot of stress change vs. measuring time for three hydridation cycles of the 200 nm np-PdNi film. In the 1st cycle, slope of the 1st stage (stage divided same as shown in Figure 8.6) is 1.51 and 1.59. After 3.75 min, the 2nd stage shows a slope of 0.37. However, there was a short time duration about 1 min in the 1st stage which exhibits a slope of 0.33 in between the regions of 1.51 and 1.59. In the 2nd cycle, slope is 1.27 for the 1st stage and changes to 0.32-0.36 at 1.75 min. The 3rd cycle has slopes of 0.72 and 0.31 for the 1st and 2nd stages, respectively. It can be seen that the 1st stage of all cycles shows a higher slope but the slope decreases cycle by cycle, and the 2nd stage of all cycles exhibits slopes in a narrow range.

As Figure 8.8, it is suggested that the 1st stage of stress/strain relaxation might be caused by formation of vacancies, and the 2nd stage of stress/strain relaxation might result from rearrangement of vacancies. Figure 8.9 shows evolution of hydridation and dehydridation of PdNi ligaments. Before hydridation, PdNi ligaments should be with no H atoms and vacancies (or very low amounts of H atoms and vacancies, shown in Figure 8.9a). When H atoms diffused into ligament subsurface, β-Pd(Ni)H_x immediately nucleated and grew to be a closed shell surrounding the α-Pd(Ni)H_x core (Figure 8.9b).

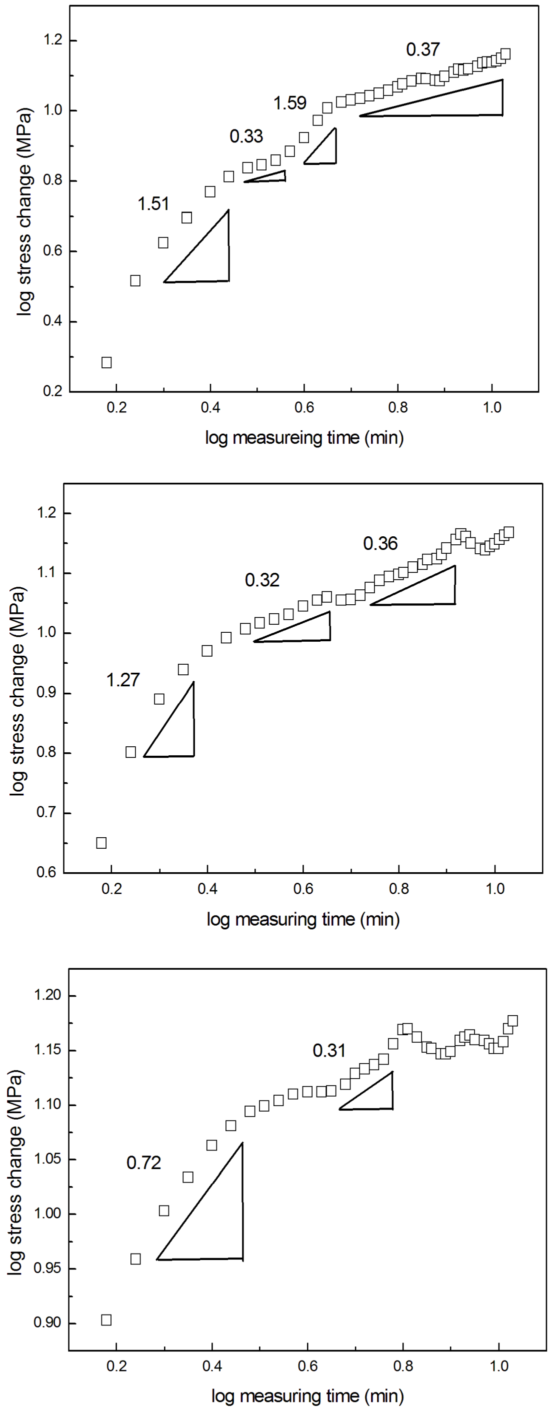

Figure 8.8 Log-log plots of stress change vs. measuring time of a 200 nm np-PdNi film during the hydridation segments of three consecutive cycles. Each curve exhibited 2-4 stages with different slopes. Slope of the 1st stage (0.72-1.59) was higher than the followed stage(s). Slope of the 2nd stage was with a narrow rage (0.31-0.37).

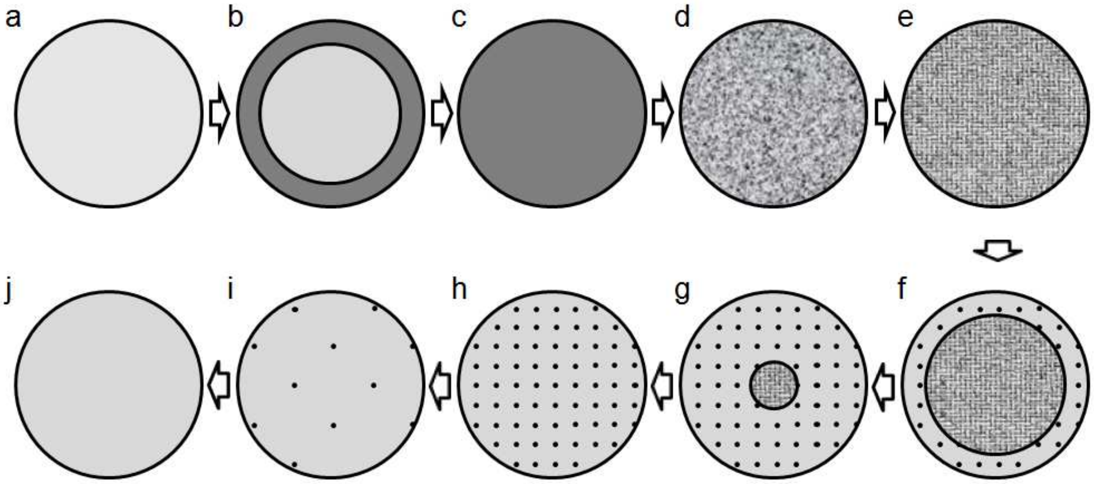

Figure 8.9 Sequence of transformation between α-PdH_x and β-PdH_x across the ligament cross-section during (a-e) hydridation and (f-j) dehydridation. (a) The ligament initially contained no/little H atoms and vacancies in the lattices, represented by a uniform light gray color. (b) When hydridation initiated, lattices near ligament surface absorbed a high amount of H to form β-PdH_x, filled by dark gray as a shell surrounding the α-PdH_x core. (c) The shell grew thicker, and the core reduced. (d) Vacancies were formed due to high compressive stresses. (e) Vacancies rearranged with a long-range ordered structure. During dehydridation, (f) α-PdH_x shell surrounded the β-PdH_x core, and some vacancies were remained in lattices, presented by black spots. (g) The α-PdH_x shell grew thicker. (h) All H atoms were desorbed, and some vacancies were still in the ligament. With being a longer elapsed time, (i and j) vacancies can gradually disappear.

With H diffusion, the entire ligament transformed to β-Pd(Ni)H_x (Figure 8.9c). Transformation of PdH_x phases led the ligament to experience a high compressive stress. The stress can induce formation of vacancies at random sites in the Pd(Ni) lattices to rapidly relax the high stress state (Figure 8.9d). Due to high diffusion rate of H atoms in Pd(Ni), it is suggested that the entire ligament can be completely hydrogenated in 10^{-1} sec

[53]. Therefore, the 1st measurement of each hydridation cycle was taken by the stage of vacancy formation, which exhibits a higher rate to relax residual stress. After the 1st stage of stress relaxation dominated by formation of vacancies, vacancies preferred to rearrange for decreasing gradient of vacancy concentration over the ligament (Figure 8.9e). Rearrangement of vacancies caused the residual stress to be further relaxed but with a lower rate. When the rearrangement finished, stress reached an equilibrium level. During dehydridation, H atoms near ligament surface rapidly escaped from Pd(Ni) lattices. However, the created and rearranged vacancies cannot be removed as rapid as H atoms. Vacancies need time to agglomerate as voids or float to surface. In the 2nd and 3rd cycles, the equilibrium stress can be reached earlier than the 1st cycle. It is suggested that some vacancies were remained in ligaments and the stage of vacancy formation can be shortened. An interesting fact in the study may support this explanation: the 1st hydridation curve can be performed again if the specimen stayed in the air for several days, which means removal of all vacancies and recovery of the lattice structure.

8.4.2 Effects of film thickness and remnant Ni content

Performance of np-PdNi films can be influenced by film thickness and remnant Ni content. Thicker np-PdNi films (e.g. 200 nm) have longer curved channels through the film thickness. The channels are able to trap H_2 molecules because mean free path of gas molecules at 1 atm is 70 nm but average pore size of the porous structure was ~5 nm only. The small pores can limit traveling distance of gas molecules [23]. That is why the 200 nm film exhibited rapid saturation during hydridation and lag of H desorption during dehydridation, shown in Figure 8.5. So, thinner np-PdNi films have a better sensitivity to change in H_2 content in the atmosphere. In addition, as change in film stress (shown in

Figures 8.4 and 8.5), thinner np-PdNi films exhibited a higher capability of H absorption. It might be caused by non-uniform saturation of ligaments through the thick film. That is, ligaments near the film top were easier to reach saturation, but the ligaments near the film bottom were not saturated due to insufficient amounts of H_2 molecules traveling through the long, curved channels to the film bottom.

Impurity in Pd lattices may change mobility and occupation energy of H atoms in pure Pd. Also, stress in lattices may be changed by foreign atoms, such as Ni [54]. Due to different lattice parameters of pure Pd (0.389 nm) and Ni (0.352 nm), remnant Ni atoms can change formation and diffusion energies of vacancies from pure Pd. Remnant Ni atoms might cause less vacancies to be formed during the 1st stage of stress relaxation. It can be seen that the 25nm-10Ni film presented a higher degree of stress relaxation in the 1st hydridation cycle than the 25nm-30Ni film, shown in Figure 8.4b.

8.5 Conclusions

Np-PdNi films were prepared with open pores and 3-D interconnected ligaments. Pore and ligament sizes were from few nm to 10 nm and some remnant Ni (10-46 at.%) were remained in the nanoporous structure, varying by different dealloying recipes. H_2 absorption and desorption behavior of these films were investigated by film stress measurements.

During hydridation, compressive stresses caused by absorption of H atoms can be relaxed to an equilibrated stress level. The stress relaxation was divided into two stages, and mechanisms were interpreted by formation and rearrangement of vacancies. High compressive stresses were firstly relaxed by formation of vacancies for the first few min. Vacancies were rearranged for balancing the concentration, and the residual stress was further relaxed by vacancy rearrangement. Additionally, thicker np-Pd/np-PdNi films contained longer curved channels (pores) through the film thickness, which may cause a higher difficulty in H_2 molecules traveling to the film bottom and yield lower capability of H absorption. Remnant Ni might change local stress fields of Pd(Ni) lattices due to its smaller atomic radius. The change in local stress field might influence the amount of vacancies which were created for the 1st stage of stress relaxation.

Chapter 9

Microstructure and Texture of Os-Ru Coatings for Porous Tungsten Dispenser Cathodes

9.1 Introduction

Dispenser cathodes are usually composed of heating elements at the bottom and a porous tungsten (W) pellet at top of the diode. The porous W pellet is impregnated with barium (Ba) aluminates and coated with a thin film (e.g. platinum-group metals or their alloys). The combination of impregnation and the thin film lowers the work function and operating temperature of the diode which improves the lifetime of the dispenser cathodes. Since the 1970's, osmium-iridium (Os-Ir) and osmium-ruthenium (Os-Ru) have been considered ideal coatings for enhancing electron emission in dispenser cathodes [1]. Os-Ru coatings can lower the work function of impregnated W substrates from 2.1 eV to approximately 1.85 eV, lower than that of rhenium (1.93 eV) and iridium (1.89-2.07 eV) [2, 3]. Much attention has been given to Os-Ru due to its low work function and potential application in so-called *M-type* dispenser cathodes [4].

In general, there are two main factors limiting the lifetime of dispenser cathodes: depletion of the Ba impregnant and degradation of the Os-Ru coating. Both phenomena can be aggravated by operation at high temperatures and cause failure of the dispenser cathodes. Semicon Associates Inc. (a leading commercial cathode manufacturer and collaborator in this study) has suggested from pragmatic processing and operating experience that almost none of their cathodes fail due to depletion of the Ba impregnant. Instead, failure of the cathodes was primarily caused by excessive diffusion of W in the

Os-Ru coating from the W substrate after long-term operation at high temperatures. Although the Os-Ru coating needs some W (~40 at.%) to stabilize and enhance electron emission, the cathode can fail when W content near the top surface of the Os-Ru coating reaches a high level (>80 at.%) [5]. Therefore, excessive W interdiffusion should be inhibited during high-temperature operation to improve the cathode lifetime. The interdiffusion phenomenon is believed to have a close relation to the microstructure of the Os-Ru coating (e.g. grain structure and texture). However, not much attention has been given to the microstructural stability of the top-coating thin films, e.g. Os-Ru films.

Several studies utilized surface analysis and characterization techniques to investigate how surface composition changed with depth using x-ray photoelectron spectroscopy or Auger electron microscopy [6-9]. In addition, Jones et al. [10] and Isagawa et al. [11] characterized as-deposited/activated cathode surfaces and porous W substrates, respectively, using scanning electron microscopy (SEM). All the previous studies focused on either surface analysis or microstructural imaging; but none have clarified relationships between microstructure and composition of the Os-Ru coating. Bell [12] provided more systematic research for understanding the effects of applying a substrate bias during film deposition on the microstructural change of the as-deposited and annealed Os-Ru coatings. He concluded that applying a substrate bias voltage between 50 V and 100 V (DC) during film deposition was optimal for ideal stability of film thickness and composition. The deposition process in the current study, specifically the substrate bias parameter, was based on Bell’s findings.

The texture of Os-Ru coatings can be significantly affected by varying the processing parameters, such as substrate bias voltage and by using different sputtering systems [13, 14]. The result shows the Os-Ru coating deposited with a substrate bias power of 5 W had the highest stability of film microstructure and composition during annealing. A 5 W bias power is equivalent to a DC voltage of 115 V, near the bias voltage range suggested by Bell [12]. Considering paths of bulk diffusion, it is suggested that film texture might be an important factor to W interdiffusion because of the variant planar density of three texture components – (10-10), (0002) and (10-11) – in hexagonal close-packed (HCP) Os-Ru films. Furthermore, a larger grain size in the Os-Ru film might be helpful in inhibiting W diffusion through the film thickness. A more complete study of the effects of processing parameters on the microstructure, composition and texture of Os-Ru coatings was designed with considerations for planar density, texture components, and grain boundary diffusion. Understanding W interdiffusion and its effects will hopefully lead to producing Os-Ru coatings that increase the lifetime of cathodes.

9.2 Experiments

Porous W substrates were prepared from W powders (General Electric, U.S., showing an average particle size of 4.5 μm) by standard powder metallurgical processes. W powders were pressed into circular pellets, 3 mm in diameter and 1.27 mm in height. Sequentially, the as-pressed pellets were sintered at 2200 ˚C for 1 h. The sintered W pellets had ~16% porosity. The top surface of the porous W pellets was CNC-machined into a concave shape. After cleaning in solvents, the W pellets were loaded into sputter systems for film deposition.

There were two sputtering systems used for Os-Ru deposition in this study: an Omega coater (Omega Industries Inc., MN, U.S.) used by Semicon Associates Inc. and an ORION sputter (AJA International Inc., MA, U.S.) used by the University of Kentucky (UK). The base pressures of the Omega and ORION systems are 2.7×10^{-4} Pa (2.0×10^{-6}

torr) and 1.3×10^{-6} Pa (1.0×10^{-8} torr), respectively. Deposition pressure was 2.7 Pa (2.0×10^{-2} torr) for the Omega coater and 3.3×10^{-1} Pa (2.5×10^{-3} torr) for the ORION system. Depositions of Os-Ru films were processed by Ar plasma with a rate of 10 nm/min for the Omega coater and 16.7 nm/min for the ORION system. Substrates were cleaned by Ar plasma etching for 1.5 min at 35 W (equivalent to a DC voltage of 169 V) prior to Os-Ru film deposition. Substrate bias was applied during Os-Ru film deposition at 0 (no biasing), 5 (115 V), 10 (163 V), and 20 W (239 V). The bias can cause an atomic peening effect on the Os-Ru film, and might change texture and film stress in the Os-Ru film. The thickness of as-deposited Semicon films was 610 nm, and UK films were in thicknesses of 150, 300 and 550 nm. Table 9.1 shows deposition parameters in detail. After deposition, a portion of Semicon and UK specimens were annealed at 1050 $^\circ C_B$ (C_B = brightness temperature) for 10 min in a 75% N_2 + 25% H_2 atmosphere.

As-deposited and annealed Os-Ru films were characterized using a SEM (Hitachi S900) for plan-view and cross-sectional observation, operating at an accelerating voltage of 3 kV in secondary electron imaging mode. The texture of the Os-Ru films were analyzed by x-ray diffraction (XRD, Siemens D500), operating at 40 kV and 30 mA with Cu Kα (λ = 1.5406Å) incident radiation. All XRD scans were performed from 30˚ to 50˚ (2θ) with a step size of 0.01˚ and all Os-Ru diffraction peaks were calibrated using the W (110) peak (appearing at a 2θ angle of 40.3˚). Fractions of each Os-Ru texture component were calculated based on the integrated intensities of the individual diffraction peaks. Reproducibility was verified by making two measurements on two specimens processed with the same parameters. The composition of the as-deposited and annealed Os-Ru films was measured by energy dispersive x-ray spectrometry (EDS, Hitachi S3200 SEM) and the reported values are an average of three measurements from a given specimen.

Table 9.1 Deposition parameters and film thicknesses of all Os-Ru films deposited at UK and Semicon.

Specimen	Sputtering system	$P_{deposition}$	Dep. rate (nm/min)	Estimated thickness (nm)	Measured thickness (nm)	Thickness contraction during annealing
Semicon	Omega (Semicon)	2.7 Pa (2.0×10^{-2} torr)	10	----	610	~ 4 %
UK-0W-550nm	ORION (at UK)	3.3×10^{-1} Pa (2.5×10^{-3} torr)	17	550	585	< 5 nm (no contraction presumed)
UK-5W-550nm					540	
UK-10W-550nm					530	
UK-20W-550nm*					520	
UK-0W-300nm				300	250	
UK-5W-300nm					310	
UK-10W-300nm					300	
UK-20W-300nm					240	
UK-0W-150nm				150	140	
UK-5W-150nm					130	
UK-10W-150nm					130	
UK-20W-150nm					130	

* UK-20W-550nm films were deposited by two different deposition rates, 17 nm/min (regular deposition process, listed in Table 9.1 above) and 8.5 nm/min (specimen named: UK-20W-550nm-slow), for understanding effects of deposition rate on texture.

9.3 Results and Discussion

The microstructure of the Os-Ru film in all specimens was observed by plan-view and cross-section. Each SEM micrograph for a given specimen shown in Figures 9.1 and 9.2 consists of a plan-view image (on top) and a cross-sectional image (at the bottom). As-deposited Semicon films have a majority of grains 25-55 nm in size, and preferentially grouped in clusters, isolated by crack-like gaps, as shown in Figure 9.1a. Isolated grain clusters were mostly in a range of 100-200 nm with some minor, thinner crack-like gaps within the interior of a grain cluster. Cross-sectional observation revealed that as-deposited Semicon films consisted of columnar grains, extending completely through the film thickness and roughly perpendicular to the W substrate surface. The columnar grains transformed to equi-axed grains with a grain size of 25-75 nm. Comparing the micrographs in Figure 9.1a with those in Figure 9.1b, it is seen that several equi-axed grains were needed to transform from columnar grains in the as-deposited film and stacked through the film thickness during annealing. Additionally, the thickness of the as-deposited Os-Ru film was 610 nm. However, the film thickness contracted by ~4 % during annealing, corresponding to a thickness (585 nm) of the

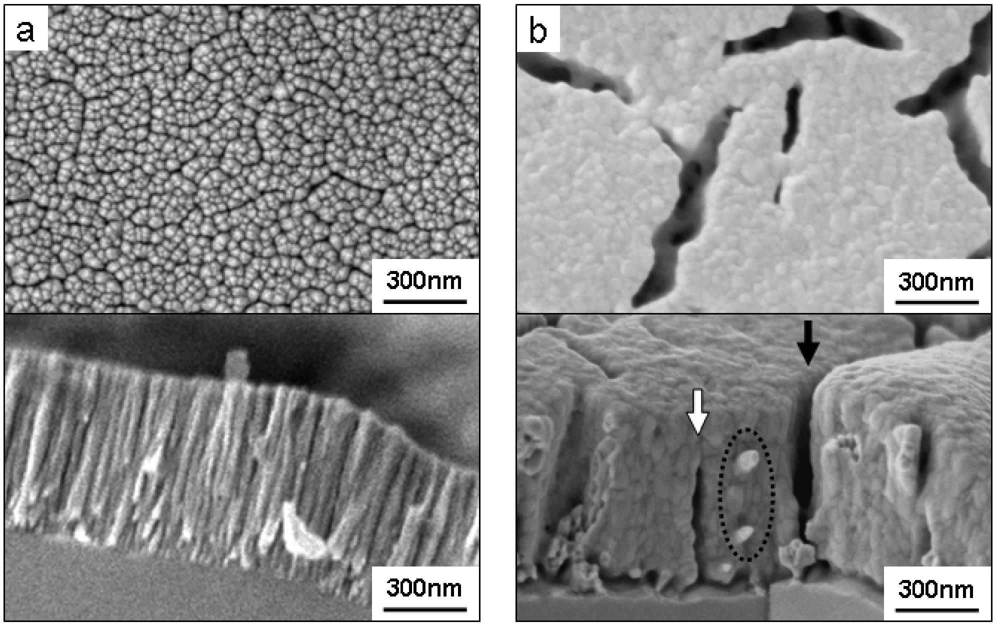

Figure 9.1 (Top) Plan-view and (bottom) cross-sectional SEM micrographs of (a) as-deposited and (b) annealed Semicon films. The annealed Semicon film exhibits micron-cracks dispersing over the Os-Ru film surface and transition of grain structure from columnar grains (before annealing) to equi-axed grains. Cracks appearing on the W grain boundary and the regular W surface were indicated by thick and hollow arrows, respectively. Two protruded ligament-like Os-Ru grains were marked by a dashed circle.

annealed Semicon film, as shown in Figure 9.1b. After annealing, uniformly dispersed cracks appeared over the film surface of the Semicon film. The cracks were up to 120 nm wide on the film surface, which allowed for some features in the crevice to be observed. Some ligament-like Os-Ru grains near the cracks were pulled out but still bridged cracks. In Figure 9.1b (indicated by a dashed-circle), two ligament-like Os-Ru grains are shown on the front fracture surface. The two protruding Os-Ru grains were located at approximately one-third and two-thirds of the film thickness from the W substrate with a diameter of 20-30 nm, and on the same order as the grain size. It is suggested that the protrusion in the Semicon film resulted from tensile stresses due to texture transition during annealing. Texture transition will be discussed later. In addition, the grain size did not grow significantly during annealing (25-55 nm for the as-deposited film and 25-75 nm for the annealed film).

By cross-sectional observation (shown in the bottom image of Figure 9.1b), it is noted that cracks might appear on either grain boundaries or W grain surfaces, marked by thick and hollow arrows in Figure 9.1b. All observed cracks on the grain boundaries of a W substrate extended through the film thickness and widely opened on the top surface of the film. Tensile stress in the annealed film was suggested as the primary cause for this type of cracking; in-plane stress leads to a higher momentum on the top surface than at the bottom of the film. The momentum can result in a crack extending through the film thickness with a wide gap on the film surface. However, some cracks on W grain surfaces were seen that did not extend through the film thickness but terminated at approximately two-thirds of the film thickness from the bottom, as indicated by a hollow arrow in Figure 9.1b. It is suggested that cracks of this type resulted from volume contraction of Os-Ru grains, caused by texture transition during annealing.

Microstructure of as-deposited and annealed UK-550nm, 300nm, and 150nm films are shown in Figures 9.2, 3, and 4, respectively, observed by plan-view (top) and cross-section (bottom) for each specimen. In these three figures, a pair of images for one specimen includes a micrograph for both the as-deposited film and the annealed film.

Figure 9.2 shows microstructural observation for UK-550nm films. All as-deposited UK-550nm films exhibit a grain structure consisting of columnar grains, similar to as-deposited Semicon films. Columnar grains were roughly perpendicular to the surface of the W substrate and extend through the film thickness as shown in Figures 9.2a, c, e, and g. The majority of grains in the as-deposited UK-550nm films ranged from 10 to 40 nm, except the UK-20W-550nm film which exhibited a larger grain size of 50-100 nm. The bias power applied during film deposition did not significantly affect grain size and columnar grain structure of the as-deposited UK-550nm films. In addition, the as-deposited UK-550nm films showed neither grain clustering nor gap-like cracking; phenomena seen in the as-deposited Semicon films despite the film thicknesses being close to the Semicon film thickness. All as-deposited UK-550nm films exhibited the same microstructure – fine columnar grains. However, these films present a different microstructure from the as-deposited films during annealing.

During annealing, the grain size in the UK-550nm films significantly increased from 10-40 nm (as-deposited) to 30-150 nm (annealed). The grain size of all Os-Ru films is shown in Table 9.2. The surface roughness of the UK-550nm films also increased with grain growth. Cross-sectional observation revealed that the columnar grain structure of the as-deposited films changed. A few grains in the UK-5W-550nm film transformed into shorter, columnar grains (almost equi-axed); but, most grains in the annealed

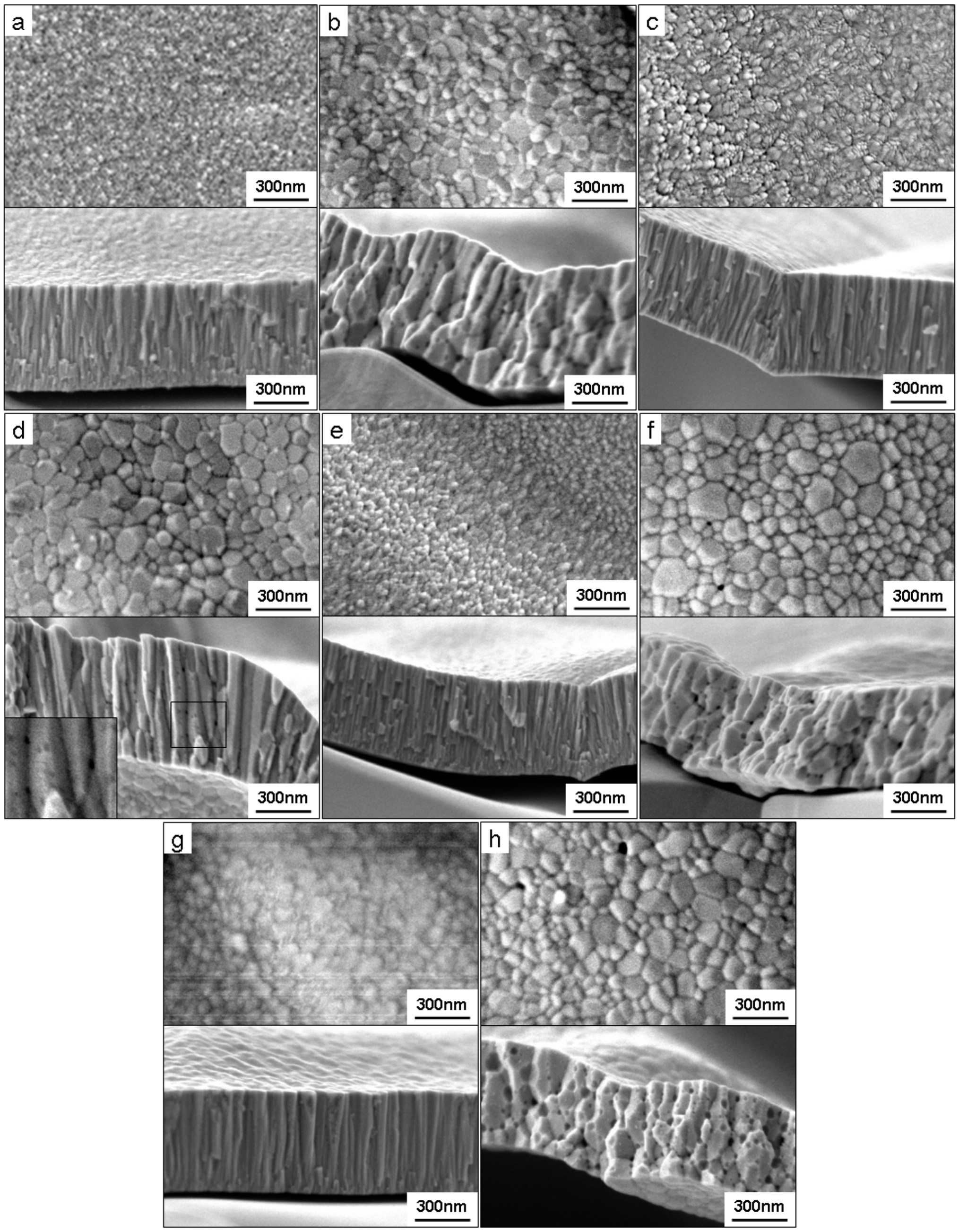

Figure 9.2 Micrographs of (a, c, e, and g) as-deposited and (b, d, f and h) annealed UK-550 nm films. Specimens of (a), (c), (e), and (g) were deposited with a biased power of 0, 5, 10, and 20 W, respectively. Images of (b), (d), (f), and (h) were taken sequentially corresponding to micrographs of (a), (c), (e), and (g). All as-deposited UK-550 nm films consist of columnar grains, but the columnar grains mostly transferred to equi-axed grains during annealing.

UK-5W-550nm film were still columnar and the grains extended through the film thickness. The UK-0W-550nm films consisted of both equi-axed and columnar grains with lengths shorter than the film thickness. In the UK-550nm films deposited with a bias power at 10 and 20 W, most grains in the annealed films transformed to equi-axed, and no columnar grains that extended through the film thickness were observed. All the grains in the annealed films were similar in that the grains grew three times as large in diameter and had facets. Furthermore, small voids appeared at grain boundaries of the annealed films as seen in the cross-sectional images of Figures 9.2b, d, f, and h. The voids were mostly as small as a few nm in diameter. Formation of the inter-granular voids will be discussed later.

The plan- and cross-sectional views of UK-300nm and UK-150nm films (in Figures 9.3 and 9.4) revealed microstructures similar to that of the UK-550nm films – with the exception of the UK-0W-300nm film. The columnar grains were roughly perpendicular to the surface of a W substrate and extend through the film thickness. The grain size in the as-deposited films ranged from 10-25 nm and 5-30 nm for UK-300nm films and UK-150nm films, respectively. It is seen in the as-deposited UK-300nm and UK-150nm films that the grain size decreased with increasing bias power. However, this tendency was not seen in the as-deposited UK-550nm films (see details in Table 9.2). It is suggested that applying bias during film deposition can introduce high compressive in-plane stresses in the as-deposited Os-Ru film, which leads to a higher nucleation density due to bombardment of Ar ions during deposition.

In-plane stress of the as-deposited UK-0W-550nm and UK-10W-150nm films was 5.77-6.49 GPa in compression, high enough to buckle the Os-Ru films in a telephone cord configuration due to the weak adhesion between the Os-Ru film and the substrate.

However, as-deposited Semicon films have a much lower compressive stress (~20 MPa) than the UK films [15, 16]. The high compressive stress in the UK as-deposited films might affect the film texture and grain structure.

During annealing, grains grew several times larger and in-plane compressive stresses were also released. The grain size of the annealed UK-300nm and UK-150nm films ranged from 30-120 nm, with UK-20W films showing some larger grains up to 150 nm. UK-300nm and UK-150nm films changed the columnar grain structure in the as-deposited films during annealing. Annealed UK-0W-300nm, UK-5W-300nm, and UK-20W-300nm films exhibited columnar grains that extended through the film thickness. Some shorter columnar grains appeared in UK-10W-300nm films with grain lengths smaller than the thickness of the film. Overall, the annealed UK-300nm and UK-150nm films presented a stronger preference for columnar (high aspect ratio) grains with the exception of the UK-10W-150nm film, which had completely equi-axed grains. Furthermore, small voids at the grain boundaries were also observed in all annealed UK-300nm and UK-150nm films. The voids can be as small as an order of several nm in some annealed films. The phenomenon of void formation was also seen in the annealed UK-550nm films, but not the annealed Semicon films.

During annealing, grains in the UK films transformed to completely equi-axed (e.g. UK-20W-550nm); part columnar, part equi-axed (e.g. UK-0W-550nm); or completely columnar (e.g. UK-5W-300nm) configuration. Small voids at the grain boundaries were observed in all annealed UK films, while the annealed Semicon films exhibited cracks instead of voids. Formation of voids is suggested to result from agglomeration of vacancies and Ar embedded in the growing of the Os-Ru film and/or Ar released by the porous W substrate. Manenschijn et al. [17] reported that Ar released by

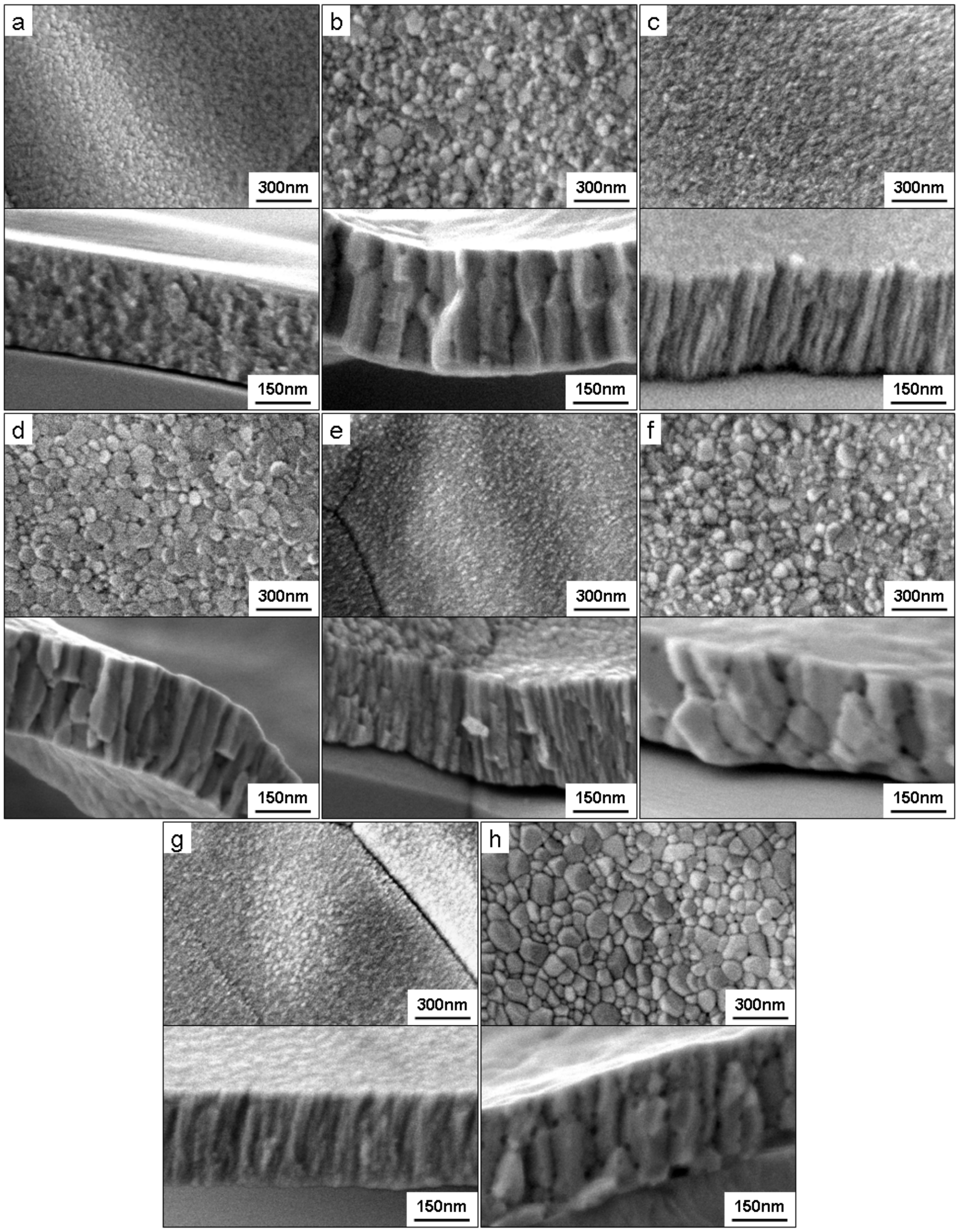

Figure 9.3 Micrographs of (a, c, e, and g) as-deposited and (b, d, f and h) annealed UK-300 nm films. Specimens of (a), (c), (e), and (g) were deposited with a biased power of 0, 5, 10, and 20 W, respectively. Images of (b), (d), (f), and (h) were taken sequentially corresponding to micrographs of (a), (c), (e), and (g). All as-deposited UK-300 nm films consist of columnar grains, except UK-0W-300 nm film. The columnar grains mostly transferred to equi-axed grains during annealing.

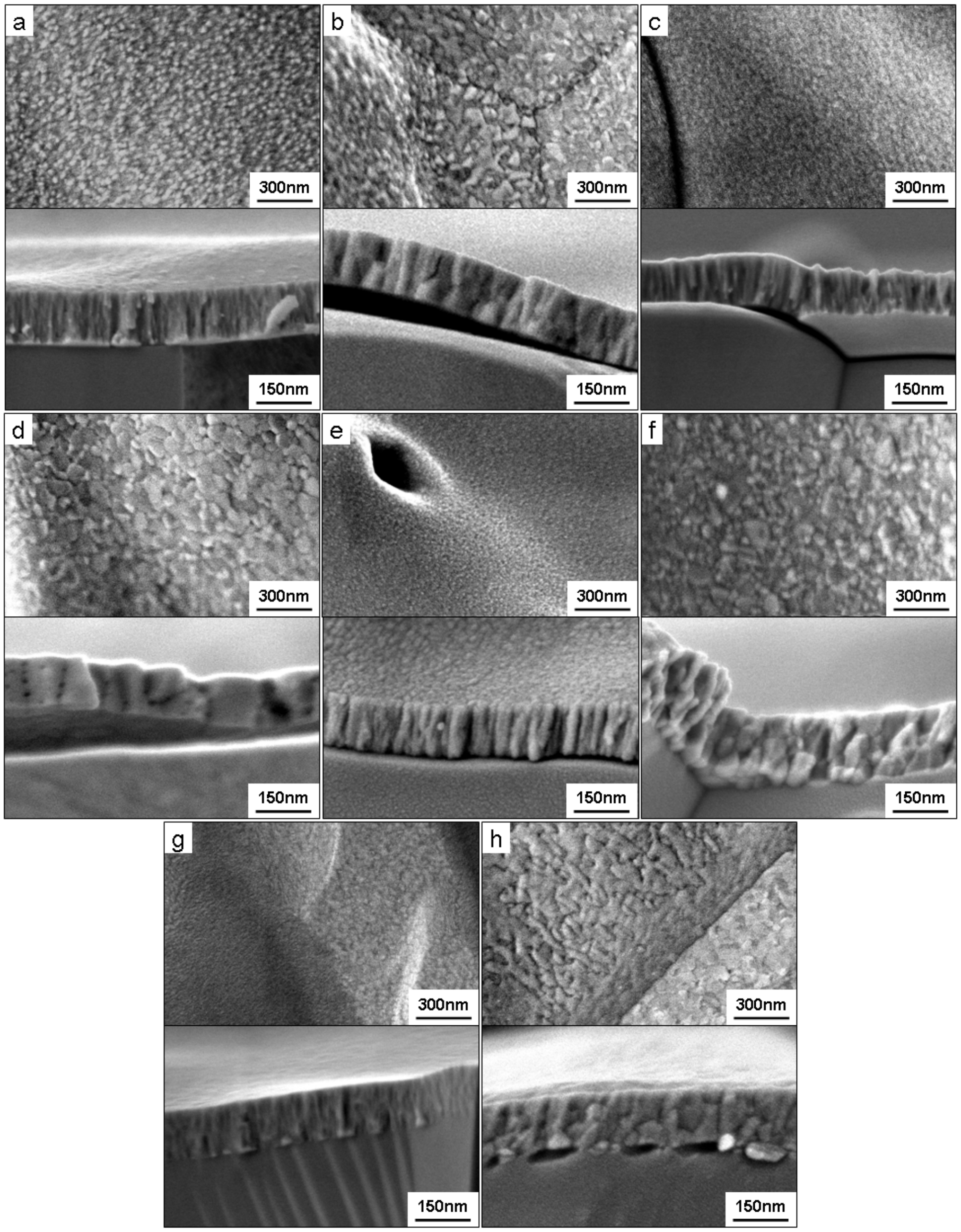

Figure 9.4 Micrographs of (a, c, e, and g) as-deposited and (b, d, f and h) annealed UK-150 nm films. Specimens of (a), (c), (e), and (g) were deposited with a biased power of 0, 5, 10, and 20 W, respectively. Images of (b), (d), (f), and (h) were taken sequentially corresponding to micrographs of (a), (c), (e), and (g). All as-deposited UK-150 nm films consist of columnar grains. The columnar grains mostly transferred to equi-axed grains during annealing.

Table 9.2 Grain size, void size, and grain structure of Semicon and UK Os-Ru films.

Specimen	As-deposited (nm)	Annealed (nm)	Void size (nm)	Grain structure after annealing*[3]
Semicon	20-65	25-100	----	equi-axed
UK-0W-550nm	10-15	30-120	10-15	col. + equi.
UK-5W-550nm	20-40*[1]	50-150	5-10	columnar
UK-10W-550nm	25-35	50-150	15-20	equi-axed
UK-20W-550nm	50-100	50-150	15-20	equi-axed
UK-0W-300nm	15-25	40-120	8-12	columnar
UK-5W-300nm	15-25	40-120	5-8	columnar
UK-10W-300nm	10-20	30-120	15-20	col. + equi.
UK-20W-300nm	10-20	40-120	15-20	col. + equi.
UK-0W-150nm	25-30	50-80	----	columnar
UK-5W-150nm	15-20	50-120	8-12	columnar
UK-10W-150nm	10-15	50-120	----	equi-axed
UK-20W-150nm	5-10	50-150*[2]	----	col. + equi.

*[1]: shell-like grains, shown in Figure 9.2c

*[2]: fused and irregular grains, shown in Figure 9.4h

*[3]: "col." – columnar; "equi." – equi-axed grains

the sputtered Os-Ru film (100 and 600 nm thick) and the W substrate occurred at 1100K and 1300K, respectively. Formation of Ar agglomerated bubbles was at temperatures higher than 1800K. The annealing temperature used in this study was 1050 ˚C$_{B}$ (or 1323K), which is too high for Ar to be released but lower than the temperature for Ar agglomeration via thermal-vacancy assisted diffusion (1800K). However, no results of microstructural characterization were mentioned by Manenschijn et al. Consequently, it is not clear if grain size and configuration of the as-deposited Os-Ru films can affect these temperatures.

Figure 9.5 shows voids formed in the annealed UK films with two typical grain structures, consisting of only columnar grains (UK-5W-300nm, shown in Figure 9.5a) or only equi-axed grains (UK-20W-550nm, shown in Figure 9.5b). Voids appeared in both types of grain structures and were at inter-granular sites in the Os-Ru film, such as grain boundaries and tri-junctions. It is seen that the grains formed facets during annealing. In the annealed UK-5W-300nm film, voids (dark spots in Figure 9.5a) linearly arranged along straight grain boundaries (e.g. 5 spots located between two arrows) or curved grain boundaries (ex. spots around the egg-like protruded grain, located at left of the bottom arrow) with diameters of 5-8 nm. Voids appearing in the annealed UK-20W-550nm film consisting of equi-axed grains were not distinguishable from the cave-rich fracture surface because some large caves resulted from pulling grains out during fracture. Some dark spots indentified as the voids were marked by arrows in Figure 9.5b. Voids in the film with a higher bias power and film thickness were 15-20 nm in diameter, which is 2-3 times larger than the voids that appeared in the annealed UK-5W-300nm film.

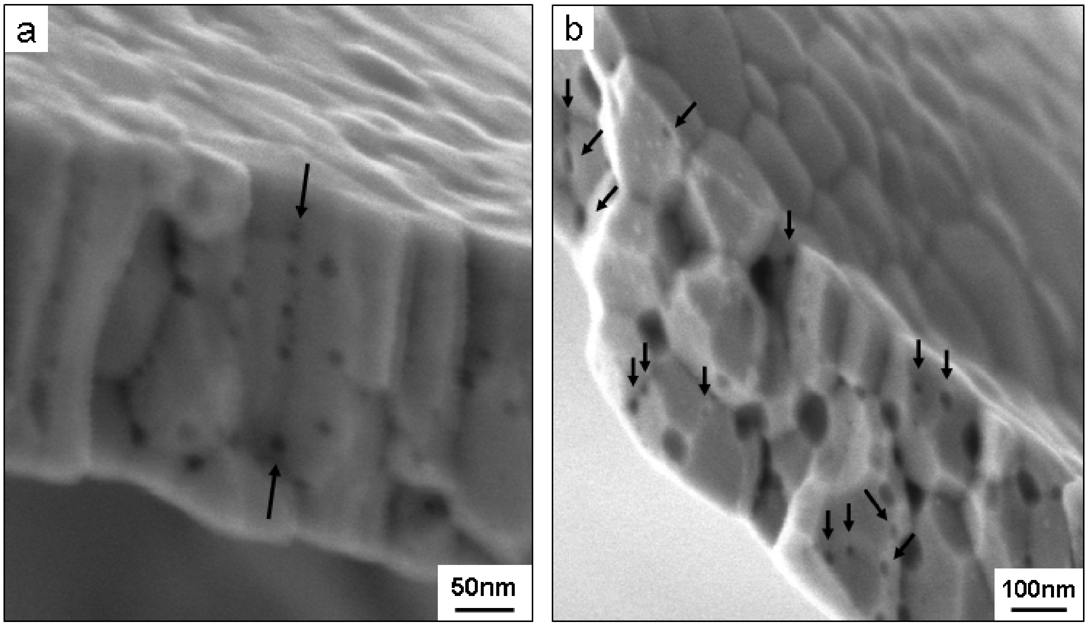

Figure 9.5 Voids formed at grain boundaries of the annealed (a) UK-5W-300nm and (b) UK-20W-550nm films. These two annealed films exhibit different grain structures: columnar grains in the UK-5W-300nm film and equi-axed grains in the UK-20W-550nm film.

Bias power did not seem to have a significant effect on void size. However, it was interesting that voids were always smaller when the annealed UK film consisted of columnar grains than when the film was a mixture of columnar/equi-axed grains or purely equi-axed grains. Detailed information about void size and grain structure are shown in Table 9.2. Since no reports have discussed the relationship between grain structure and Ar agglomeration in Os-Ru films during annealing or high-temperature operation, no proven mechanisms can be directly used to understand relationships between void size and grain structures. To interpret this unknown issue, it is suggested here that Ar agglomeration during annealing occurs by diffusion assisted by thermal vacancy motion.

Columnar grains have large and long facets on the grain sides parallel to the grain axis. The large and long grain boundaries are flat. A flat grain boundary has a uniform surface tension within a local area, but boundary curvature is the driving force to push vacancies moving once the temperature is high enough to make the vacancy motion proceed. That is, flat grain boundaries lack the driving force to push Ar desorbed by the Os-Ru film passing a long diffusion path for agglomeration. Therefore, many – but small – Ar bubbles form at the flat grain boundaries surrounding to a columnar grain. Contrastingly, equi-axed gains have a lower aspect ratio and a much more curved grain boundary which means a shorter diffusion path and a much higher driving force for Ar diffusion assisted by thermal vacancy motion. Figure 9.5 show that voids formed in the films consisting of equi-axed grains were larger and preferentially located at tri-junction points.

It is believed that the voids at grain boundaries can stabilize the grain structure and make difficulties in grain growth and/or Ostwalt ripening. Therefore, an understanding of void formation is very important for processing the Os-Ru coated dispenser diodes to improve their lifetime. Furthermore, grain structure is a critical factor for W diffusing into the Os-Ru film because grain boundaries can be circuit paths for W diffusion during high-temperature operation.

Texture is another critical factor affecting W diffusion behavior in an Os-Ru film. Texture components in HCP Os-Ru films contain {0002} basal, {10-10} prismatic, and {10-11} pyramidal planes. Basal planes have a higher planar packing density than prismatic and pyramidal planes. Considering W diffusion in an Os-Ru film by bulk diffusion paths, a high planar packing density might be helpful in inhibiting W/Os-Ru interdiffusion. In this study, textures of as-deposited and annealed Semicon and UK films were measured by XRD using the integrated intensity of each Os-Ru diffraction peak to calculate the amounts of individual texture components, as shown in Figure 9.6.

Figure 9.6a reveals that Semicon films had {10-10} prismatic and {10-11} pyramidal planes before annealing. However, the annealed Semicon film shows a strong {10-11} preference (0.93). As-deposited UK-550nm films have all three texture components: {0002}, {10-10}, and {10-11} planes. In the UK-550nm films deposited with a lower bias power (0 W or 5 W), {0002} basal planes are the majority of texture in these as-deposited films (0.69 for UK-0W-550nm and 0.75 for UK-5W-550nm). However, the fraction of basal planes decreased when bias power increased to 10 W or 20 W, and pyramidal planes became the texture majority in as-deposited UK-10W-550nm (0.43) and UK-20W-550nm (0.50) films. During annealing, the texture of the UK-550nm films changed significantly. 5 W and 20 W biased UK-550nm films presented a much stronger preference for basal planes. However, the fraction of basal planes in 0 W and 10 W biased UK films decreased during annealing. Instead, the annealed UK-0W-550nm and

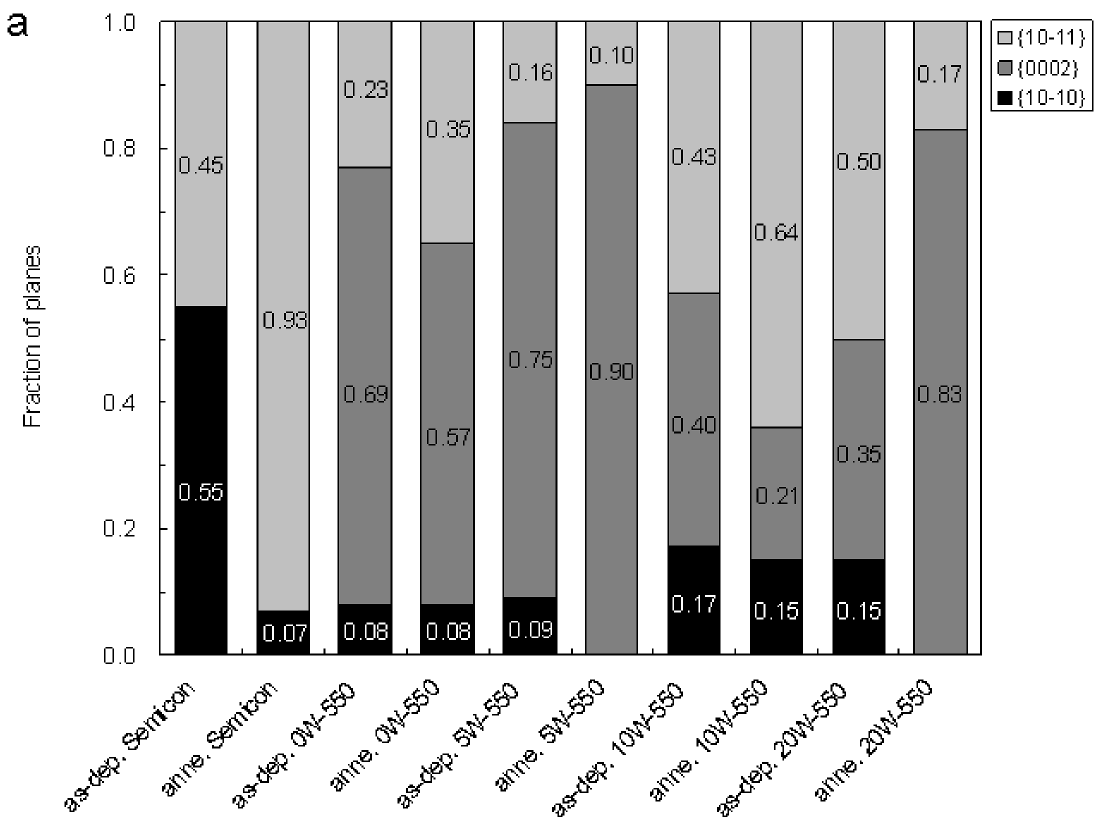
a
Fraction of planes
1.0
0.8
0.6
0.4
0.2
0.0
{10-11}
{0002}
{10-10}
0.45
0.55
0.93
0.07
0.23
0.69
0.08
0.35
0.57
0.08
0.16
0.75
0.09
0.10
0.90
0.43
0.40
0.17
0.64
0.21
0.15
0.50
0.35
0.15
0.17
0.83
as-dep. Semicon
anne. Semicon
as-dep. 0W-550
anne. 0W-550
as-dep. 5W-550
anne. 5W-550
as-dep. 10W-550
anne. 10W-550
as-dep. 20W-550
anne. 20W-550

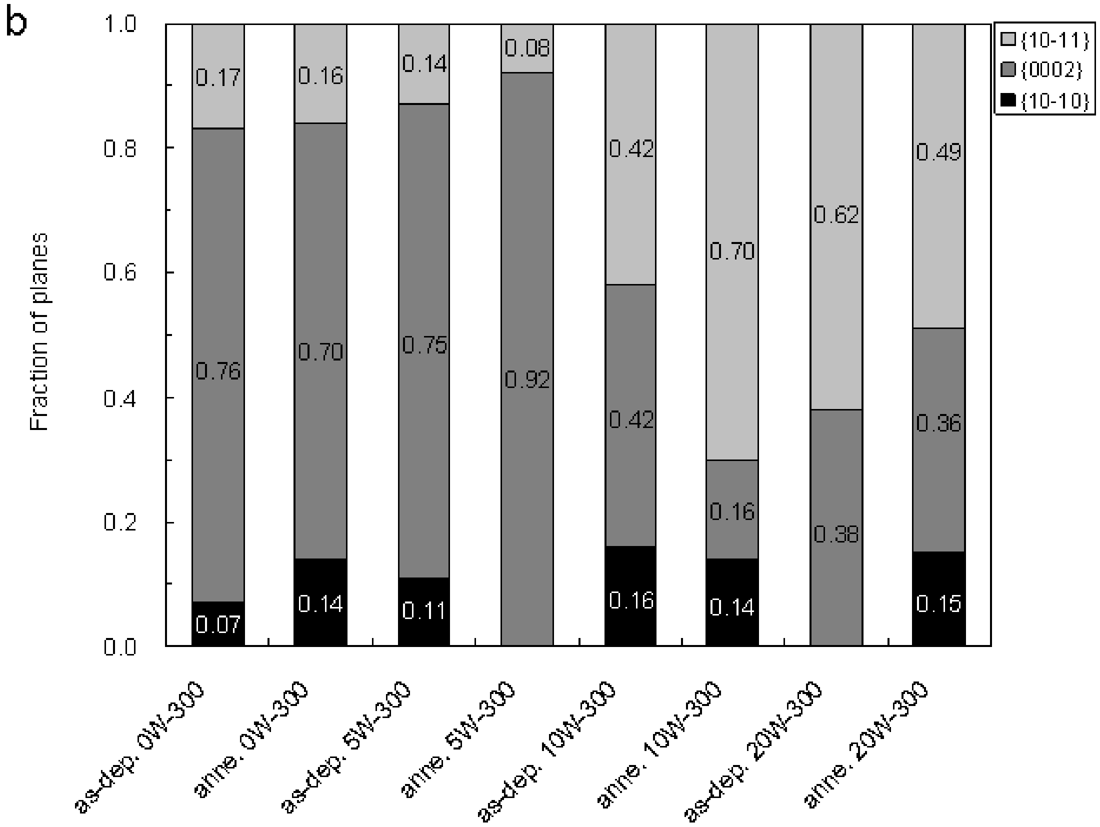
b
Fraction of planes
1.0
0.8
0.6
0.4
0.2
0.0
{10-11}
{0002}
{10-10}
0.17
0.76
0.07
0.16
0.70
0.14
0.14
0.75
0.11
0.08
0.92
0.42
0.42
0.16
0.70
0.16
0.14
0.62
0.38
0.49
0.36
0.15
as-dep. 0W-300
anne. 0W-300
as-dep. 5W-300
anne. 5W-300
as-dep. 10W-300
anne. 10W-300
as-dep. 20W-300
anne. 20W-300

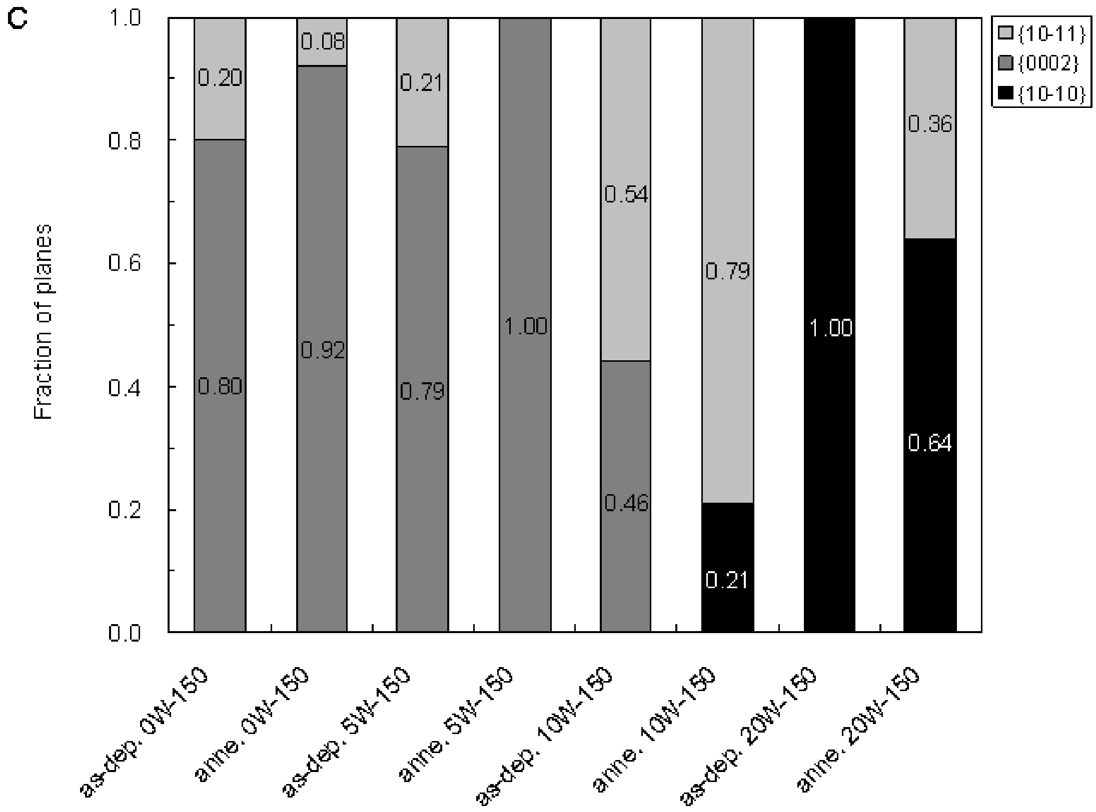

Figure 9.6 Changes in texture components in as-deposited and annealed (a) Semicon and UK-550nm, (b) UK-300nm, and (c) UK-150nm Os-Ru films.

UK-10W-550nm films exhibited a significant increase in the fraction of pyramidal planes (increased by 0.12 in UK-0W-550nm films and 0.21 in UK-10W-550nm films). The amount of prismatic planes in these two films remained the same or slightly decreased.

Texture in UK-300nm films are shown in Figure 9.6b. Similarly to UK-550nm films, all as-deposited UK-300nm films presented prismatic, basal and pyramidal planes, except UK-20W-300nm film showing basal and pyramidal planes only. In the as-deposited UK-300nm films deposited with a lower bias power (0 W or 5 W), basal plans were the majority of texture (0.76 for UK-0W-300nm films and 0.75 for UK-5W-300nm films). Increasing the bias power to 10 W and 20 W caused the fraction of basal planes in these as-deposited UK-300nm films to gradually decrease (0.42 for UK-10W-300nm and 0.38 for UK-20W-300nm films). This is similar to the texture change found in as-deposited UK-550nm films in that bias power of 10 W might be too high to have the basal component as the majority of film texture, and the texture majority was replaced by pyramidal planes. This phenomenon in as-deposited UK-300nm films can be clearly seen once bias power was increased to 20 W.

During annealing, texture change in the UK-300nm films matched with the UK-550nm films. Firstly, basal planes were still the majority of film texture in the UK-0W-300nm film despite decreasing slightly (decreased from 0.76 to 0.70). Secondly, the UK-5W-300nm film showed a stronger preference for basal planes than other UK-300nm films during annealing. Lastly, the fraction of basal planes in the UK-10W-300nm film decreased during annealing (from 0.42 to 0.16), and pyramidal planes became the texture majority (0.70). However, the UK-20W-300nm film exhibited different texture change from the UK-20W-550nm film during annealing. The basal planes retained a similar amount to the as-deposited film, but the prismatic planes appeared with a fraction of 0.15 and a 0.13 reduction of pyramidal planes.

Texture change in UK-150nm films was addressed in previous work prior to this study [13, 14]. In order to complete texture analysis of Os-Ru films with varing film thicknesses, the result of UK-150nm films was also involved in this study for a better and more systematic comparison. Texture of the as-deposited and annealed UK-150nm films is shown in Figure 9.6c. The as-deposited UK-150nm films processed with a lower bias power (0 W or 5 W) had basal planes as the majority of film texture (0.80 for UK-0W-150nm and 0.79 for UK-5W-150nm). However, the fraction of basal planes decreased to 0.46 and pyramidal planes became the texture majority when bias power increased to 10 W. Once bias power increased to 20 W, basal planes disappeared completely but the as-deposited UK-20W-150nm film exhibited prismatic planes only. Based on the fraction change in basal planes in the as-deposited UK-150nm films, there is a tendency similar to thicker UK films (i.e. UK-550nm and UK-300nm) in that basal planes were the majority of film texture in the as-deposited 0 W and 5 W biased films. However, the fraction of basal planes decreased with increasing bias power. In addition, the UK-0W-150nm and UK-5W-150nm films present a much stronger preference of basal planes during annealing. The annealed films have a higher fraction of basal planes (0.92 for the annealed UK-0W-150nm film and 1.00 for the annealed UK-5W-150nm film). However, basal planes disappeared in both the annealed UK-10W-150nm and UK-20W-150nm films. {10-11} pyramidal and {10-10} prismatic planes were the majority of film texture in the annealed UK-10W-150nm and UK-20W-150nm films, respectively.

Considering texture stability of Os-Ru films during annealing, the fraction of texture changes in the UK films are shown in Figure 9.7. The Fraction of texture changes in Semicon films was 0.48 (not shown in Figure 9.7), which was the highest value for all Os-Ru films presented in this study. Figure 9.7 shows the fraction of exhibited texture change of the films with a given film thickness (e.g. 150 nm, 300 nm, or 550 nm) increased with increasing bias power. However, the UK-20W-150nm and UK-20W-300nm films decreased their fractions of texture change. Note that a film having a smaller texture change was a more stable film texture during annealing (or high-temperature operation). In terms of film texture stability, Os-Ru films are suggested to be prepared with a lower film thickness and bias power.

In order to understand effects of deposition rate on film texture and texture

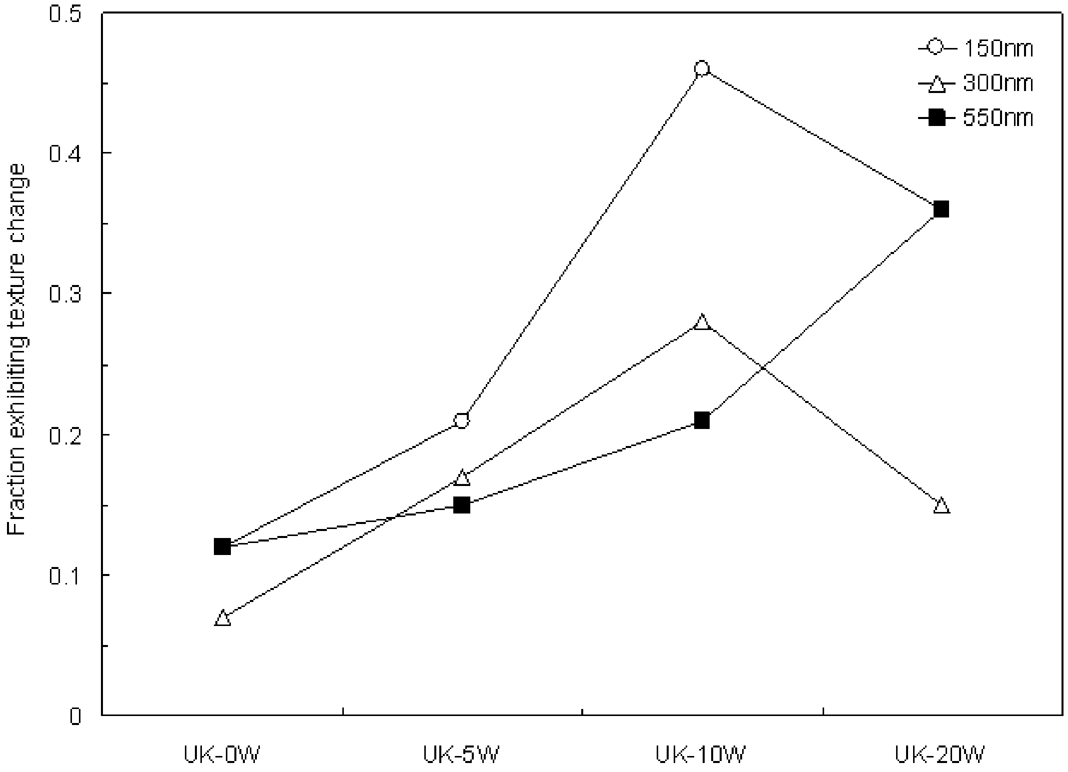

Figure 9.7 The plot shows the relationship between fraction exhibiting texture change during annealing and bias power of UK-150nm, UK-300nm, and UK-550nm films. With a given film thickness, fraction exhibiting texture change increased with the applied bias power increasing, except the UK-20W-150nm and UK-20W-300nm films. (Note: Fraction exhibiting texture change of Semicon films was 0.48, higher than all UK films.)

stability, two types of UK-20W-550nm films were deposited at different deposition rates: 17 nm/min (using the regular deposition rate shown in Table 9.1) and 8.5 nm/min (UK-20W-550nm). The deposition rate was change only by decreasing the deposition power by 50% with all other parameters remaining the same. The texture of the as-deposited UK-20W-550nm-slow film was 0.79 for basal planes and 0.21 for pyramidal planes. This texture is different from the regular as-deposited UK-20W-550nm film (0.15 for prismatic, 0.35 for basal and 0.50 for pyramidal components). However, it is interesting to note that the annealed UK-20W-550nm-slow film shows a film texture perfectly matching the annealed UK-20W-550nm film (0.83 for basal planes and 0.17 for pyramidal planes). Although the deposition rate affects the film texture during deposition, all films exhibited the same texture after annealing. In addition, the comparison of deposition rates shows that an Os-Ru film prepared at a lower deposition rate can have an as-deposited film texture much closer to the film texture of the annealed film. However, the UK-20W-550nm-slow film presented a fraction of exhibited texture change of only 0.03, which means the UK-20W-550nm-slow film had a very stable film texture during annealing.

As mentioned above, several issues involved with microstructure and texture can affect W/Os-Ru interdiffusion, such as grain size, inter-granular voids, and texture. The composition difference between the as-deposited and the annealed films provides a direct evaluation for W/Os-Ru interdiffusion. In this study, EDS was used to measure the composition of every specimen. Each specimen (either as-deposited or annealed) was measured from the top film surface, with the composition value taken as the average of three separate measurements. However, it is known that the EDS technique can collect elemental energy signals from the W substrate (Os-Ru films were only 150-610 nm thick). Therefore, the W signals were from not only the film but also the substrate. However, W content values obtained by EDS can be used to estimate W/Os-Ru interdiffusion.

Figure 9.8 shows the composition change of Semicon and UK films during annealing. The Semicon film has an increase in W content of 6 at.% with an equivalent reduction in Ru content. In UK-550nm films, the UK-5W-550nm film exhibited the lowest W content change (only 1 at.% change), shown in Figure 8a. In addition, UK-300nm films also showed that the films biased at 5 W had a lower W content change

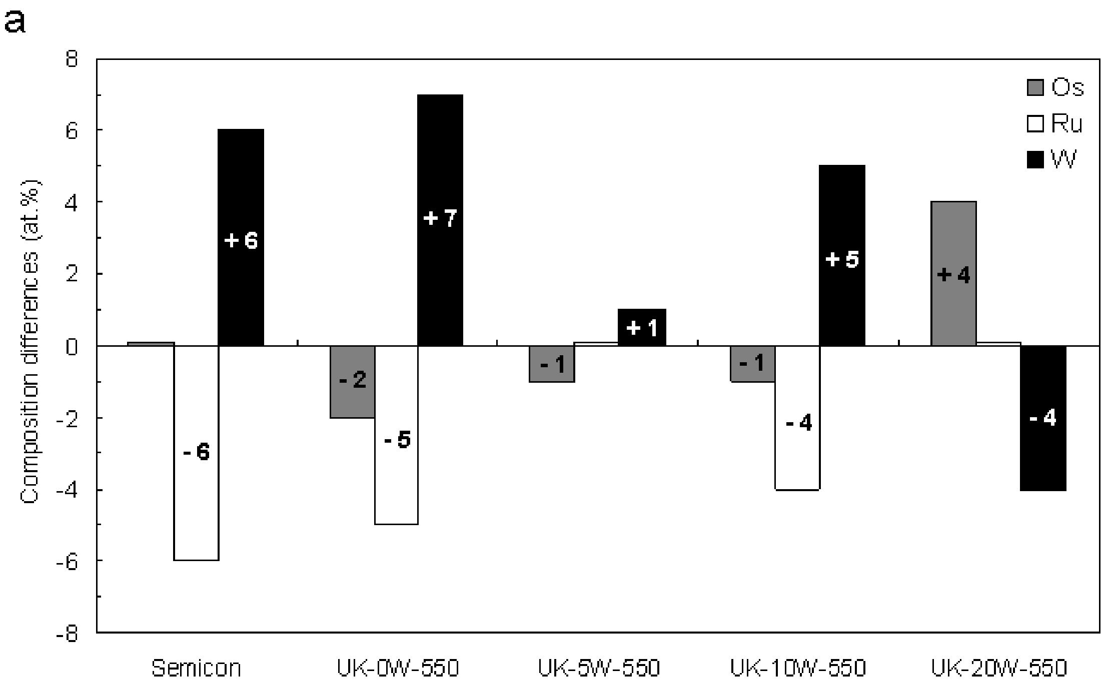
a
Composition differences (at.%)
8
6
4
2
0
-2
-4
-6
-8
Os
Ru
W
+6
-6
-2
+7
-5
-1
+1
-1
+5
-4
+4
-4
Semicon
UK-0W-550
UK-5W-550
UK-10W-550
UK-20W-550

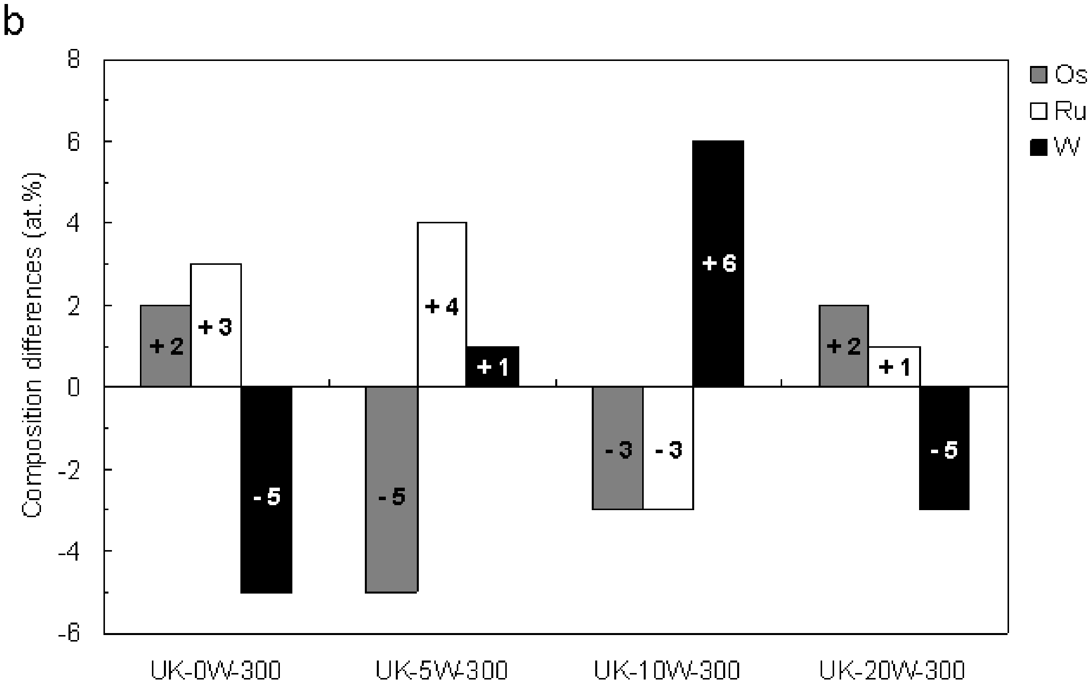
b
Composition differences (at.%)
8
6
4
2
0
-2
-4
-6
Os
Ru
W
+2
+3
-5
-5
+4
+1
-3
-3
+6
+2
+1
-5
UK-0W-300
UK-5W-300
UK-10W-300
UK-20W-300

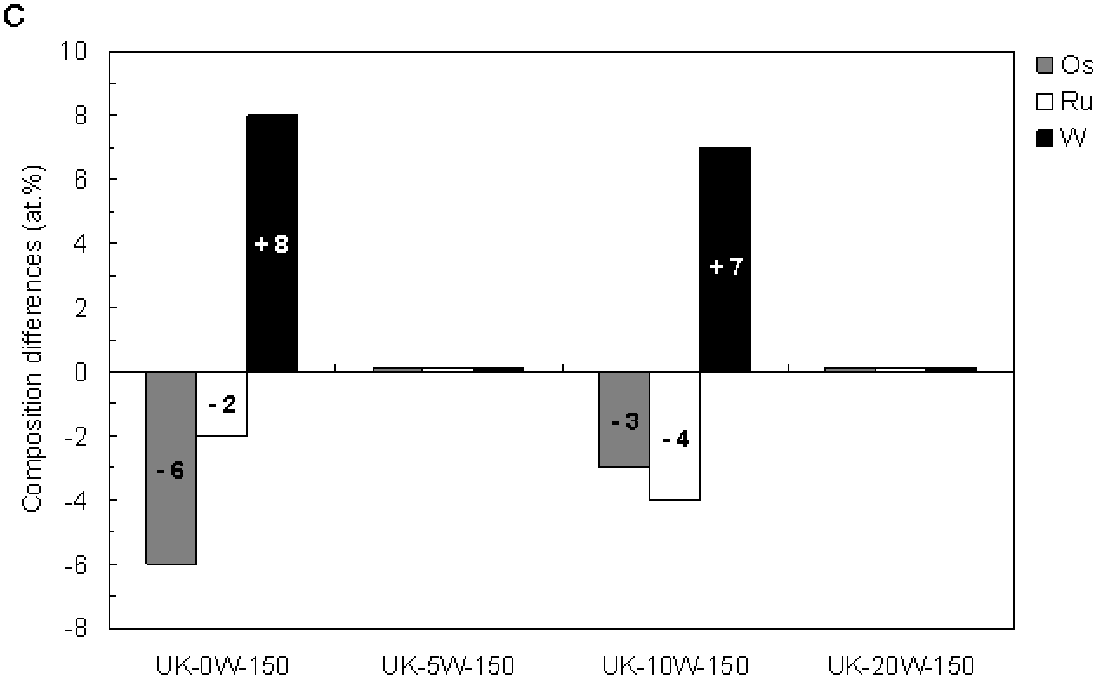

Figure 9.8 Composition change in (a) Semicon and UK-550nm, (b) UK-300nm, and (c) UK-150nm films during annealing. As the result, UK-5W films with all three film thicknesses show the highest stability of composition and the best ability to inhibit W diffusion into the Os-Ru film.

than other films (1 at.% change, shown in Figure 9.8b). For the thinnest UK films, both UK-5W-150nm and UK-20W-150nm films had no change in W content. Overall, based on composition analysis, UK-5W films (150 nm, 300 nm, and 550 nm) had the most stable compositions. Again, it should be emphasized that the EDS result shown in Figure 9.8 does not offer an accurate quantitative measurement. Exact amounts of composition change in the Os-Ru film need to be clarified using surface analysis techniques with depth profiling measurements, such as x-ray photoelectron spectroscopy or secondary ion mass spectrometry.

9.4 Summary

A complete and systematic result involving microstructural, texture, and composition analyses for the sputtered Os-Ru film coated on a porous W substrate was done in this study. Effects of film thicknesses and bias power were investigated, and results were compared with commercial specimens, provided by Semicon Associates Inc.

It was observed that columnar grains in the as-deposited Os-Ru films transformed into equi-axed grains during annealing in some specimens. UK-5W films (150 nm, 300 nm, and 550 nm) were the only set of specimens consisting of columnar grains before and after annealing. UK-0W and UK-5W films had the highest stability of film texture during annealing. Finally, UK-5W films also exhibited good stability of composition, which inhibited W/Os-Ru interdiffusion in these films during annealing.

It was shown that 5 W (115 V) was an ideal bias power for Os-Ru film deposition. In addition, lower film thicknesses and deposition rates were suggested for obtaining high stability of microstructure and film texture. With these suggested parameters (biased at 5 W, 150 nm thickness and 8.5 nm/min deposition rate), the lifetime of Os-Ru coated porous W dispenser cathodes should be improved.

Chapter 10

Conclusions

10.1 Concluding Remarks

This doctorate study focused on nanoporous Pd-based (np-Pd, np-PdNi and np-AuPd) and Os-Ru thin films. Np-AuPd thin films were used to study dealloying mechanisms and formation of nanoporosity in porous thin films. Np-Pd and np-PdNi thin films were utilized to investigate hydridation and dehydridation of the nanoporous Pd-based thin films. Additionally, relationships between deposition parameters and film texture/microstructure of Os-Ru were studied.

Microstructure of the Np-AuPd ultrathin film shows a ligament configuration of nanoporous structure, a layer of nanolegs and a layer of nanobridges, which has been commonly observed in nanoporous thin films (e.g. np-Au) but has never been reported and discussed. Formation of nanolegs was suggested due to low (or no) wetting in between the ligaments and the oxidized interlayer. Above the nanoleg layer, ligaments can be formed with random orientations. In addition, it is verified that the convex substrate has a higher dealloying rate in np-AuPd ultra thin films, yielding a nanoporous structure with more cracks and larger ligaments.

Based on understandings of dealloying mechanisms, np-pd and np-PdNi thin films were prepared with finer ligaments and pores by adding surfactants to the etchant solution. The fine porosity led to a much shorter response time of H absorption than blanket Pd films and np-Pd/np-PdNi films with coarse ligaments/pores. Hydridation behavior of the fine ligaments was addressed to involve formation and rearrangement of vacancies in Pd (or PdNi) lattices. Formation and rearrangement of vacancies can effectively relax the high compressive stress caused by hydridation and keep away from permanent deformation and delamination of np-Pd/np-PdNi thin films in a high H-content atmosphere.

Os-Ru thin films were deposited with varied sputtering parameters to change film texture and microstructure. Optimized deposition parameters were suggested to obtain the highest stability of film texture, microstructure and composition. Understandings of Os-Ru deposition may be helpful in improving lifetime and performance of the Os-Ru thin films used in dispenser cathodes.

10.2 Key Findings

10.2.1 Dealloying of Nanoporous Structure

Results from the studies of np-AuPd and np-Pd/np-PdNi thin films can be summarized as below:

- Characterization of np-AuPd on flat and curved substrates revealed differences in the dealloyed films. The np-AuPd film on a flat or curved substrate exhibited a transition in ligament geometry, cracking and film composition. The observed differences in dealloyed structure and composition may be due to a more tensile stress state in the convex region, which led to a faster Ag dissolution rate and earlier transition to ligament coarsening.
- AuPd clusters transformed from isolated nanodots to single-layer ligament networks and finally to a multilayer nanoporous film were observed in dealloying AuPdAg films. Change in morphology of AuPd clusters depended on thickness of AuPdAg precursor alloy films. It is noted that a critical

thickness of the AuPdAg film has to be required for formation of a 3-D nanoporous structure.

- The bottommost layer of a nanoporous film consisted of individual "nanolegs", oriented perpendicular to the substrate, which supported nanobridges as the second layer in the porous structure above. It is proposed that nanoleg formation was enhanced by oxidation of the Ta interlayer over most of the substrate area, except at locations of incipient AuPd agglomeration where bonds with metallic Ta were established.
- Average ligament width and pore diameter in dealloyed np-PdNi films were decreased by ~50% after adding surfactants to the etching solution. It is proposed that the refinement of nanoporosity is due to partial immobilization of Pd adatoms, which hinders surface diffusion along ligaments. In addition, ultrasonic agitation was found to accelerate the dealloying process while maintaining fine nanoporosity. These np-PdNi films with smaller pores may be well suited for applications that require higher amounts of surface area, such as hydrogen sensing.

10.2.2 Hydridation and Dehydridation Behavior

Results from the study of hydridation and dehydridation of np-Pd/np-PdNi thin films can be summarized as below:

- During hydridation, compressive stresses caused by H absorption can be relaxed to an equilibrated stress level. The stress relaxation involved two mechanisms: (1) formation of vacancies and (2) rearrangement of vacancies in Pd (or PdNi) ligaments. The high compressive stress was firstly and rapidly relaxed by formation of vacancies in the first few min during hydridation. The next stage of stress relaxation was dominated by rearrangement of vacancies, and the vacancy rearrangement can relax film stress to an equilibrated level.

- Thicker np-Pd/np-PdNi films contained a higher amount of remnant Ni after dealloying. Due to a much longer dealloying time needed for thicker films, porosity through the entire film thickness might be not as uniform as the thinner films. Difference in remnant Ni content and porosity may change H absorption and desorption behavior. In addition, remnant Ni might change local stress fields of Pd(Ni) lattices due to its smaller atomic radius. The changed stress field might vary the amount of vacancies which were formed during the 1st stage of stress relaxation.

10.2.3 Characterization of Os-Ru Films

Results from the study of Os-Ru thin films can be summarized as below:

- Columnar grains in the as-deposited Os-Ru films transformed into equi-axed grains during annealing in some specimens. UK-5W films (150 nm, 300 nm, and 550 nm) were the only set of specimens consisting of columnar grains before and after annealing. UK-0W and UK-5W films had the highest stability of film texture during annealing. Finally, UK-5W films also exhibited good stability of composition, which inhibited W/Os-Ru interdiffusion in these films during annealing.
- 5 W (115 V) was an ideal bias power for Os-Ru film deposition. Lower film thicknesses and deposition rates were suggested for obtaining high stability of microstructure and film texture. With these suggested parameters (biased at 5

W, 150 nm thickness and 8.5 nm/min deposition rate), the lifetime of Os-Ru coated porous W dispenser cathodes should be improved.

10.3 Future Work

Based on results of the doctorate study, some ideas were generated for clarifying unknown questions/mechanisms. The ideas might be able to estimate possibility of using the materials for potential applications. In this section, the ideas will be presented.

10.3.1 Nanoporous Thin Films

- Precursor alloy films can be deposited with a multilayer structure, containing interrupted columnar grains in the as-deposited film and oriented ligaments in the dealloyed porous film. Nanoporous Pd-based alloy films with oriented ligaments might be able for membrane applications, which require oriented porosity. Additionally, composition of each layer of the precursor alloy can be tuned for obtaining optimal porosity gradient from film top to film bottom of the final porous structure.
- Porosity dimensions of the nanoporous Pd-based alloy films dealloyed with surfactants might be changed by adding surfactants with varied length of C-chains to the etching solution. Therefore, finer nanoporosity (2 nm or less) might be able to achieve by using surfactants with shorter C-chains. The porous Pd-based alloy films with a finer porosity might exhibit better performance for H_2 sensing applications, especially response time.
- Np-Pd/np-PdNi thin film might be a good electrode material in proton exchange membrane fuel cells (PEMFCs) when the nanoporous layer is

prepared on a continuous thick Pd film. Due to high absorption rate and low capability of H in the np-Pd/np-PdNi films, the nanoporous layer might be helpful in rapidly "trapping" H from the atmosphere.

- Sensitivity of np-Pd/np-PdNi thin films to H absorption and desorption can be measured in an atmosphere containing low H_2 content, e.g. levels of ppm. High surface-to-volume ratio of the nanoporous Pd-based alloy thin films might be still sensitive in the low-H atmosphere. It is suggested that np-Pd/np-PdNi thin films can be cycled in the low-H atmosphere to determine limits of H_2 content for H_2 sensing.
- Ag nanoprecipitates-decorated np-Au thin films may be able for applications as a catalytic material for bacteria adhesion, which has been recently verified by few studies of Ag-decorated Au nanoparticles. The Ag-decorated np-Au films can be prepared by combination of dealloying and electroplating. During electroplating, Ag nanoprecipitates might be grown epitaxially due to its well-matched lattice parameters to Au. Surface Plasmon of the np-Au thin films might appear based on the periodic air/Au/air (i.e. dielectric/metal/dielectric) structure. Furthermore, surface-enhanced Raman scattering (SERS) of the np-Au thin film might be improved by decoration of the Ag nanoprecipitates.

10.3.2 Os-Ru Films

- Os-Ru films can be deposited as a sandwich structure. The bottommost layer can be composed of fine grains, which can improve adhesion to the W substrate. The 2nd layer contains coarse grains to interrupt W diffusion along grain boundaries. The topmost layer is composed of fine grains with a sharp tip on the grain top, which might lower work function of the coating material and improve emission capability. The improvement might lead the cathodes to operate for a longer lifetime.

- In general, elements have high electron emission efficiency once the elements present their electronic configuration with a ground term of sp^0, such as magnesium, calcium and barium. These elements are usually used in phosphors at oxidation states. Based on electronic configuration of Pd, it is suggested that work function of the Os-Ru film might be lowered by doping little amount of Pd on the film surface because Pd has a ground term of sp^0. The lowered work function may improve emission capability and lifetime of the cathodes.

References

Chapter 1: Introduction

[1] Barton JC, Woodward I, Lewis FA. Hysteresis of Relationships between Electrical Resistance and Hydrogen Content of Palladium. T Faraday Soc 1963;59:1201.

[2] Pundt A, Kirchheim R. Hydrogen in Metals: Microstructural Aspects. Annual Review of Materials Research 2006;36:555.

[3] Oriani RA. The Physical and Metallurgical Aspects of Hydrogen in Metals. 4th International Conference on Cold Fusion. Lahaina, 1993.

[4] Schlecht U, Balasubramanian K, Burghard M, Kern K. Electrochemically Decorated Carbon nanotubes for Hydrogen Sensing. Appl Surf Sci 2007;253:8394.

[5] Rather SU, Zacharia R, Hwang SW, Naik MU, Nahm KS. Hyperstoichiometric Hydrogen Storage in Monodispersed Palladium Nanoparticles. Chem Phys Lett 2007;438:78.

[6] Chen ZH, Jie JS, Luo LB, Wang H, Lee CS, Lee ST. Applications of Silicon Nanowires Functionalized with Palladium Nanoparticles in Hydrogen Sensors. Nanotechnology 2007;18.

[7] Eastman JA, Thompson LJ, Kestel BJ. Narrowing of the Palladium-hydrogen Miscibility Gap in Nanocrystalline Palladium. Phys Rev B 1993;48:84.

[8] Kuji T, Matsumura Y, Uchida H, Aizawa T. Hydrogen Absorption of Nanocrystalline Palladium. Journal of Alloys and Compounds 2002;330:718.

[9] Lemier C, Weissmuller J. Grain Boundary Segregation, Stress and Stretch: Effects on Hydrogen Absorption in Nanocrystalline Palladium. Acta Mater 2007;55:1241.

[10] Luna-Moreno D, Monzon-Hernandez D, Villatoro J, Badenes G. Optical Fiber Hydrogen Sensor Based on Core Diameter Mismatch and Annealed Pd-Au Thin Films. Sensor Actuat B-Chem 2007;125:66.

[11] Luna-Moreno D, Monzon-Hernandez D. Effect of the Pd-Au Thin Film Thickness Uniformity on the Performance of An Optical Fiber Hydrogen Sensor. Appl Surf Sci 2007;253:8615.

[12] Di Vece M, Grandjean D, Van Bael MJ, Romero CP, Wang X, Decoster S, Vantomme A, Lievens P. Hydrogen-induced Ostwald Ripening at Room Temperature in A Pd Nanocluster Film. Physical Review Letters 2008;100.

[13] Ding DY, Chen Z, Lu C. Hydrogen Sensing of Nanoporous Palladium Films Supported by Anodic Aluminum Oxides. Sensor Actuat B-Chem 2006;120:182.

[14] Ding DY, Chen Z. Volume-expansion-enhanced pinning of nanoporous Pd films for detection of high-concentration hydrogen. Sens Lett 2006;4:331.

[15] Ding DY, Chen Z. A pyrolytic, carbon-stabilized, nanoporous Pd film for wide-range H-2 sensing. Adv Mater 2007;19:1996.

[16] Erlebacher J. An atomistic description of dealloying - Porosity evolution, the critical potential, and rate-limiting behavior. J Electrochem Soc 2004;151:C614.

[17] Forty AJ. Corrosion Micro-Morphology of Noble-Metal Alloys and Depletion Gilding. Nature 1979;282:597.

[18] Erlebacher J, Aziz MJ, Karma A, Dimitrov N, Sieradzki K. Evolution of Nanoporosity in Dealloying. Nature 2001;410:450.

[19] Ji CX, Searson PC. Fabrication of Nanoporous Gold Nanowires. Applied Physics Letters 2002;81:4437.

[20] Kramer D, Viswanath RN, Weissmuller J. Surface-stress Induced Macroscopic Bending of Nanoporous Gold Cantilevers. Nano Lett 2004;4:793.

[21] Sun Y, Kucera KP, Burger SA, Balk TJ. Microstructure, stability and thermomechanical behavior of crack-free thin films of nanoporous gold. Scripta Materialia 2008;58:1018.

[22] Kabius B, Kaiser H, Kaesche H. A Micromorphological Study of Selective Dissolution of Cu from CuPd-Alloys. J Electrochem Soc 1986;133:C304.

[23] Li W-C, Balk TJ. Preparation and Hydrogen Absorption/Desorption of Nanoporous Palladium Thin Films. Materials (submitted) 2009.

[24] Hayes JR, Hodge AM, Biener J, Hamza AV, Sieradzki K. Monolithic Nanoporous Copper by Dealloying Mn-Cu. J Mater Res 2006;21:2611.

[25] Sun L, Chien CL, Searson PC. Fabrication of Nanoporous Nickel by Electrochemical Dealloying. Chemistry of Materials 2004;16:3125.

[26] Kimura S, Higuchi T, Ouchi Y, Ueda E, Nakamura O, Sudo T, Koyama K. Emission Characteristics of Dispenser Cathodes with A Fine-grained Tungsten Top Layer. Appl Surf Sci 1997;111:60.

[27] Roquais JM, Poret F, le Doze R, Ricaud JL, Monterrin A, Steinbrunn A. Barium Depletion Study on Impregnated Cathodes and Lifetime Prediction. Appl Surf Sci 2003;215:5.

[28] Bao JX, Wan BF, Wang PJ. Preparation and Performance Analysis of Barium Dispenser Cathodes. Vacuum 2007;81:1029.

[29] Kumar KS, Devi PD, Ravi M, Bhat KS. Work Function Distribution for W-Ir Mixed Metal Matrix Cathodes. Appl Surf Sci 2006;252:5632.

[30] Cortenraad R, van der Gon AWD, Brongersma HH, Gartner G, Manenschijn A.

Surface Analysis of Thermionic Dispenser Cathodes. Appl Surf Sci 2002;191:153.

[31] Higuchi T, Nakamura O, Matsumoto S, Uda E. Pore Geometry of Dispenser Cathode Surface vs. Emission Characteristics, and Ba Recovery Characteristics After Ion Bombardment. Appl Surf Sci 1999;146:51.

[32] Falce LR. A Study of the Inter-diffusion of Tungsten and Osmium-ruthenium in M-cathodes and the Effects on Performance and Life. Fifth IEEE International Vacuum Electronics Conference. Palo Alto, CA, USA, 2004. p.356.

[33] Private Communication with Semicon Associates.

[34] Jones D, Mcneely D, Swanson LW. Surface and Emission Characterization of the Impregnated Dispenser Cathode. Appl Surf Sci 1979;2:232.

[35] Rachocki KD, Lamartine BC, Haas TW. Angle Resolved Photoelectron-Spectroscopy Study of M-Type Cathode Activation. Appl Surf Sci 1983;16:40.

[36] Koenig MF, Grant JT. XPS Studies of the Chemical-State of Ba on the Surface of Impregnated Tungsten Dispenser Cathodes. Appl Surf Sci 1985;20:481.

[37] Forman R. Surface Studies on the Low Work Function Surface Complex of Barium on an Osmium Ruthenium Substrate. Appl Surf Sci 1987;29:127.

[38] Vanveen NJA. XPS on Impregnated Cathodes - Surface Concentrations and Thermal-Stability. Appl Surf Sci 1987;29:113.

[39] Bell BV. Bias Sputter Deposition of Osmium-Ruthenium Films. Dept. Chem. Mater. Eng. Lexington, KY: Univ. Kentucky, 1994.

[40] Isagawa S, Higuchi T, Kobayashi K, Miyake S, Ohya K, Yoshida M. Application of M-type Cathodes to High-power Cw Klystrons. Appl Surf Sci 1999;146:89.

Chapter 2: Background

[1] Kabius B, Kaiser H, Kaesche H. A Micromorphological Study of Selective Dissolution of Cu from CuPd-Alloys. J Electrochem Soc 1986;133:C304.

[2] Moreira J, del Angel P, Ocampo AL, Sebastian PJ, Montoya JA, Castellanos RH. Synthesis, Characterization and Application of A Pd/Vulcan and Pd/C Catalyst in A PEM Fuel Cell. Int J Hydrogen Energ 2004;29:915.

[3] Cho YH, Choi B, Cho YH, Park HS, Sung YE. Pd-based PdPt(19 : 1)/C Electro-catalyst as An eElectrode in PEM Fuel Cell. Electrochem Commun 2007;9:378.

[4] Garcia AC, Paganin VA, Ticianelli EA. CO Tolerance of PdPt/C and PdPtRu/C Anodes for PEMFC. Electrochim Acta 2008;53:4309.

[5] Biyikoglu A. Review of Proton Exchange Membrane Fuel Cell Models. Int J Hydrogen Energ 2005;30:1181.

[6] Erdler G, Frank M, Lehmann M, Reinecke H, Muller C. Chip Integrated Fuel Cell. Sensors and Actuators a-Physical 2006;132:331.

[7] Favier F, Walter EC, Zach MP, Benter T, Penner RM. Hydrogen Sensors and Switches from Electrodeposited Palladium Mesowire Arrays. Science 2001; 293: 2227.

[8] Walter EC, Favier F, Penner RM. Palladium Mesowire Arrays for Fast Hydrogen Sensors and Hydrogen-actuated Switches. Anal Chem 2002;74:1546.

[9] Villatoro J, Monzon-Hernandez D. Fast Detection of Hydrogen with Nano Fiber Tapers Coated with Ultra Thin Palladium Layers. Opt Express 2005;13:5087.

[10] Lim W, Wright JS, Gila BP, Johnson JL, Ural A, Anderson T, Ren F, Pearton SJ. Room Temperature Hydrogen Detection Using Pd-coated GaN Nanowires. Applied Physics Letters 2008;93:0721091.

[11] Mubeen S, Zhang T, Yoo B, Deshusses MA, Myung NV. Palladium Nanoparticles Decorated Single-walled Carbon Nanotube Hydrogen Sensor. J Phys Chem C 2007; 111:6321.

[12] Baselt DR, Fruhberger B, Klaassen E, Cemalovic S, Britton CL, Patel SV, Mlsna TE, McCorkle D, Warmack B. Design and Performance of A Microcantilever-based Hydrogen Sensor. Sensor Actuat B-Chem 2003;88:120.

[13] Ding DY, Chen Z, Lu C. Hydrogen Sensing of Nanoporous Palladium Films Supported by Anodic Aluminum Oxides. Sensor Actuat B-Chem 2006;120:182.

[14] Ding DY, Chen Z. A pyrolytic, carbon-stabilized, nanoporous Pd film for wide-range H-2 sensing. Adv Mater 2007;19:1996.

[15] Ding DY, Chen Z. Volume-expansion-enhanced pinning of nanoporous Pd films for detection of high-concentration hydrogen. Sens Lett 2006;4:331.

[16] Luongo K, Sine AR, Bhansali S. Development of A Highly Sensitive Porous Si-based Hydrogen Sensor Using Pd Nano-structures. Sensor Actuat B-Chem 2005; 111:125.

[17] Forty AJ. Corrosion Micro-Morphology of Noble-Metal Alloys and Depletion Gilding. Nature 1979;282:597.

[18] Erlebacher J, Aziz MJ, Karma A, Dimitrov N, Sieradzki K. Evolution of Nanoporosity in Dealloying. Nature 2001;410:450.

[19] Biener J, Hodge AM, Hamza AV. Microscopic Failure Behavior of Nanoporous Gold. Applied Physics Letters 2005;87.

[20] Biener J, Hodge AM, Hamza AV, Hsiung LM, Satcher JH. Nanoporous Au: A High Yield Strength Material. J Appl Phys 2005;97.

[21] Biener J, Hodge AM, Hayes JR, Volkert CA, Zepeda-Ruiz LA, Hamza AV, Abraham

FF. Size Effects on The Mechanical Behavior of Nanoporous Au. Nano Lett 2006; 6: 2379.

[22] Parida S, Kramer D, Volkert CA, Rosner H, Erlebacher J, Weissmuller J. Volume Change during The Formation of Nanoporous Gold by Dealloying. Physical Review Letters 2006;97.

[23] Volkert CA, Lilleodden ET, Kramer D, Weissmuller J. Approaching The Theoretical Strength in Nanoporous Au. Applied Physics Letters 2006;89.

[24] Senior NA, Newman RC. Synthesis of Tough Nanoporous Metals by Controlled Electrolytic Dealloying. Nanotechnology 2006;17:2311.

[25] Zhu JZ, Seker E, Bart-Smith H, Begley MR, Kelly RG, Zangari G, Lye WK, Reed ML. Mitigation of Tensile Failure in Released Nanoporous Metal Microstructures via Thermal Treatment. Applied Physics Letters 2006;89.

[26] Hakamada M, Mabuchi M. Mechanical Strength of Nanoporous Gold Fabricated by Dealloying. Scripta Materialia 2007;56:1003.

[27] Lu X, Balk TJ, Spolenak R, Arzt E. Dealloying of Au-Ag Thin films with A Composition Gradient: Influence on Morphology of Nanoporous Au. Thin Solid Films 2007;515:7122.

[28] Lu X, Bischoff E, Spolenak R, Balk TJ. Investigation of Dealloying in Au-Ag Thin Films by Quantitative Electron Probe Microanalysis. Scripta Materialia 2007;56:557.

[29] Sun Y, Balk TJ. Evolution of Structure, Composition, and Stress in Nanoporous Gold Thin Films with Grain-boundary Cracks. Metall Mater Trans A 2008;39A:2656.

[30] Sun L, Chien CL, Searson PC. Fabrication of Nanoporous Nickel by Electrochemical Dealloying. Chemistry of Materials 2004;16:3125.

[31] Erlebacher J. An Atomistic Description of Dealloying - Porosity Evolution, The Critical Potential, and Rate-limiting Behavior. J Electrochem Soc 2004;151:C614.

[32] Andreasen G, Nazzarro M, Ramirez J, Salvarezza RC, Arvia AJ. Kinetics of Particle Coarsening at Gold Electrode/electrolyte Solution Interfaces Followed by In Situ Scanning Tunneling Microscopy. J Electrochem Soc 1996;143:466.

[33] Qian LH, Chen MW. Ultrafine Nanoporous Gold by Low-temperature Dealloying and Kinetics of Nanopore Formation. Applied Physics Letters 2007;91.

[34] Dona JM, Gonzalez-Velasco J. Mechanism of Surface-Diffusion of Gold Adatoms in Contact with an Electrolytic Solution. J Phys Chem-Us 1993;97:4714.

[35] Erlebacher J, Sieradzki K. Pattern Formation during Dealloying. Scripta Materialia 2003;49:991.

[36] Sieradzki K. Curvature Effects in Alloy Dissolution. J Electrochem Soc 1993; 140: 2868.

[37] Sieradzki K, Corderman RR, Shukla K, Newman RC. Computer-simulations of Corrosion - Selective Dissolution of Binary-Alloys. Philos Mag A 1989;59:713.

[38] Sun Y, Balk TJ. A Multi-step Dealloying Method to Produce Nanoporous Gold with No Volume Change and Minimal Cracking. Scripta Materialia 2008;58:727.

[39] Centrone A, Brambilla L, Zerbi G. Adsorption of H-2 on Carbon-based Materials: A Raman Spectroscopy Study. Phys Rev B 2005;71.

[40] Mitsui T, Rose MK, Fomin E, Ogletree DF, Salmeron M. Dissociative Hydrogen Adsorption on Palladium Requires Aggregates of Three or More Vacancies. Nature 2003;422:705.

[41] Lopez N, Lodziana Z, Illas F, Salmeron M. When Langmuir Is Too Simple: H2 Dissociation on Pd(111) at High Coverage. Physical Review Letters 2004; 93: 1461031.

[42] Berube V, Radtke G, Dresselhaus M, Chen G. Size Effects on the Hydrogen Storage Properties of Nanostructured Metal Hydrides: A review. International Journal of Energy Research 2007;31:637.

[43] Frieske H, Wicke E. Magnetic Susceptibility and Equilibrium Diagram of PdH. Ber Bunsen Phys Chem 1973;77:48.

[44] Flanagan TR, Kuji T, Oates WA. The Effect of Isotopic-Substitution on the Alpha-Alpha' Phase-Transition in Metal Hydrogen Systems. J Phys F Met Phys 1985; 15:2273.

[45] Flanagan TB, Oates WA. The Palladium-Hydrogen System. Annu Rev Mater Sci 1991;21:269.

[46] Krenn CR. Continuum Modelling of Transformation Hysteresis in A Metal Hydride System. Model Simul Mater Sc 2004;12:S415.

[47] Lasser R, Klatt K-H. Solubility of Hydrogen Isotopes in Palladium. Phys Rev B 1983; 28:748.

[48] Schirber JE, Morosin B. Lattice-Constants of Beta-PdHx and Beta-PdDx with X near 1.0. Phys Rev B 1975;12:117.

[49] Pundt A, Kirchheim R. Hydrogen in Metals: Microstructural Aspects. Annual Review of Materials Research 2006;36:555.

[50] Nechaev YS. Characteristics of Hydride-like Segregates of Hydrogen at Dislocations in Palladium. Physics - Uspekhi 2001;44:1189.

[51] Lemier C, Weissmuller J. Grain Boundary Segregation, Stress and Stretch: Effects on Hydrogen Absorption in Nanocrystalline Palladium. Acta Mater 2007;55:1241.

[52] Mutschele T, Kirchheim R. Segregation and Diffusion of Hydrogen in Grain-Boundaries of Palladium. Scripta Metall Mater 1987;21:135.

[53] Oriani RA. The Physical and Metallurgical Aspects of Hydrogen in Metals. 4th International Conference on Cold Fusion. Lahaina, 1993.

[54] Kirchheim R. Interaction of Hydrogen with Dislocations in Palladium .1. Activity and Diffusivity and Their Phenomenological Interpretation. Acta Metall Mater 1981; 29:835.

[55] Kirchheim R. Interaction of Hydrogen with Dislocations in Palladium .2. Interpretation of Activity Results by a Fermi-Dirac Distribution. Acta Metall Mater 1981;29:845.

[56] Pundt A. Hydrogen in Nano-sized Metals. Advanced Engineering Materials 2004; 6: 11.

[57] Eastman JA, Thompson LJ, Kestel BJ. Narrowing of The Palladium-hydrogen Miscibility Gap in Nanocrystalline Palladium. Phys Rev B 1993;48:84.

[58] Kuji T, Uchida H, Sato M, Cui W. Thermodynamic Properties of Hydrogen in Fine Pd Powders. Journal of Alloys and Compounds 1999;293-295:19.

[59] Kuji T, Matsumura Y, Uchida H, Aizawa T. Hydrogen Absorption of Nanocrystalline Palladium. Journal of Alloys and Compounds 2002;330:718.

[60] Kishore S, Nelson JA, Adair JH, Eklund PC. Hydrogen Storage in Spherical and Platelet Palladium Nanoparticles. Journal of Alloys and Compounds 2005;389:234.

[61] Sachs C, Pundt A, Kirchheim R, Winter M, Reetz MT, Fritsch D. Solubility of Hydrogen in Single-sized Palladium Clusters. Phys Rev B 2001;64.

[62] Jurczyk M, Okonska I, Iwasieczko W, Jankowska E, Drulis H. Thermodynamic and Electrochemical Properties of Nanocrystalline Mg2Cu-type Hydrogen Storage Materials. Journal of Alloys and Compounds 2007;429:316.

[63] Cox DM, Fayet P, Brickman R, Hahn MY, Kaldor A. Abnormally Large Deuterium Uptake on Small Transition Metal Clusters. Catalysis Letters 1990;4:271.

[64] Asakuma Y, Miyauchi S, Yamamoto T, Aoki H, Miura T. Numerical Analysis of Absorbing and Desorbing Mechanism for The Metal Hydride by Homogenization Method. Int J Hydrogen Energ 2003;28:529.

[65] Crespo EA, Ruda M, de Debiaggi SR. Hydrogen Absorption in Ni and Pd: A Study Based on Atomistic Calculations. Int J Hydrogen Energ 2008;33:3561.

[66] Seymour EFW, Cotts RM, Williams WD. NMR Measurement of Hydrogen Diffusion in Beta-Palladium Hydride. Physical Review Letters 1975;35:165.

[67] Di Vece M, Grandjean D, Van Bael MJ, Romero CP, Wang X, Decoster S, Vantomme A, Lievens P. Hydrogen-induced Ostwald Ripening at Room Temperature in A Pd Nanocluster Film. Physical Review Letters 2008;100.

[68] Zalm P, Johannes A, Stratum Av, Peeters HH. Tungsten Dispenser Cathode Having

Emission Enhancing Coating of Osmium-iridium or Osmium-Ruthenium Alloy for Use in Electron Tube. US Patent No. 3,497,757, Philips, 1970.

[69] Falce LR. Electron Tube with Dispenser Cathode. US Patent No. 4,165,473, Varian Associates, Inc., 1979.

[70] Cortenraad R, van der Gon AWD, Brongersma HH, Gartner G, Manenschijn A. Surface Analysis of Thermionic Dispenser Cathodes. Appl Surf Sci 2002;191:153.

[71] Senzaki Y, Gladfelter WL, Mccormick FB. Chemical-Vapor-Deposition of Ruthenium and Osmium Thin-Films Using (Hexafluoro-2-Butyne) Tetracarbonylruthenium and Tetracarbonylosmium. Chemistry of Materials 1993; 5: 1715.

[72] Chi Y, Yu HL, Ching WL, Liu CS, Chen YL, Chou TY, Peng SM, Lee GH. Deposition of Osmium Thin Films Using Pyrazolate Complexes as CVD Source Reagents. J Mater Chem 2002;12:1363.

[73] Roquais JM, Poret F, le Doze R, Ricaud JL, Monterrin A, Steinbrunn A. Barium Depletion Study on Impregnated Cathodes and Lifetime Prediction. Appl Surf Sci 2003;215:5.

[74] Higuchi T, Nakamura O, Matsumoto S, Uda E. Pore Geometry of Dispenser Cathode Surface vs. Emission Characteristics, and Ba Recovery Characteristics After Ion Bombardment. Appl Surf Sci 1999;146:51.

[75] Private Communication with Semicon Associates.

[76] Jones D, Mcneely D, Swanson LW. Surface and Emission Characterization of the Impregnated Dispenser Cathode. Appl Surf Sci 1979;2:232.

[77] Isagawa S, Higuchi T, Kobayashi K, Miyake S, Ohya K, Yoshida M. Application of M-type Cathodes to High-power Cw Klystrons. Appl Surf Sci 1999;146:89.

[78] Rachocki KD, Lamartine BC, Haas TW. Angle Resolved Photoelectron-Spectroscopy Study of M-Type Cathode Activation. Appl Surf Sci 1983;16:40.

[79] Koenig MF, Grant JT. XPS Studies of the Chemical-State of Ba on the Surface of Impregnated Tungsten Dispenser Cathodes. Appl Surf Sci 1985;20:481.

[80] Vanveen NJA. XPS on Impregnated Cathodes - Surface Concentrations and Thermal-Stability. Appl Surf Sci 1987;29:113.

[81] Forman R. Surface Studies on the Low Work Function Surface Complex of Barium on an Osmium Ruthenium Substrate. Appl Surf Sci 1987;29:127.

[82] Bell BV. Bias Sputter Deposition of Osmium-Ruthenium Films. Dept. Chem. Mater. Eng. Lexington, KY: Univ. Kentucky, 1994.

Chapter 3: Experiments

[1] Nix WD. Mechanical-Properties of Thin-Films. Metall Trans A 1989;20:2217.

[2] Cullity BD, Stock SR. Elements of X-Ray Diffraction. Upper Saddle River, NJ: Prentice Hall, 2001.

Chapter 4: Preparation and Hydrogen Sensing Behavior of Np-Pd Thin Films

[1] Flanagan TB, Oates WA. The Palladium-Hydrogen System. Ann Rev Mater Sci 1991;21:269.

[2] Sachs C, Pundt A, Kirchheim R, Winter M, Reetz MT, Fritsch D. Solubility of Hydrogen in Single-sized Palladium Clusters. Phys Rev B 2001;64.

[3] Rather SU, Zacharia R, Hwang SW, Naik MU, Nahm KS. Hyperstoichiometric hydrogen storage in monodispersed palladium nanoparticles. Chem Phys Lett 2007;438:78.

[4] Schlecht U, Balasubramanian K, Burghard M, Kern K. Electrochemically decorated carbon nanotubes for hydrogen sensing. Appl Surf Sci 2007;253:8394.

[5] Chen ZH, Jie JS, Luo LB, Wang H, Lee CS, Lee ST. Applications of silicon nanowires functionalized with palladium nanoparticles in hydrogen sensors. Nanotechnology 2007;18:3455021.

[6] Luna-Moreno D, Monzon-Hernandez D, Villatoro J, Badenes G. Optical fiber hydrogen sensor based on core diameter mismatch and annealed Pd-Au thin films. Sensor Actuat B-Chem 2007;125:66.

[7] Luna-Moreno D, Monzon-Hernandez D. Effect of the Pd-Au thin film thickness uniformity on the performance of an optical fiber hydrogen sensor. Appl Surf Sci 2007;253:8615.

[8] Ding DY, Chen Z, Lu C. Hydrogen sensing of nanoporous palladium films supported by anodic aluminum oxides. Sensor Actuat B-Chem 2006;120:182.

[9] Erlebacher J, Aziz MJ, Karma A, Dimitrov N, Sieradzki K. Evolution of nanoporosity in dealloying. Nature 2001;410:450.

[10] Lu X, Bischoff E, Spolenak R, Balk TJ. Investigation of dealloying in Au-Ag thin films by quantitative electron probe microanalysis. Scripta Mater 2007;56:557.

[11] Lu X, Balk TJ, Spolenak R, Arzt E. Dealloying of Au-Ag thin films with a composition gradient: Influence on morphology of nanoporous Au. Thin Solid Films 2007;515:7122.

[12] Erlebacher J, Sieradzki K. Pattern formation during dealloying. Scripta Mater 2003;

49:991.
[13] Erlebacher J. An atomistic description of dealloying - Porosity evolution, the critical potential, and rate-limiting behavior. J Electrochem Soc 2004;151:C614.
[14] Kabius B, Kaiser H, Kaesche H. A Micromorphological Study of Selective Dissolution of Cu from Cupd-Alloys. J Electrochem Soc 1986;133:562.
[15] Hakamada M, Mabuchi M. Preparation of Nanoporous Palladium by Dealloying: Anodic Polarization Behaviors of Pd-M (M = Fe, Co, Ni) Alloys. Mater. Trans. 2009; 50:431.
[16] Sun L, Chien CL, Searson PC. Fabrication of nanoporous nickel by electrochemical dealloying. Chem Mater 2004;16:3125.
[17] Sun Y, Balk TJ. Evolution of structure, composition, and stress in nanoporous gold thin films with grain-boundary cracks. Metall Mater Trans A 2008;39A:2656.
[18] Parida S, Kramer D, Volkert CA, Rosner H, Erlebacher J, Weissmuller J. Volume change during the formation of nanoporous gold by dealloying. Phys Rev Lett 2006;97:0355041.
[19] Sun Y, Kucera KP, Burger SA, Balk TJ. Microstructure, stability and thermo-mechanical behavior of crack-free thin films of nanoporous gold. Scripta Mater 2008;58:1018.
[20] Schirber JE, Morosin B. Lattice-Constants of Beta-PdHx and Beta-PdDx with X near 1.0. Phys Rev B 1975;12:117.
[21] Krenn CR. Continuum Modelling of Transformation Hysteresis in A Metal Hydride System. Model Simul Mater Sc 2004;12:S415.
[22] Berube V, Radtke G, Dresselhaus M, Chen G. Size Effects on the Hydrogen Storage Properties of Nanostructured Metal Hydrides: A review. Int J Energy Res 2007; 31: 637.

Chapter 5: Achieving Finer Pores and Ligaments in Np-PdNi Thin Films

[1] Erlebacher J. An atomistic description of dealloying - Porosity evolution, the critical potential, and rate-limiting behavior. J Electrochem Soc 2004;151:C614.
[2] Erlebacher J, Aziz MJ, Karma A, Dimitrov N, Sieradzki K. Evolution of nano-porosity in dealloying. Nature 2001;410:450.
[3] Sun Y, Balk TJ. Evolution of structure, composition, and stress in nanoporous gold thin films with grain-boundary cracks. Metallurgical and Materials Transactions 2008;39A:2656.
[4] Erlebacher J, Sieradzki K. Pattern formation during dealloying. Scripta Mater

2003;49:991.

[5] Berube V, Radtke G, Dresselhaus M, Chen G. Size Effects on the Hydrogen Storage Properties of Nanostructured Metal Hydrides: A review. Int J Energy Res 2007; 31: 637.

[6] Schlecht U, Balasubramanian K, Burghard M, Kern K. Electrochemically decorated carbon nanotubes for hydrogen sensing. Appl Surf Sci 2007;253:8394.

[7] Chen ZH, Jie JS, Luo LB, Wang H, Lee CS, Lee ST. Applications of silicon nanowires functionalized with palladium nanoparticles in hydrogen sensors. Nanotechnology 2007;18.

[8] Luna-Moreno D, Monzon-Hernandez D, Villatoro J, Badenes G. Optical fiber hydrogen sensor based on core diameter mismatch and annealed Pd-Au thin films. Sensor Actuat B-Chem 2007;125:66.

[9] Luna-Moreno D, Monzon-Hernandez D. Effect of the Pd-Au thin film thickness uniformity on the performance of an optical fiber hydrogen sensor. Appl Surf Sci 2007;253:8615.

[10] Kabius B, Kaiser H, Kaesche H. A Micromorphological Study of Selective Dissolution of Cu from Cupd-Alloys. J Electrochem Soc 1986;133:C304.

[11] Li W-C, Schendel SC, Balk TJ. Microstructure and Hydrogen Absorption/Desorption Behavior of Nanoporous Pd Thin Films. In: al. Ce, editor. Mater. Res. Soc. Symp. Proc., vol. 1098. Warrendale, PA: Mater. Res. Soc. Symp. Proc., 2008. p.HH02.08.

[12] Li W-C, Balk TJ. Preparation and Hydrogen Absorption/Desorption of Nanoporous Palladium Thin Films. submitted to Materials 2009.

[13] Chen M, Nikles DE, Yin HQ, Wang ST, Harrell JW, Majetich SA. Patterning self-assembled FePt nanoparticles. J Magn Magn Mater 2003;266:8.

[14] Chen M, Nikles DE. Synthesis of spherical FePd and CoPt nanoparticles. J Appl Phys 2002;91:8477.

[15] Ma HY, Chen SH, Yin BS, Zhao SY, Liu XQ. Impedance spectroscopic study of corrosion inhibition of copper by surfactants in the acidic solutions. Corros Sci 2003;45:867.

[16] Ma HY, Chen SH, Zhao SY, Liu XQ, Li DG. A study of corrosion behavior of copper in acidic solutions containing cetyltrimethylammonium bromide. J Electrochem Soc 2001;148:B482.

[17] Luo H, Guan YC, Han KN. Inhibition of mild steel corrosion by sodium dodecyl benzene sulfonate and sodium oleate in acidic solutions. Corrosion 1998;54:619.

[18] Fernandez MB, Tonetto GM, Crapiste GH, Ferreira ML, Damiani DE. Hydrogenation of edible oil over Pd catalysts: A combined theoretical and

experimental study. Journal of Molecular Catalysis A: Chemical 2005;237:67.

[19] Parida S, Kramer D, Volkert CA, Rosner H, Erlebacher J, Weissmuller J. Volume change during the formation of nanoporous gold by dealloying. Physical Review Letters 2006;97:035504.

Chapter 6: Effects of Substrate Curvature on Dealloying of Nanoporous Thin Films

[1] Forty AJ. Corrosion Micro-Morphology of Noble-Metal Alloys and Depletion Gilding. Nature 1979;282:597.

[2] Forty AJ, Durkin P. A micromorphological study of the dissolution of silver-gold alloys in nitric acid. Philos. Mag. A, Phys. Condens. Matter Defects Mech. Prop. 1980;42:295.

[3] Erlebacher J, Aziz MJ, Karma A, Dimitrov N, Sieradzki K. Evolution of nanoporosity in dealloying. Nature 2001;410:450.

[4] Ji CX, Searson PC. Fabrication of nanoporous gold nanowires. Appl Phys Lett 2002; 81:4437.

[5] Kabius B, Kaiser H, Kaesche H. A Micromorphological Study of Selective Dissolution of Cu from CuPd-Alloys. J Electrochem Soc 1986;133:C304.

[6] Li W-C, Schendel SC, Balk TJ. Microstructure and Hydrogen Absorption/Desorption Behavior of Nanoporous Pd Thin Films. In: al. Ce, editor. Mater. Res. Soc. Symp. Proc., vol. 1098. Warrendale, PA: Mater. Res. Soc. Symp. Proc., 2008. p.HH02.08.

[7] Hayes JR, Hodge AM, Biener J, Hamza AV, Sieradzki K. Monolithic nanoporous copper by dealloying Mn-Cu. J Mater Res 2006;21:2611.

[8] Sun L, Chien CL, Searson PC. Fabrication of nanoporous nickel by electrochemical dealloying. Chem Mater 2004;16:3125.

[9] Anselme K, Bigerelle M. Effect of a gold-palladium coating on the long-term adhesion of human osteoblasts on biocompatible metallic materials. Surf Coat Tech 2006;200:6325.

[10] Maeland A, Flanagan TB. X-Ray and Thermodynamic Studies of Absorption of Hydrogen by Gold-Palladium Alloys. J Phys Chem-Us 1965;69:3575.

[11] Huang XMH, Manolidis M, Jun SC, Hone J. Nanomechanical hydrogen sensing. Appl Phys Lett 2005;86.

[12] Luna-Moreno D, Monzon-Hernandez D, Villatoro J, Badenes G. Optical fiber hydrogen sensor based on core diameter mismatch and annealed Pd-Au thin films. Sensor Actuat B-Chem 2007;125:66.

[13] Luna-Moreno D, Monzon-Hernandez D. Effect of the Pd-Au thin film thickness

uniformity on the performance of an optical fiber hydrogen sensor. Appl Surf Sci 2007;253:8615.

[14] Chen MS, Kumar D, Yi CW, Goodman DW. The promotional effect of gold in catalysis by palladium-gold. Science 2005;310:291.

[15] Hou WB, Dehm NA, Scott RWJ. Alcohol oxidations in aqueous solutions using Au, Pd, and bimetallic AuPd nanoparticle catalysts. J Catal 2008;253:22.

[16] Qian LH, Chen MW. Ultrafine nanoporous gold by low-temperature dealloying and kinetics of nanopore formation. Appl Phys Lett 2007;91:0831051.

[17] Sun Y, Kucera KP, Burger SA, Balk TJ. Microstructure, stability and thermo-mechanical behavior of crack-free thin films of nanoporous gold. Scripta Materialia 2008;58:1018.

[18] Lu X, Balk TJ, Spolenak R, Arzt E. Dealloying of Au-Ag thin films with a composition gradient: Influence on morphology of nanoporous Au. Thin Solid Films 2007;515:7122.

[19] Sun Y, Balk TJ. Evolution of structure, composition, and stress in nanoporous gold thin films with grain-boundary cracks. Metallurgical and Materials Transactions 2008;39A:2656.

[20] Li W-C, Balk TJ. Transition from Single- to Multi-layered Structures in Nanoporous Gold-Palladium Ultrathin Films. submitted to Materials 2009.

[21] Erlebacher J, Sieradzki K. Pattern formation during dealloying. Scripta Materialia 2003;49:991.

[22] Erlebacher J. An atomistic description of dealloying porosity evolution, the critical potential, and rate-limiting behavior. Journal of the Electrochemical Society 2004;151:614.

[23] Schofield EJ, Ingham B, Turnbull A, Toney MF, Ryan MP. Strain development in nanoporous metallic foils formed by dealloying. Appl Phys Lett 2008;92:0431181.

Chapter 7: Transition from Single- to Multi-layered Structures in Np-AuPd Ultrathin Films

[1] Forty AJ. Corrosion Micro-Morphology of Noble-Metal Alloys and Depletion Gilding. Nature 1979;282:597.

[2] Ji CX, Searson PC. Fabrication of nanoporous gold nanowires. Appl Phys Lett 2002; 81:4437.

[3] Kramer D, Nadar Viswanath R, Weissmuller J. Surface-stress induced macroscopic bending of nanoporous gold cantilevers. Nano Letters 2004;4:793.

[4] Biener J, Hodge AM, Hayes JR, Volkert CA, Zepeda-Ruiz LA, Hamza AV, Abraham FF. Size effects on the mechanical behavior of nanoporous Au. Nano Letters 2006; 6: 2379.

[5] Kabius B, Kaiser H, Kaesche H. A Micromorphological Study of Selective Dissolution of Cu from CuPd-Alloys. J Electrochem Soc 1986;133:C304.

[6] Li W-C, Schendel SC, Balk TJ. Preparation and Hydrogen Absorption/Desorption of Nanoporous Palladium Thin Films. Materials Research Society Symposium Proceedings, vol. 1098 (HH02-08). v. 1098, 2008.

[7] Hayes JR, Hodge AM, Biener J, Hamza AV, Sieradzki K. Monolithic nanoporous copper by dealloying Mn-Cu. J Mater Res 2006;21:2611.

[8] Sun L, Chien CL, Searson PC. Fabrication of nanoporous nickel by electrochemical dealloying. Chem Mater 2004;16:3125.

[9] Erlebacher J, Aziz MJ, Karma A, Dimitrov N, Sieradzki K. Evolution of nanoporosity in dealloying. Nature 2001;410:450.

[10] Erlebacher J, Sieradzki K. Pattern formation during dealloying. Scripta Mater 2003; 49:991.

[11] Ding Y, Chen M, Erlebacher J. Metallic mesoporous nanocomposites for electrocatalysis. Journal of the American Chemical Society 2004;126:6876.

[12] Sun Y, Kucera KP, Burger SA, Balk TJ. Microstructure, stability and thermomechanical behavior of crack-free thin films of nanoporous gold. Scripta Materialia 2008;58:1018.

[13] Sun Y, Balk TJ. A multi-step dealloying method to produce nanoporous gold with no volume change and minimal cracking. Scripta Materialia 2008;58:727.

[14] Anselme K, Bigerelle M. Effect of a gold-palladium coating on the long-term adhesion of human osteoblasts on biocompatible metallic materials. Surf Coat Tech 2006;200:6325.

[15] Maeland A, Flanagan TB. X-Ray and Thermodynamic Studies of Absorption of Hydrogen by Gold-Palladium Alloys. J Phys Chem-Us 1965;69:3575.

[16] Huang XMH, Manolidis M, Jun SC, Hone J. Nanomechanical hydrogen sensing. Appl Phys Lett 2005;86.

[17] Luna-Moreno D, Monzon-Hernandez D, Villatoro J, Badenes G. Optical fiber hydrogen sensor based on core diameter mismatch and annealed Pd-Au thin films. Sensor Actuat B-Chem 2007;125:66.

[18] Luna-Moreno D, Monzon-Hernandez D. Effect of the Pd-Au thin film thickness uniformity on the performance of an optical fiber hydrogen sensor. Appl Surf Sci 2007;253:8615.

[19] Chen MS, Kumar D, Yi CW, Goodman DW. The promotional effect of gold in catalysis by palladium-gold. Science 2005;310:291.

[20] Hou WB, Dehm NA, Scott RWJ. Alcohol oxidations in aqueous solutions using Au, Pd, and bimetallic AuPd nanoparticle catalysts. J Catal 2008;253:22.

[21] Wang HW, Shieh CF, Chen HY, Shiu WC, Russo B, Cao GZ. Standing [111] gold nanotube to nanorod arrays via template growth. Nanotechnology 2006;17:2689.

Chapter 8: Hydridation and Dehydridation Behavior of Np-PdNi Thin Films

[1] Frazier GA, Glosser R. Phase Diagrams of Thin Films of The Palladium Hydrogen System Using a Quartz Crystal Thickness Monitor. Journal of Physics D: Applied Physics 1979;12:113.

[2] Lasser R, Klatt K-H. Solubility of Hydrogen Isotopes in Palladium. Phys Rev B 1983;28:748.

[3] Flanagan TB, Oates WA. The Palladium-Hydrogen System. Annu Rev Mater Sci 1991;21:269.

[4] Conrad H. Adsorption of Hydrogen on Palladium Single Crystal Surfaces. Surface Science 1974;41:435.

[5] Felter TE, Sowa EC. Location of Hydrogen Adsorbed on Palladium (111) Studied by Low-energy Electron Diffraction. Phys Rev B 1989;40:891.

[6] Paul J-F, Sautet P. Density-functional periodic study of the adsorption of hydrogen on a palladium (111) surface. Phys Rev B 1996;53:8015.

[7] Mitsui T, Rose MK, Fomin E, Ogletree DF, Salmeron M. Dissociative Hydrogen Adsorption on Palladium Requires Aggregates of Three or More Vacancies. Nature 2003;422:705.

[8] Lopez N, Lodziana Z, Illas F, Salmeron M. When Langmuir Is Too Simple: H2 Dissociation on Pd(111) at High Coverage. Physical Review Letters 2004; 93: 1461031.

[9] Pundt A. Hydrogen in Nano-sized Metals. Advanced Engineering Materials 2004; 6: 11.

[10] Pundt A, Kirchheim R. Hydrogen in Metals: Microstructural Aspects. Annual Review of Materials Research 2006;36:555.

[11] Krenn CR. Continuum Modelling of Transformation Hysteresis in A Metal Hydride System. Model Simul Mater Sc 2004;12:S415.

[12] Kuji T, Uchida H, Sato M, Cui W. Thermodynamic Properties of Hydrogen in Fine Pd Powders. Journal of Alloys and Compounds 1999;293-295:19.

[13] Kishore S, Nelson JA, Adair JH, Eklund PC. Hydrogen Storage in Spherical and Platelet Palladium Nanoparticles. Journal of Alloys and Compounds 2005;389:234.

[14] Eastman JA, Thompson LJ, Kestel BJ. Narrowing of The Palladium-hydrogen Miscibility Gap in Nanocrystalline Palladium. Phys Rev B 1993;48:84.

[15] Kuji T, Matsumura Y, Uchida H, Aizawa T. Hydrogen Absorption of Nanocrystalline Palladium. Journal of Alloys and Compounds 2002;330:718.

[16] Lemier C, Weissmuller J. Grain Boundary Segregation, Stress and Stretch: Effects on Hydrogen Absorption in Nanocrystalline Palladium. Acta Mater 2007;55:1241.

[17] Vargas WE, Rojas I, Azofeifa DE, Clark N. Optical and Electrical Properties of Hydrided Palladium Thin Films Studied by An Inverson Approach from Transmittance Measurements. Thin Solid Films 2006;496:189.

[18] Matelon RJ, Avila JI, Volkmann UG, Cabrera AL, Morales EH, Lederman D. Substrate Effect on the Optical Response of Thin Palladium Films Exposed to Hydrogen Gas. Thin Solid Films 2008;516:7797.

[19] Ding DY, Chen Z, Lu C. Hydrogen Sensing of Nanoporous Palladium Films Supported by Anodic Aluminum Oxides. Sensor Actuat B-Chem 2006;120:182.

[20] Lim W, Wright JS, Gila BP, Johnson JL, Ural A, Anderson T, Ren F, Pearton SJ. Room Temperature Hydrogen Detection Using Pd-coated GaN Nanowires. Applied Physics Letters 2008;93:0721091.

[21] Kabius B, Kaiser H, Kaesche H. A Micromorphological Study of Selective Dissolution of Cu from Cupd-Alloys. J Electrochem Soc 1986;133:C304.

[22] Kim J, Dohnalek Z, Kay BD. Structural Characterization of Nanoporous Pd Films Grown via Ballistic Deposition. Surface Science 2005;586:137.

[23] Berube V, Radtke G, Dresselhaus M, Chen G. Size Effects on the Hydrogen Storage Properties of Nanostructured Metal Hydrides: A review. Int J Energy Res 2007; 31: 637.

[24] Mutschele T, Kirchheim R. Hydrogen as a Probe for the Average Thickness of a Grain-Boundary. Scripta Metall Mater 1987;21:1101.

[25] Pundt A, Sachs C, Winter M, Reetz MT, Fritsch D, Kirchheim R. Hydrogen sorption in elastically soft stabilized Pd-clusters. Journal of Alloys and Compounds 1999; 295: 480.

[26] Nechaev YS. Characteristics of Hydride-like Segregates of Hydrogen at Dislocations in Palladium. Physics - Uspekhi 2001;44:1189.

[27] Lewis FA, Kandasamy K, Tong XQ. Lattice Strain Gradient Effects on Hydrogen Diffusion Parameter Calculations. Int J Hydrogen Energy 2002;27:687.

[28] Cox DM, Fayet P, Brickman R, Hahn MY, Kaldor A. Abnormally Large Deuterium

Uptake on Small Transition Metal Clusters. Catalysis Letters 1990;4:271.

[29] Forty AJ. Corrosion Micro-Morphology of Noble-Metal Alloys and Depletion Gilding. Nature 1979;282:597.

[30] Erlebacher J, Aziz MJ, Karma A, Dimitrov N, Sieradzki K. Evolution of nanoporosity in dealloying. Nature 2001;410:450.

[31] Ji CX, Searson PC. Fabrication of nanoporous gold nanowires. Appl Phys Lett 2002; 81:4437.

[32] Hayes JR, Hodge AM, Biener J, Hamza AV, Sieradzki K. Monolithic nanoporous copper by dealloying Mn-Cu. J Mater Res 2006;21:2611.

[33] Sun L, Chien CL, Searson PC. Fabrication of nanoporous nickel by electrochemical dealloying. Chem Mater 2004;16:3125.

[34] Li W-C, Schendel SC, Balk TJ. Preparation and Hydrogen Absorption/Desorption of Nanoporous Palladium Thin Films. Materials Research Society Symposium Proceedings. v. 1098, HH02.08, 2008.

[35] Li W-C, Balk TJ. Achieving Finer Pores and Ligaments in Nanoporous Palladium-Nickel Thin Films. Scripta Mater 2010;62:167.

[36] Schirber JE, Morosin B. Lattice-Constants of Beta-PdHx and Beta-PdDx with X near 1.0. Phys Rev B 1975;12:117.

[37] Cullity BD, Stock SR. Elements of X-Ray Diffraction. Upper Saddle River, NJ: Prentice Hall, 2001.

[38] Gibson LJ, Ashby MF. Cellular Solids: Structures and Properties. Cambridge: Cambridge University Press, 1997.

[39] Kart SO, Erbay A, Kilic H, Cagin T, Tomak M. Molecular Dynamics Study of Cu-Pd Ordered Alloys. Journal of Achievements in Materials and Manufacturing Engineering 2008;31:41.

[40] Makenas BJ, Birnbaum HK. Phase-Changes in the Niobium-Hydrogen System .1. Accommodation Effects during Hydride Precipitation. Acta Metall Mater 1980; 28: 979.

[41] Flanagan TB, Bowerman BS, Biehl GE. Hysteresis in Metal-Hydrogen Systems. Scripta Metall Mater 1980;14:443.

[42] Zuttel A, Nutzenadel C, Schmid G, Emmenegger C, Sudan P, Schlapbach L. Thermodynamic aspects of the interaction of hydrogen with Pd clusters. Appl Surf Sci 2000;162:571.

[43] McLellan RB, Yang L. Hydrogen-Vacancy Interactions in Palladium. Acta Metallurgica Et Materialia 1995;43:2463.

[44] Fukai Y, Okuma N. Formation of Superabundant Vacancies in Pd Hydride under

High Hydrogen Pressures. Physical Review Letters 1994;73:1640.

[45] Krystian M, Setman D, Mingler B, Krexner G, Zehetbauer MJ. Formation of Superabundant Vacancies in Nano-Pd-H Generated by High-Pressure Torsion. Scripta Mater 2010;62:49.

[46] Fukai Y. Formation of Superabundant Vacancies in Metal Hydrides at High Temperatures. Journal of Alloys and Compounds 1995;231:35.

[47] McLellan RB. The Kinetic and Thermodynamic Effects of Vacancy-Interstitial Interactions in Pd-H Solutions. Acta Mater 1997;45:1995.

[48] McLellan RB, Zang DH. Kinetics of Vacancy Migration in Hydrogenated Palladium. Scripta Mater 1997;36:1207.

[49] Mclellan RB. The Thermodynamics of Interstitial Vacancy Interactions in Solid-Solutions. J Phys Chem Solids 1988;49:1213.

[50] Miraglia S, Fruchart D, Hlil EK, Tavares SSM, Dos Santos D. Investigation of The Vacancy-Ordered Phases in The Pd-H System. Journal of Alloys and Compounds 2001;317:77.

[51] Avdyukhina VM, Anishchenko AA, Katsnel'son AA, Revkevich GP. Role of Vacancies in The Structural Relaxation of Pd-Mo Alloys Saturated with Hydrogen. Phys Solid State. 2004;46:265.

[52] Stafford GR, Bertocci U. In Situ Stress and Nanogravimetric Measurements During Hydrogen Adsorption/Absorption on Pd Overlayers Deposited onto (111)-Textured Au. J Phys Chem C 2009;113:13249.

[53] Seymour EFW, Cotts RM, Williams WD. NMR Measurement of Hydrogen Diffusion in Beta-Palladium Hydride. Physical Review Letters 1975;35:165.

[54] Crespo EA, Ruda M, de Debiaggi SR. Hydrogen Absorption in Ni and Pd: A Study Based on Atomistic Calculations. Int J Hydrogen Energy 2008;33:3561.

Chapter 9: Microstructure and Texture of Os-Ru Coatings for Porous Tungsten Dispenser Cathodes

[1] Zalm P, Stratum AJAv, Peeters HH. Tungsten Dispenser Cathode Having Emission Enhancing Coating with Osmium-Iridium or Osmium-Ruthenium Alloy for Use in Electron Tube. In: Office UP, editor, vol. 3,497,757: US Phillips Corporation, 1970.

[2] Cortenraad R, van der Gon AWD, Brongersma HH, Gartner G, Manenschijn A. Surface analysis of thermionic dispenser cathodes. Appl Surf Sci 2002;191:153.

[3] Kumar KS, Devi PD, Ravi M, Bhat KS. Work function distribution for W-Ir mixed metal matrix cathodes. Appl Surf Sci 2006;252:5632.

[4] Cronin JL. Modern Dispenser Cathodes. Iee Proc-I 1981;128:19.

[5] Private Communication with Semicon Associates.

[6] Vanveen NJA. XPS on Impregnated Cathodes - Surface Concentrations and Thermal-Stability. Appl Surf Sci 1987;29:113.

[7] Forman R. Surface Studies on the Low Work Function Surface Complex of Barium on an Osmium Ruthenium Substrate. Appl Surf Sci 1987;29:127.

[8] Koenig MF, Grant JT. XPS Studies of the Chemical-State of Ba on the Surface of Impregnated Tungsten Dispenser Cathodes. Appl Surf Sci 1985;20:481.

[9] Rachocki KD, Lamartine BC, Haas TW. Angle Resolved Photoelectron-Spectroscopy Study of M-Type Cathode Activation. Appl Surf Sci 1983;16:40.

[10] Jones D, Mcneely D, Swanson LW. Surface and Emission Characterization of the Impregnated Dispenser Cathode. Appl Surf Sci 1979;2:232.

[11] Isagawa S, Higuchi T, Kobayashi K, Miyake S, Ohya K, Yoshida M. Application of M-type cathodes to high-power cw klystrons. Appl Surf Sci 1999;146:89.

[12] Bell BV. Bias Sputter Deposition of Osmium-Ruthenium Films. Department of Chemical and Materials Engineering at the University of Kentucky. , Master thesis, Lexington, 1994.

[13] Li W-C, Robert S, Balk TJ. Characterization of Osmium-Ruthenium Coatings for Porous Tungsten Dispenser Cathodes. IEEE Transactions on Electron Devices May 2009;56, No. 5:805.

[14] Balk TJ, Li W-C, Roberts S. Characterization of Osmium-Ruthenium Coatings for Porous Tungsten Dispenser Cathodes. Ninth IEEE International Vacuum Electronics Conference. Monterey, CA, USA, April 2008. p.42.

[15] Li W-C, Balk TJ. Telephone Cord and Briar-like Buckling Delamination of Osmium-Ruthenium and Iridium Films under High Compressive Stresses. Journal of Mateirals Research 2009 (submitted).

[16] Li W-C, Roberts S, Balk TJ. Effects of Annealing on Microstructure of Osmium-Ruthenium Thin Films. Tenth IEEE International Vacuum Electronics Conference. Rome, Italy, 2009.

[17] Manenschijn A, vanVeen A, deMoor MW. Ar desorption from OsRu coated cathodes (L6). Appl Surf Sci 1997;111:76.

Vita

Wen-Chung Li

Wen-Chung Li was born on June 24, 1975 in Hsin-Chu, Taiwan. He received the B.S. degree in materials engineering from National Taipei University of Technology, Taipei, Taiwan, in 1999 and the M.S. degree in materials science and engineering from National Taiwan University of Science and Technology, Taipei, in 2001. After 2-year military service from 2001 to 2003, he was a lecturer with China University of Science and Technology, Taipei. In 2004, he attended Delta Electronics, Inc. and Wafer Works Co., Taoyuan, Taiwan, as an R&D engineer until attending the University of Kentucky for the PhD study in 2005.

Publications

Peer reviewed journals

1. W.-C. Li, S. Roberts, and T. J. Balk, "*Effects of Substrate Bias on Microstructure of Osmium-Ruthenium Coatings for Porous Tungsten Dispenser Cathodes*", *IEEE Transactions on Electron Devices*, vol. 56, no. 5, pp. 805-811, 2009
2. W.-C. Li and T. J. Balk, "*Effects of Substrate Curvature on Dealloying for Forming Nanoporous Thin Films*", *Scripta Materialia*, vol. 61, pp. 1125-1128, 2009
3. W.-C. Li and T. J. Balk, "*Achieving Finer Pore and Ligaments in Nanoporous Palladium-Nickel Thin Films*", *Scripta Materialia*, vol. 62, pp. 167-169, 2010
4. W.-C. Li and T. J. Balk, "*Transition from Single- to Multi-layered Structures in Nanoporous Gold-Palladium Ultrathin Films*", Thin Solid Films, submitted, 09.2009
5. W.-C. Li and T. J. Balk, "*Preparation and Hydrogen Absorption/Desorption of Nanoporous Palladium Thin Films*", *Materials* (invited paper), accepted, 12.2009
6. W.-C. Li, C. Liang, and S.-T. Lin, "*Heteroepitaxial Growth of a Nanocrystalline TiC layer on a Diamond Substrate*", *Diamond and Related Materials*, Vol. 11, pp. 1366-1373, 2002

7. W.-C. Li, C. Liang, and S-T Lin, “*Interfacial Segregation of Ti in the Brazing of Diamond Grids onto a Steel Substrate Using a Cu-Sn-Ti Brazing Alloy*”, *Metallurgical and Materials Transactions A*, Vol. 33, pp. 2163-2172, 2002

Conference proceedings

1. W.-C. Li, S. Roberts, and T. J. Balk, “*Effects of Annealing on Microstructure of OsRu Thin Films*”, International Vacuum Electronics Conferences Symposium Proceedings, Rome, Italy, 04.2009
2. T. J. Balk, W.-C. Li, and S. Roberts, “*Characterization of Osmium-Ruthenium Coatings for Porous Tungsten Dispenser Cathodes*”, International Vacuum Electronics Conferences Symposium Proceedings, Monterey, CA, USA, 04.2008
3. W.-C. Li, S. C. Schendel, and T. J. Balk, “Microstructure and Hydrogen Cycling Behavior of Nanoporous Pd Thin Films”, Materials Research Society Symposium Proceedings, vol. 1098 (HH02-08), San Francisco CA, USA, 03.2008